



HAL
open science

The Van Allen Probes Electric Field and Waves Instrument: Science Results, Measurements, and Access to Data

A. W. Breneman, J. R. Wygant, S. Tian, C. A. Cattell, S. A. Thaller, K. Goetz, E. Tyler, C. Colpitts, L. Dai, K. Kersten, et al.

► **To cite this version:**

A. W. Breneman, J. R. Wygant, S. Tian, C. A. Cattell, S. A. Thaller, et al.. The Van Allen Probes Electric Field and Waves Instrument: Science Results, Measurements, and Access to Data. Space Science Reviews, 2022, 218, 10.1007/s11214-022-00934-y . insu-04089865

HAL Id: insu-04089865

<https://insu.hal.science/insu-04089865>

Submitted on 5 May 2023

HAL is a multi-disciplinary open access archive for the deposit and dissemination of scientific research documents, whether they are published or not. The documents may come from teaching and research institutions in France or abroad, or from public or private research centers.

L'archive ouverte pluridisciplinaire **HAL**, est destinée au dépôt et à la diffusion de documents scientifiques de niveau recherche, publiés ou non, émanant des établissements d'enseignement et de recherche français ou étrangers, des laboratoires publics ou privés.



Distributed under a Creative Commons Attribution 4.0 International License



The Van Allen Probes Electric Field and Waves Instrument: Science Results, Measurements, and Access to Data

A.W. Breneman¹ · J.R. Wygant² · S. Tian² · C.A. Cattell² · S.A. Thaller² · K. Goetz² · E. Tyler² · C. Colpitts² · L. Dai² · K. Kersten² · J.W. Bonnell³ · S.D. Bale³ · F.S. Mozer³ · P.R. Harvey³ · G. Dalton³ · R.E. Ergun^{4,5} · D.M. Malaspina^{4,5} · C.A. Kletzing⁶ · W.S. Kurth⁶ · G.B. Hospodarsky⁶ · C. Smith^{3,7} · R.H. Holzworth⁸ · S. Lejosne³ · O. Agapitov³ · A. Artemyev⁹ · M.K. Hudson¹⁰ · R.J. Strangeway⁹ · D.N. Baker^{4,5} · X. Li⁴ · J. Albert¹¹ · J.C. Foster¹² · P.J. Erickson¹² · C.C. Chaston³ · I. Mann¹³ · E. Donovan¹⁴ · C.M. Cully¹⁴ · V. Krasnoselskikh¹⁵ · J.B. Blake¹⁶ · R. Millan¹⁰ · A.J. Halford¹

Received: 1 November 2021 / Accepted: 31 October 2022 / Published online: 25 November 2022

This is a U.S. Government work and not under copyright protection in the US; foreign copyright protection may apply 2022, corrected publication 2022

Abstract

The Van Allen Probes Electric Fields and Waves (EFW) instrument provided measurements of electric fields and spacecraft floating potentials over a wide dynamic range from DC to 6.5 kHz near the equatorial plane of the inner magnetosphere between 600 km altitude and 5.8 Re geocentric distance from October 2012 to November 2019. The two identical instruments provided data to investigate the quasi-static and low frequency fields that drive large-scale convection, waves induced by interplanetary shock impacts that result in rapid relativistic particle energization, ultra-low frequency (ULF) MHD waves which can drive radial diffusion, and higher frequency wave fields and time domain structures that provide particle pitch angle scattering and energization. In addition, measurements of the spacecraft potential provided a density estimate in cold plasmas (< 20 eV) from 10 to 3000 cm⁻³. The EFW instrument provided analog electric field signals to EMFISIS for wave analysis, and it received 3d analog signals from the EMFISIS search coil sensors for inclusion in high time resolution waveform data.

The electric fields and potentials were measured by current-biased spherical sensors deployed at the end of four 50 m booms in the spacecraft spin plane (spin period ~ 11 sec) and a pair of stacer booms with a total tip-tip separation of 15 m along the spin axis. Survey waveform measurements at 16 and/or 32 S/sec (with a nominal uncertainty of 0.3 mV/m over the prime mission) were available continuously while burst waveform captures at up to 16,384 S/sec provided high frequency waveforms.

This post-mission paper provides the reader with information useful for accessing, understanding and using EFW data. Selected science results are discussed and used to highlight instrument capabilities. Science quantities, data quality and error sources, and analysis routines are documented.

1 Instrument and Mission Overview

The twin Van Allen Probes (Mauk et al. 2013) were launched into a near-equatorial elliptical orbit on 2012-08-30. Throughout their prime mission (until 2014-10-31) and most of the extended mission phases, their orbit altitude varied from 600 km to 5.8 Earth Radii (RE). Because the orbital plane was inclined by 17 deg, magnetic latitudes of approximately ± 20 deg at L-shells as high as ~ 8 were sampled. This orbit was designed to capture physics in a wide range of regions including the inner radiation belt, the dynamic outer belt, the near-tail, and the plasmasphere. Within these regions energetic particle populations can vary by orders of magnitude as the magnetosphere interacts with the solar wind and structures including shocks, CMEs, and fast-slow stream interfaces. Manifestations of this interaction include the aurora, radial motion of plasma, the formation of the ring current, and the varying radiation belt structure.

Electric fields drive the dynamics of these plasma environments on physical scales, frequencies, and amplitudes that span 8 orders of magnitude in temporal scale (tens of hours to fractions of a millisecond) and 5 orders of magnitude in spatial scale (tens of Earth radii down to tens of km). At global scales, the convection electric field, the co-rotation electric field, and sub-auroral electric fields drive macroscopic transport and motion of boundaries. At MHD scales, ULF-wave fields are associated both with prompt energization and transport (reconnection, shocks, and injection fronts) and with diffusive transport and particle boundary loss. At small scales, kinetic Alfvén waves, very low frequency waves (hiss, chorus), and impulsive time domain structures can also result in both diffusive and prompt energization and scattering. The Van Allen Probes Electric Fields and Waves (EFW) instrument (Wygant et al. 2013) was designed to make measurements of electric fields and spacecraft potential over this entire range. EFW is based on a long heritage, including double probe instruments on the Air Force S3-3 spacecraft (Mozer et al. 1979), the NASA-ESA International Sun-Earth Explorer (Mozer et al. 1978a, 1978b), the Swedish Viking satellite (Falthammar et al. 1987), the Air Force CRRES spacecraft (Wygant et al. 1992), the Geotail Spacecraft (Tsuruda et al. 1994), the Akebono Spacecraft (Hayakawa et al. 1990), the NASA Polar spacecraft (Harvey et al. 1995), the NASA FAST spacecraft (Carlson et al. 1998), the ESA-NASA Cluster spacecraft (Gustafsson et al. 1997, 2001), and the NASA THEMIS spacecraft (Bonnell et al. 2008).

The Principal Investigator for the Van Allen Probe EFW instruments was John Wygant at the University of Minnesota. The instruments, including the main electronics packages and the boom deployment units and sensors, were fabricated and tested under the leadership of John Bonnell at the Space Sciences Laboratory (SSL) at the University of California Berkeley. Digital signal processing boards were provided by Robert Ergun and David Malaspina at the University of Colorado Boulder. There were two Science Operations Centers for EFW data: one at SSL led by John Bonnell and the other at the University of Minnesota by Aaron Breneman. The theory/simulation effort was led by Mary Hudson at Dartmouth College.

To make the measurements required to meet the science objectives of the Van Allen Probes, the EFW instrument had the following baseline measurement goals (Wygant et al. 2013):

1. Measure 2d quasi-static electric fields in the spin plane of the spacecraft at radial distances > 3 RE to an accuracy of 0.3 mV/m or 10% of the maximum electric field amplitude, whichever is larger, over a dynamic range of ± 500 mV/m above $L = 3$.
2. Provide measurements of the quasi-static electric field component along the shorter spin axis booms to an accuracy of 4 mV/m or 20% of the maximum electric field magnitude at radial distances > 3 Re.

3. Provide measurements of cold (< 20 eV) plasma variations in the plasmasphere over time scales from DC to < 1 sec with an accuracy of 50% over a density range from 0.1 to 50 cm^{-3} .
4. Provide burst waveform measurements of large amplitude electric fields of at least 250 Hz with an accuracy of 0.3 mV/m and a range of 500 mV/m at a variety of programmable rates ranging from 512–16,384 512 S/sec.
5. Include measurements of the 3d wave magnetic field obtained from the EMFISIS (Kletzing et al. 2013) instrument in burst recordings (along with the wave electric field measurements described above) of at least 250 Hz.
6. Provide interferometric timing of the propagation of small-scale waves and structures between opposing sensor pairs using burst recordings with a time cadence of up to 16,384 S/sec.
7. Provide spectral and cross-spectral information on the wave electric fields, magnetic fields, and density fluctuations up to 250 Hz.
8. Provide the EMFISIS wave instrument with the three measured components of the electric field over the frequency range from 10 Hz to 400 kHz with a noise level of $10^{-13} \text{ V}^2/\text{m}^2 \text{ Hz}$ at 1 kHz and $10^{-17} \text{ V}^2/\text{m}^2 \text{ Hz}$ at 100 kHz with a 90 dB dynamic range and a maximum signal of 30 mV/m.

Making these accurate measurements necessitated specific design requirements, as described in Wygant et al. (2013).

Electric field and potential measurements were made with two pairs of current biased spherical sensors with ~ 100 m tip-tip separations, providing accurate electric field measurements in the spin plane. In addition, two sensors with a ~ 15 m separation on stacer booms along the spin axis provided the third component of the electric field. Due to the shorter separation, this component was used primarily for wave measurements at frequencies > 100 Hz where the sensors were no longer DC-coupled to the plasma.

At low frequencies, spin plane measurements are approximately an order of magnitude more accurate than spin axis measurements because of the large probe separation and the orientation perpendicular to the Earth-Sun line, which ensured that the spin plane sensors were not shadowed by the spacecraft body or each other. This orientation was well-suited to measure the large-scale convection electric field and other important fields such as azimuthal components resulting from shock impacts. Current biasing decreased errors associated with photocurrents from surfaces near the sensors and also decreased the sensor-plasma sheath impedance, allowing measurement of quasi-static electric fields to roughly 0.3 mV/m during the prime mission phase. In addition, the instruments were designed with a large dynamic range allowing measurement of both large and small electric fields even when experiencing significant spacecraft charging, which sometimes occurred during geomagnetically active conditions.

Standard survey data products included 32 S/sec electric fields calculated from onboard-differenced potential measurements, and 16 S/sec probe potentials. The latter were used both to calculate electric fields on the ground, and as measurements of spacecraft charging and estimates of cold plasma density. EFW also provided full duty cycle frequency binned data of both electric and magnetic field (via analog channels from EMFISIS) from DC to 6.5 kHz in the form of 4 sec power-spectra in 64 pseudo-logarithmic frequency bins, and 8 S/sec peak and average amplitude (filter bank) spectra in 7 or 13 frequency bins. Higher cadence, non-survey products included two types of 3d burst wave electric and magnetic field, an autonomously selected *burst 2* and a ground-selected *burst 1*. The latter used an unprecedentedly large 32 GB memory allowing sampling and playback of hours of data during especially interesting intervals as selected by scientists on the ground. This fundamentally

changed the nature of burst data collection and transmission and enabled the collaborative campaigns with other missions that became a fundamental part of the EFW contribution to Van Allen Probes science.

Throughout the Van Allen Probes mission, scores of studies and many conjunctive campaigns utilized EFW data to probe deeply the electrodynamics of the Earth's radiation belts in the inner magnetosphere. Sections 2 and 3 below summarize the highlights of these studies and campaigns. Section 4 then presents an overview of electric field measurement with the double probe technique, and describes the basic data quantities, calibration, flags and error sources, and data and software availability for the EFW instrument and its data products.

2 EFW Science Results

The design features of the Electric Fields and Waves (EFW) instrument enabled the discovery of new physics addressing the primary science goals of the Van Allen Probes mission (Mauk et al. 2013), including radiation belt acceleration and loss, and the dynamics of the inner magnetosphere and ring current. These features include the most sensitive inner magnetospheric measurements of the quasi-static electric field, estimates of the cold plasma density from spacecraft potential, and high time resolution electric and magnetic fields in the form of power spectra, fast filter bank wave amplitudes, and long-duration burst waveforms.

In this section, we will highlight selected studies that described new physics or improved understanding of inner magnetosphere and radiation belt physics that made use of EFW's capabilities. These include discoveries using burst data of unexpected large populations of nonlinear field-aligned kinetic structures called Time Domain Structures (Mozer et al. 2013), which can drive significant electron acceleration and loss cone scattering. In addition, burst data was key to the finding that intense and ubiquitous kinetic Alfvén waves (Chaston et al. 2014) in the near-Earth plasma sheet can energize outflowing oxygen that can contribute significantly to the ring current during storms and produce relativistic electron dropouts. We describe innovative research on the role of whistler mode hiss and chorus waves in acceleration, loss, and transport of energetic electrons, including statistics of large amplitude chorus (Tyler et al. 2019a,b) and a study showing that the nonlinear interactions of chorus and electrons depend critically on the chorus coherence length and source scales (Agapitov et al. 2017). At lower frequencies, Dai et al. (2013) used EFW DC-coupled waveform data to provide unambiguous evidence for the generation of a fundamental mode standing poloidal wave in drift resonance with keV ring current ions. These observations provide the first in space of the fishbone instability observed in Tokamaks – a major contributor to fusion confinement disruption. Lena et al. (2021) identified low L (~ 1.1) standing mode waves that are sensitive indicators of magnetosphere-ionosphere coupling.

On global scales, prompt energization of electrons following a shock impact was thoroughly studied with a combination of observations from both Van Allen Probe satellites and modeling (Foster et al. 2015; Hudson et al. 2015). On much longer time scales, Thaller et al. (2019) used EFW measurements to uncover a 27-day periodicity in the large-scale dawn-dusk convection electric field and plasmopause location during the declining phase of the solar cycle. The role of this convection electric field in driving energetic particle transport and acceleration from the tail region to the inner magnetosphere was detailed by Thaller et al. (2015) and Califf et al. (2017).

These results, and more, described below, represent only a handful of the many and varied research studies that utilized EFW data for important discoveries and new understanding. Science results obtained during collaborative campaigns with balloons, CubeSats, and other

satellites are presented in Sect. 3. Research utilizing EFW data has resulted in significant progress in meeting the goal of the EFW investigation to *measure the electric fields associated with a variety of mechanisms causing particle acceleration and scattering in the inner magnetosphere*, as well as to the larger mission goals to *discover which processes, singly or in combination, accelerate and transport radiation belt electrons and ions and under what conditions; understand and quantify the loss of radiation belt electrons and determine the balance between competing acceleration and loss processes; and understand how the radiation belts change in the context of geomagnetic storms*.

2.1 Prompt Acceleration by Impulsive Electric Fields due to Interplanetary Shocks

Dynamics of the magnetosphere on global scales are associated with electric fields generated by the coupling of the solar wind plasma to the magnetosphere. Large-scale impulsive shock-induced electric fields can provide dramatic energization and transport of energetic electrons deep inside the radiation belts on timescales of minutes (Wygant et al. 1994; Li et al. 1993). These dynamic events, though occurring on average only a few times per year, can lead to strong outer belt enhancements or depletions, or even the creation or destruction of new belt structure (Baker et al. 2013). Prior to the Van Allen Probes, comprehensive observations of such shock-driven acceleration events were lacking due to insufficient dayside satellite coverage within the radiation belts and/or lack of in situ solar wind monitoring. One of the primary goals of the Van Allen Probes was to fill in these observational gaps to determine the role of interplanetary shock impacts on acceleration and loss of radiation belt particles.

The first comprehensive verification of prompt shock-driven acceleration was by Foster et al. (2015) who analyzed Van Allen Probes data following a moderate shock impact on October 8th, 2013. Both Van Allen Probes (A at $L = 3$ and $MLT = 13.5$, and B at $L = 5$ and $MLT = 17.3$) observed a dramatic ~ 1 min increase in the dawnward electric field associated with the shock arrival, shown in Fig. 1 for Probe B. The dual observations over a large spatial separation were key to revealing that this initial electric field fluctuation was observed over a substantial portion of the dayside equatorial magnetosphere, and propagated duskward at ~ 850 km/s, similar to the azimuthal drift velocity of ~ 2 –4 MeV electrons. A simple model using these properties of the electric field predicted that these electrons would be radially displaced inwards by 0.5 L and energized by up to 400 keV. These predictions were confirmed by a comparison with Probe B relativistic electron fluxes measured by REPT (middle panel) that show nearly simultaneous enhancements of 2–4 MeV electrons, while electrons outside of this energy range gained little to no energy. Hudson et al. (2015) simulated this event with a global MHD model constrained by observed upstream solar wind parameters. The bottom panel in Fig. 1, which plots the electric field from the simulation at the location of Probe B, illustrates that the simulation captures the main features of the observed field.

Analysis of other interplanetary shock events observed by the Van Allen Probes (Baker et al. 2016; Kanekal et al. 2016) indicates that they can result in both increases, decreases, or no change in relativistic electron populations. For example, Schiller et al. (2016) showed that 25%(14%) of events from a study of 81 interplanetary shock impacts resulted in increases(decreases) in > 1.8 MeV electrons, with the degree of increase most closely correlated with the shock strength. A majority of shocks, however, resulted in no measurable change in these electrons, suggesting that shock effectiveness is strongly dependent on the exact nature of the shock/magnetosphere coupling as well as the pre-impact state of the magnetosphere. This idea is further supported by the event study of Cattell et al. (2017) who showed that even a small shock-induced electric field, which did not have the typical bipolar signature seen with large shocks (dawnward followed by duskward), energized electrons

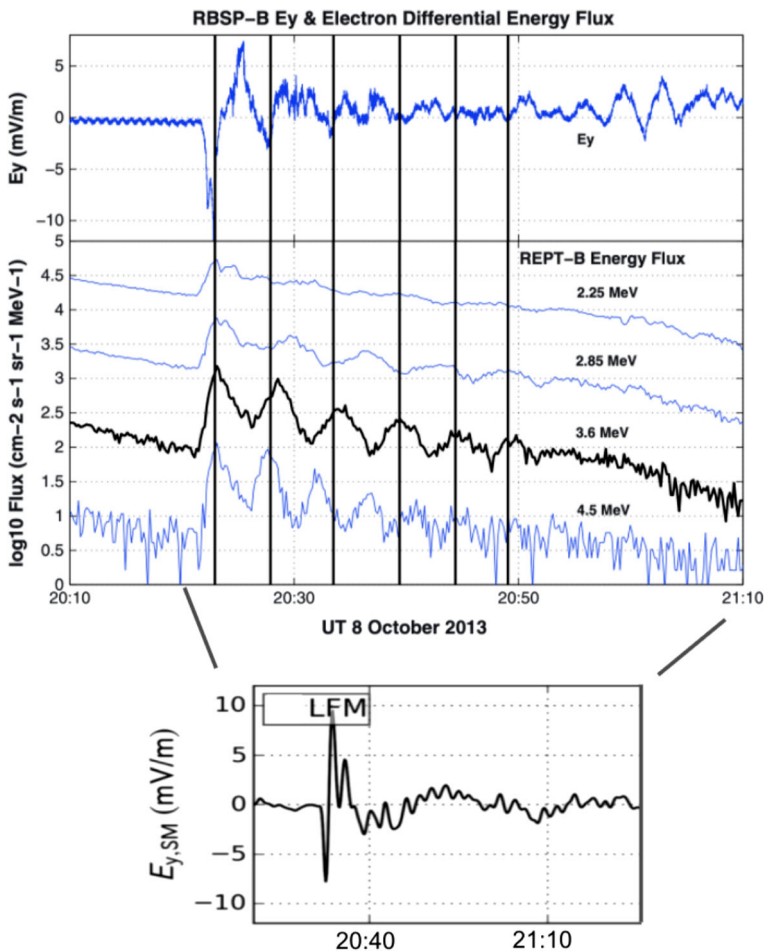


Fig. 1 (Adapted from Foster et al. 2015) Shock induced acceleration event showing 3.6 MeV electrons in drift resonance with a 300 sec period ULF wave train that followed the initial shock-induced impulse at the $L^* \sim 5$ position of Probe B. From top to bottom: Ey GSE observed by the EFW instrument. A clear 300 s periodicity is seen in the negative Ey component (vertical black lines). (middle) REPT differential electron energy flux for 2.25–4.5 MeV. (bottom; adapted from Hudson et al. 2015) The resultant Ey (SM coordinates) from the LFM simulation of this event

to > 50 keV. These observational studies have provided invaluable input into increasingly sophisticated simulations (Hudson et al. 2015; Paral et al. 2015; Hudson et al. 2017; Patel et al. 2019) to provide a more comprehensive understanding of the role of interplanetary shock impacts in radiation belt creation, enhancement and loss, a primary science goal of the EFW instrument.

2.2 Convection Electric Fields

In the inner magnetosphere, the dawn-dusk quasi-static electric field determines the location of important plasma boundaries such as the plasmopause, and can drive significant ring current enhancements. Under quiet to moderately active conditions, this field decreases sig-

nificantly at subauroral latitudes. However, limited CRRES satellite observations indicated that the fields can penetrate to low latitudes during periods of enhanced geomagnetic activity in a manner not predicted by models (Rowland and Wygant 1998; Wygant et al. 1998). An important part of both the Van Allen Probes mission and EFW design was to accurately measure these fields throughout the inner magnetosphere. In this section, we briefly describe select results showing that large-scale electric fields drive energization and transport of ring current plasma, modify boundary regions of the inner magnetosphere, and are associated with subauroral flows and optical emissions.

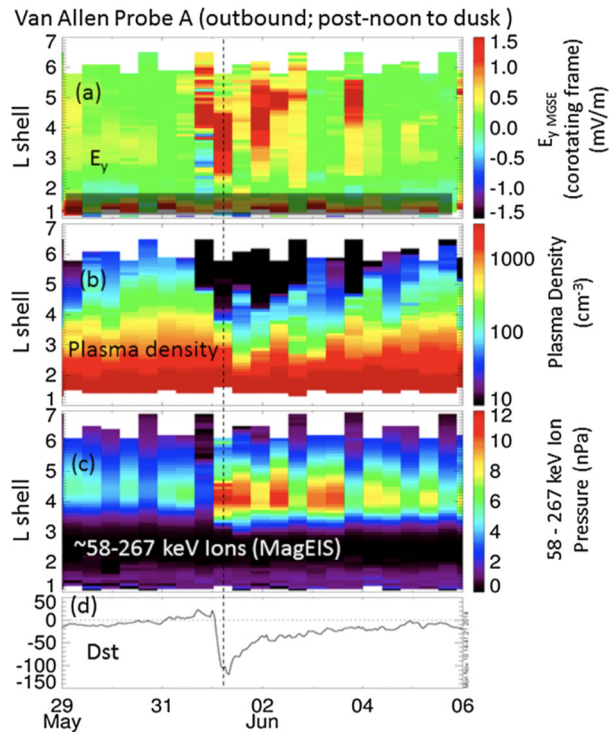
The discovery of a dominant 27-day periodicity in the dawn-dusk convection electric field during the declining phase of the solar cycle was described by Thaller et al. (2019). This periodicity is due to forcing at the solar rotation period by the enhanced solar wind convection electric fields (E_y GSE) associated with the high-speed streams of co-rotating interaction regions (CIRs). The resulting enhancement in the magnetospheric convection electric field increases erosion of the plasmasphere (as measured at all magnetic local times), driving the plasmapause inwards by nearly 0.5 RE. At a given L value, density variations of 20–35% (about the average value) were observed. Similar periodicities were not observed near solar maximum, which is characterized by sporadic coronal mass ejections rather than regular CIRs. This research revealed previously unobserved details of the fundamental connection between solar wind driving, enhanced convection, and the basic shape of boundaries within the magnetosphere, and has significant implications for models describing the long-term variability of the inner magnetosphere and radiation belts.

Thaller et al. (2015) combined EFW data with a particle drift model to convincingly link electric field enhancements with transport and energization of plasma, as illustrated in Fig. 2, which plots eight days of electric field, cold plasma density and energetic ion pressure for post-noon to dusk (outbound) orbits. Strong (1–2 mV/m), prolonged (~ 10 hrs) enhancements in the electric field down to $L < 3$ occurred during the storm main phase (DST ~ -120 nT) on both dusk and night sides. The drift model predicted that these fields were responsible for transporting and energizing plasma from the typical inner edge of the plasma sheet at $L = 6$ – 10 down to $L = 3.5$ – 5.8 where nearly simultaneous enhancements of ring current pressure (58–267 keV ions) and plasmasphere erosion were observed. This result is the first direct verification of the dominant role of the convection electric field in driving the formation of the ring current.

In a different storm, large convection electric fields drove strong inward plasma transport, resulting in an enhancement of electrons as high as ~ 500 keV by two orders of magnitude for the slot region down to $L \sim 3$ (Califf et al. 2017). Using a combination of Van Allen Probes and high-latitude DMSP data, Califf et al. (2016a) showed that enhanced electric fields lasting for hours (attributed to the pileup of earthward propagating dipolarization fronts) resulted in the injection of hundreds of keV electrons to even lower L (< 2.5). The above studies clearly show that large-scale storm-time electric fields are able to penetrate to low L where they erode the plasmasphere and provide significant transport and energization of both electrons and ions. These low L dynamics are often not well captured in conventional electric field models, as shown in comparisons to observed penetration electric fields on the Van Allen Probes by Menz et al. (2019).

For cold plasma originating in the outer plasmasphere, enhanced convection electric fields drive both low altitude ions (F region O^+) and high-altitude ions (topside H^+ , He^+) from the plasmasphere boundary layer (PBL; Carpenter and Lemaire 2004) to cusp field lines, where they modulate reconnection rates, and also ion outflow and acceleration processes in the topside ionosphere. This was shown in a Van Allen Probes and DMSP conjunction study during the March 17, 2013 geomagnetic storm (Fig. 3) by Foster et al. (2014)

Fig. 2 (Adapted from Thaller et al. 2015) Eight days of EFW data from outbound orbits encompassing the post-noon to dusk sector during a geomagnetic storm on June 1, 2013 showing the association between the (a) enhanced dawn-dusk quasi-static electric field, (b) erosion of cold plasma as seen in the plasma density determined from EFW spacecraft potential, (c) and inward transport of ring current ions. A similar result (not shown) was obtained on the inbound orbits for the pre-noon sector indicating that this process was very extensive in MLT



who observed significant erosion of cold ion flux at both ionospheric and magnetospheric altitudes.

Locally enhanced tailward electric fields are also known to drive fast flows in the ionosphere known as subauroral polarization streams (SAPS; Foster and Burke 2002). This polarization electric field is formed during disturbed conditions when the inward extent of enhanced populations of injected energetic ring current ions lies earthward of plasmasheet electrons. It maps along equipotential magnetic field lines to a strong poleward electric field in the sub-auroral ionosphere that drives the westward (sunward) SAPS flow. This overlaps with the outer plasmasphere and draws out plasmaspheric erosion plumes from their dusk-sector source sunward to the low altitude cusp, and to the magnetopause merging region where they can significantly affect reconnection rates (Walsh et al. 2013; Foster et al. 2020). Within this plume the presence of cold dense plasmaspheric ions alters the characteristics of plasma wave growth and wave-particle interactions. The Van Allen Probes altitude, orbit, and EFW data have provided excellent coverage of these and other PBL processes.

Large, localized enhancements in the low latitude electric field have also been linked with strong plasma flows associated with SAR (Stable Auroral Red) arcs and the recently (re-)discovered optical emission named STEVE (Strong Thermal Emission Velocity Enhancement, MacDonald et al. 2018). Chu et al. (2019) used a conjunction between the Van Allen Probes and a STEVE event observed at ground stations to show that the optical emissions originating at a sharp plasmapause boundary are associated with a strong and narrow tailward electric field of 20 mV/m which causes enhanced westward plasma $\mathbf{E} \times \mathbf{B}$ drifts (consistent with subauroral ion drifts; Mishin et al. 2013).

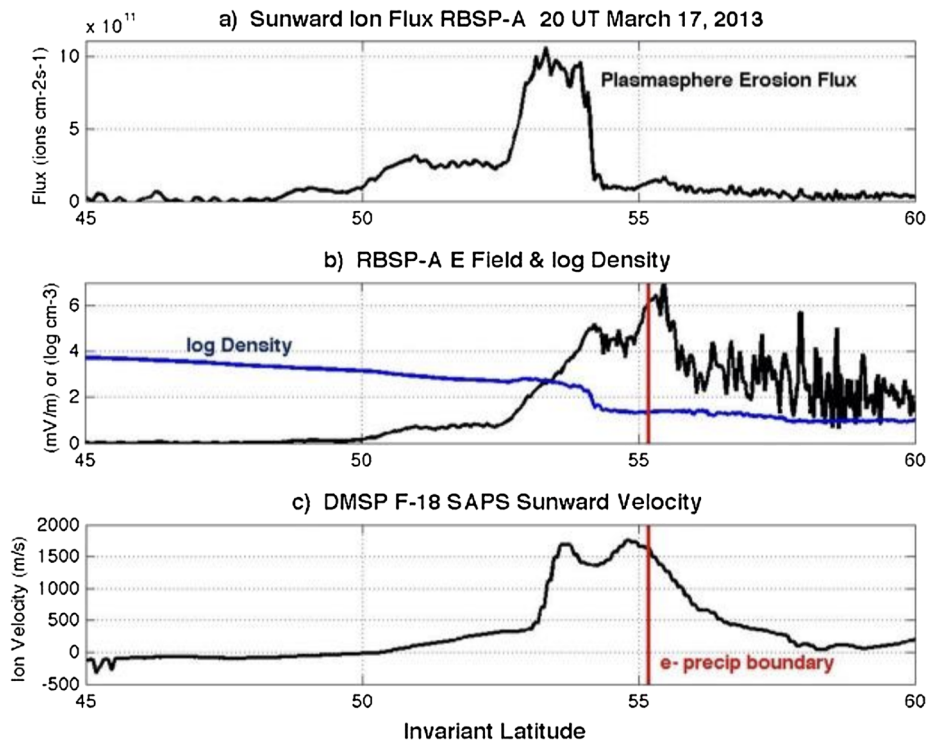
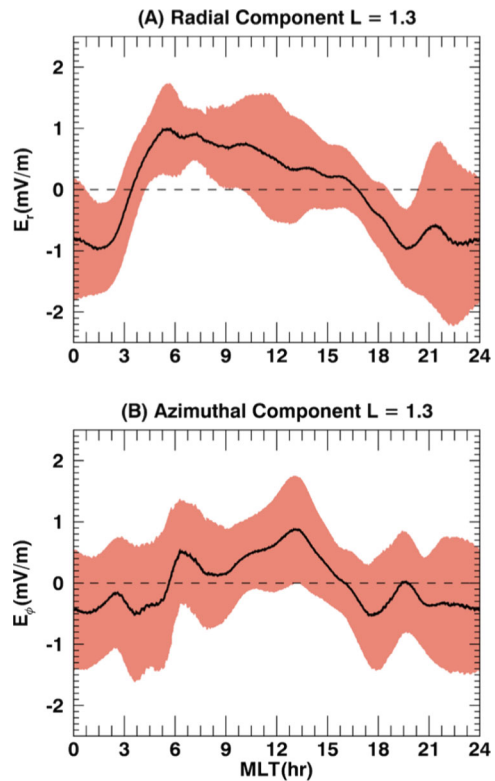


Fig. 3 (Adapted from Foster et al. 2014) (a) Plasmasphere erosion flux derived from in situ EFW observations as Probe A exited the outer plasmasphere near the apex of the $L = 3$ field line on March 17, 2013. (b) EFW radial electric field magnitude and log electron density. Sunward erosion flux maximizes in the region where the SAPS electric field overlaps the outer plasmasphere. (c) DMSP sunward ion velocity at ~ 830 km altitude showing close similarity in position and shape with the outer plasmasphere SAPS EFW electric field. The red fiducial line indicates the equatorward extent of DMSP observed precipitation of 100 eV plasma sheet electrons

2.3 Electric Fields at Low L

Studies of the dynamics of energetic (~ 100 keV) electrons at low L during both quiet and active times have repeatedly demonstrated the necessity to include new features in global electric field models in the inner belt region (e.g., Ukhorskiy et al. 2014; Selesnick et al. 2016; Su et al. 2016) and below (Selesnick et al. 2019). In practice, measuring these electric fields is extremely difficult because the electric field induced by spacecraft motion (maximum of ~ 250 mV/m near perigee along the Van Allen Probes orbit) needs to be subtracted from the measurement to obtain the naturally occurring electric fields. The true geophysical electric field, in contrast, is a combination of the corotational electric field (maximum of ~ 14 mV/m near perigee and falls as $1/r^2$) and electric fields in the corotation frame of 0.1–1 mV/m resulting from the dynamic coupling between the thermosphere, ionosphere, and magnetosphere. Thus, from the original 200–300 mV/m electric field measured in the spacecraft frame, a measurement accuracy much better than 1% is required to detect and analyze the dynamics of the DC electric fields (typically < 1 mV/m) at low L . Lejosne and Mozer (2016a, 2016b, 2019) and Lejosne et al. (2021) demonstrated that the Van Allen Probes provided the first instrument package accurate enough to achieve the goal of de-

Fig. 4 (Adapted from Lejosne et al. 2021) Two years (2013–2014) of EFW electric field measurements during quiet intervals ($K_p < 3$) at $L = 1.3$ in the (a) radial (positive away from Earth) and (b) azimuthal (positive eastward) directions. The data was projected to the magnetic equator and corotation was subtracted. The solid black lines are the 1 hr-MLT running averages of the data points and the shaded areas are the standard deviations. The 24 hr-MLT experimental averages of the radial and azimuthal electric field components (0.02 mV/m and 0.20 mV/m, respectively) have been subtracted from the datasets for calibration purposes. The electric field variation results mainly from the quiet time wind dynamo, with positive radial and azimuthal components corresponding to westward and northward convective drifts in the ionosphere, respectively



providing reliable near-equatorial electric field measurements at $L < 3$. This technical feat provided much-needed data in a region of space historically deprived of in-situ electric field measurements. Lejosne and Mozer (2016a, 2016b) showed that the Van Allen Probes can resolve the dynamo electric fields produced by tidal motion of upper atmospheric winds flowing across the Earth's magnetic field lines (the ionospheric wind dynamo), and can detect electric field perturbations associated with changes in background magnetic activity (Lejosne and Mozer 2018, 2020). These results opened new fields of research in the coupling of the magnetosphere, thermosphere, and ionosphere. For example, Lejosne et al. (2021) combined Van Allen Probes field and particle measurements, together with a physics-based coupled model, to demonstrate that the neutral winds and associated wind dynamo are the main drivers of drift shell distortion in the Earth's inner radiation belt (Fig. 4).

Van Allen Probes EFW measurements enabled Lena et al. (2021) to identify the faint electric field signatures of toroidal odd harmonic field line eigenfrequencies (0.5–3.5 Hz) at extremely low L values from 1.1–1.5. No corresponding magnetic signatures were observed in either the EMFISIS searchcoil or fluxgate magnetometers. This may be due to the decreased frequency response of the searchcoil (a factor of 20 less at 1 Hz than 10 Hz) and the decreased sensitivity of the fluxgate near perigee where it was optimized for large dynamic range. As shown in Fig. 5, the harmonics exhibit a strong frequency variation with L , which was explained by the competing effects of density, composition, magnetic field, and field line length. These waves are therefore sensitive indicators of magnetosphere-ionosphere coupling. Similar signatures are a common feature of Van Allen Probes data in the inner belt and the near-equatorial topside ionosphere from 600 to 3000 km altitude. Given the

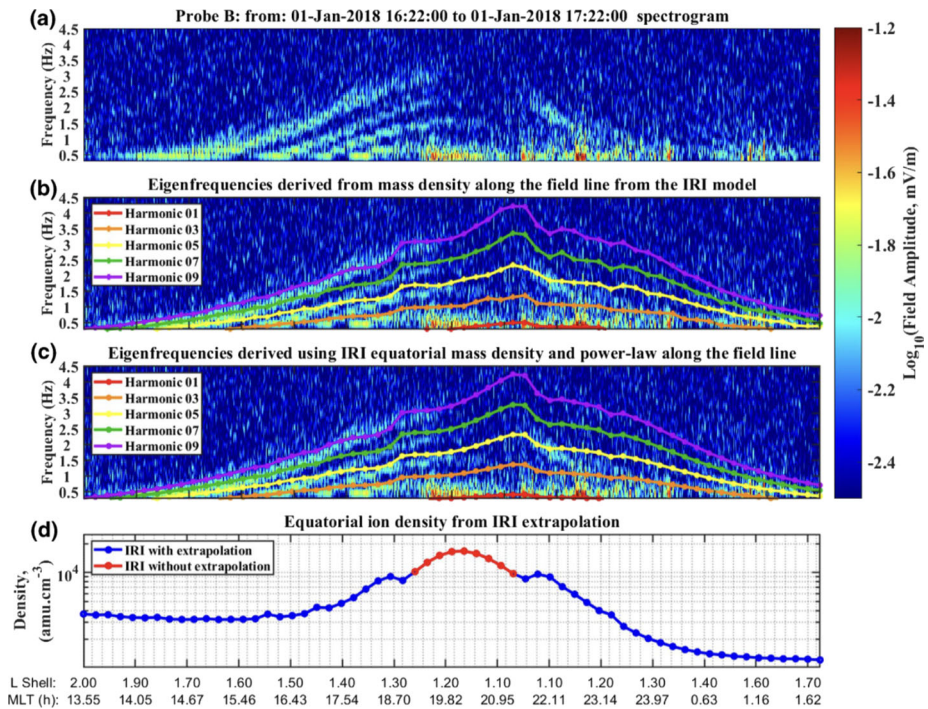


Fig. 5 (Adapted from Lena et al. 2021) EFW observations showing the faint electric field signatures of toroidal odd harmonic field line eigenfrequencies at low L on Van Allen Probe B. The observed electric field amplitude spectrum in the first three panels is overlaid with (b) predicted eigenfrequencies calculated using the IRI model mass density and (c) equatorial mass density extrapolated along the field line to the spacecraft location. Panel d shows the ion density model, with red showing direct IRI values and blue showing extrapolated IRI values

rapid changes in composition expected over this range of altitudes, follow-up studies should provide useful constraints on models of ionospheric composition, mass, and density in this region.

2.4 ULF Waves and Electric Field Structures

Ultralow frequency (ULF) waves, existing in a wide frequency range from ~ 1 mHz to 1 Hz, are ubiquitous in the magnetosphere. They are generated by a number of processes both internal and external to the magnetosphere and provide important acceleration and transport (both coherent and diffusive), and outer boundary loss of energetic particles. Internally generated ULF waves in the Pc5 (45–150 mHz) and Pc4 (150–600 mHz) range (e.g., Jacobs et al. 1964) have a large spatial extent and can produce standing mode structures such as cavity modes and field line resonances. The particular type of resonance structure – toroidal or poloidal, based on azimuthal mode number – strongly influences their interaction with charged particles. Prior to the Van Allen Probes, no comprehensive observations had been made of these fundamental standing mode structures.

Unambiguous evidence for the generation of a fundamental mode standing poloidal wave by drift resonance with ring current ions was provided for the first time by Dai et al. (2013), who analyzed the phase relation between electric and magnetic field signatures for an event

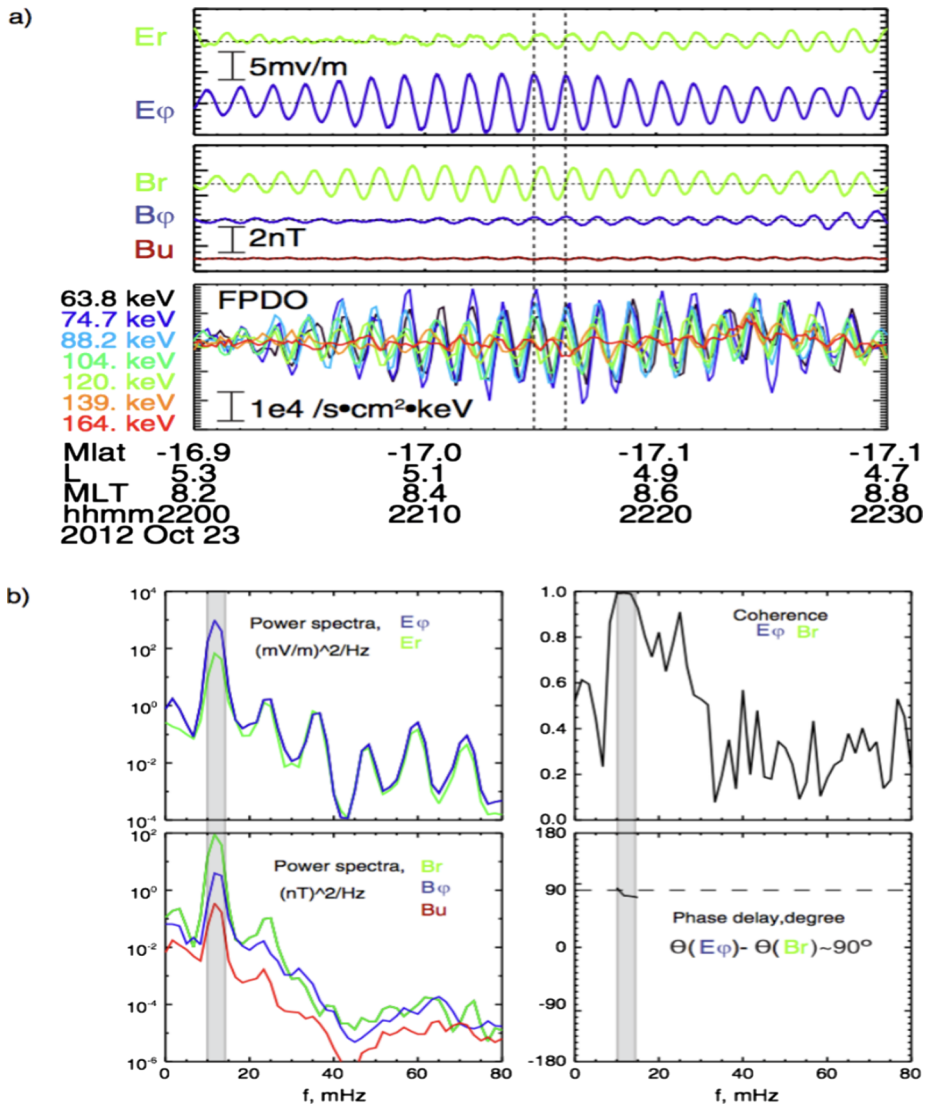


Fig. 6 (Adapted from Dai et al. 2013) Fundamental mode standing poloidal wave with electric and magnetic fields in drift resonance with 63–164 keV ring current ions (Panel a). The results of a spectral and coherence analysis between the wave components are shown in Panel b

observed on Van Allen Probe A at $L \sim 5$ in the post-dawn magnetosphere. Figure 6 shows that wave electric and magnetic fields are highly coherent, and that the dominant components of azimuthal electric and radial magnetic fields (top two a panels) at 12 mHz exhibit the expected phase relationship (b panels) for a fundamental standing mode wave. In addition, the particle observations (third a panel) indicate a coherent drift resonance interaction with 63–164 keV ring current ions, as predicted by resonance theory from Southwood and Kivelson (1981). These ions exhibit an earthward radial phase space gradient and thus provide the free energy for the wave growth. These observations are analogous to the drift resonance interaction that occurs, but is difficult to observe, in Tokamak reactors.

Takahashi et al. (2018) identified a fundamental standing mode 9 mHz Alfvén wave in the dawn sector at $L \sim 5.7$ and showed that the wave grew from drift resonant ~ 140 keV H^+ ions with an earthward phase space density gradient. The study linked the relatively low azimuthal wavenumber ($m \sim 40$, ~ 0.6 hr MLT) to the distinctive ground signature of a giant pulsation close to the magnetic footpoints of the satellites. Simultaneous ground and space-based observations of this type are critical to interpreting the magnetospheric origins of ground magnetometer signatures. Other similar studies include Min et al. (2017), Takahashi et al. (2018), and Takahashi et al. (2020).

In contrast to the coherent wave-particle interactions provided by shock-driven or standing mode ULF waves, ULF waves also provide diffusive energization, transport, and loss. A quasi-linear framework is typically employed to quantify this interaction, utilizing bounce- and/or drift-averaged diffusion coefficients calculated separately for the compressional magnetic field and azimuthal electric field (e.g., Ali et al. 2016). Historically, generation of parameterized coefficients for use in radiation belt models has involved heavy spatial (bounce and drift motion) and activity level (K_p) averaging to make up for limited data. However, averaged coefficients lack the resolution to capture the rapid, orders of magnitude changes associated with storm development. Sandhu et al. (2021) used EFW wave data to derive storm phase-dependent radial diffusion coefficients without significant averaging. They found that the diffusion coefficients can vary by orders of magnitude during storms, increasing during the late initial phase and reaching a maximum during the late main phase. These results have significant implications for understanding the time-dependent role of ULF-driven radial diffusion during dynamic times.

2.5 VLF Waves and Kinetic Scale Electric Field Structures

The EFW data set has enabled significant advances in understanding the roles of waves, including kinetic Alfvén waves (KAWs), ion cyclotron waves, whistler mode hiss and chorus waves, and Time Domain Structures. These waves transfer energy and momentum between different particle populations and different regions within the magnetosphere. Prior to the Van Allen Probes, observations of these waves and structures could be obtained only from short (few second) waveform bursts triggered on large amplitudes, or from low time resolution spectral data where short-duration impulsive structures appear as broadband noise. The long duration, high resolution burst waveforms and filter bank peak amplitudes obtained by EFW allowed correct identification of wave modes and structures, as well as accurate surveys of their occurrence. The following studies highlight discoveries that improved our understanding of adiabatic and non-adiabatic energization by electromagnetic and electrostatic waves, a major science goal for EFW.

The importance of long duration waveform bursts is clearly demonstrated in Fig. 7 (Malaspina et al. 2018b), which shows examples of different wave types that occurred during a 45 min interval of continuous 16,384 S/sec waveform data taken near an injection front. Kinetic Alfvén waves, non-linear whistlers, and solitary waves (Time Domain Structures) were observed, and their effect on the evolution of the injection front was significantly different than inferred from previous (limited) satellite data. For example, signatures of non-linear interactions in the whistler mode waves were observed at smaller amplitudes than had previously been thought possible, and the electrostatic potential of the solitary waves was shown to be significantly smaller than previously estimated. These results have important implications for the evolution of injection events as they propagate from the tail region to the inner magnetosphere (e.g., Vasko et al. 2017a).

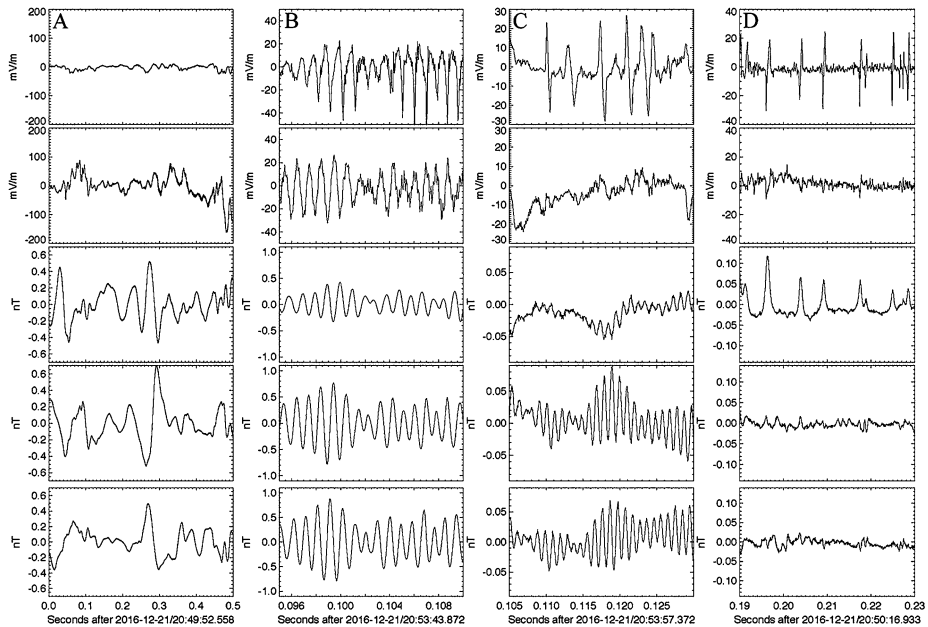


Fig. 7 (Adapted from Malaspina et al. 2018b) Examples of EFW burst waveform data showing various wave types observed in association with an injection event at 20:48 UT near $L \sim 5.4$. Each column presents (top to bottom) parallel and perpendicular components, respectively, of the electric field (2 components – no spin axis data were used) and magnetic field (3 components). Waveforms observed are consistent with kinetic Alfvén waves (column A), nonlinear whistler mode waves (column B), solitary waves (column C), and solitary waves with associated magnetic field enhancements (column D)

Kinetic Alfvén Waves Alfvén waves are a fundamental mode of energy transfer in the magnetosphere, particularly during geomagnetically active times (e.g., Wygant et al. 2002; Keiling et al. 2003). This mode exists across a spectrum of transverse scale sizes, and, at sufficiently short transverse scales (i.e. at ion gyroradius, ion acoustic gyroradius, or electron inertial length scales and below), these waves become dispersive, signified by E/B ratios that sharply increase from the Alfvén speed with increasing frequency. In the inner magnetosphere dispersive Alfvén waves have ion gyroradius transverse scales, which are in the kinetic Alfvén wave regime (Lysak and Lotko 1996) and thus generally referred to as kinetic Alfvén waves (KAWs).

Prior to the Van Allen probes mission, the occurrence and properties of KAWs in the inner magnetosphere were not well-established. A major discovery utilizing EFW data was that KAWs are a common feature of the nightside inner magnetosphere outside the plasmasphere during times of energetic plasma injections (Chaston et al. 2014, 2015a; Hull et al. 2019, 2020). The dual Van Allen probes EFW electric and EMFISIS magnetic field measurements revealed that KAWs occur as intense broadband bursts of electromagnetic activity over a very large MLT and L-shell extent of the nightside inner magnetosphere, with the largest amplitudes peaking at localized magnetic field dipolarizations (e.g., Fig. 8; Chaston et al. 2014; Malaspina et al. 2015; Hull et al. 2019, 2020). Statistical occurrence rates showed that KAWs are most prevalent during the main phase of geomagnetic storms but can extend well into the recovery phase (Chaston et al. 2015a), and are strongly associated with hot plasma injections, auroral activations, and shock impacts (Chaston et al. 2014; Moya et al. 2015; Malaspina et al. 2015; Hull et al. 2019, 2020). Comparisons with measurements

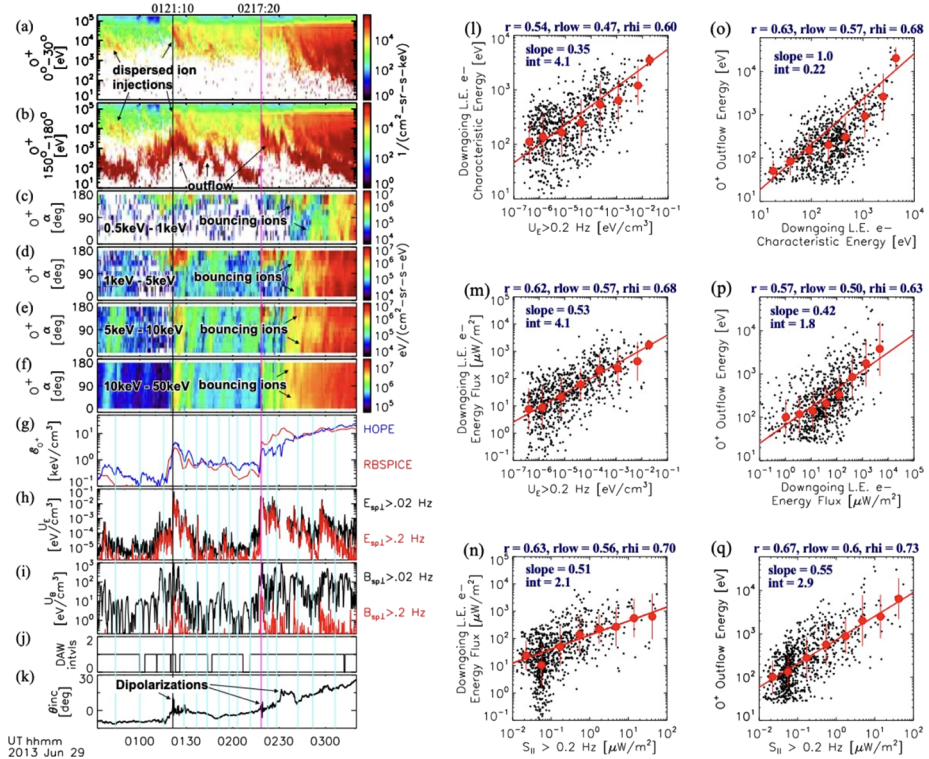


Fig. 8 (Adapted from Hull et al. 2019, 2020) Association between kinetic Alfvén waves and O^+ outflow on Van Allen Probe B for a geomagnetic storm that commenced on June 28, 2013. **(a, b)** O^+ number flux spectra in parallel and antiparallel directions showing clear outflow in the antiparallel direction. **(c–f)** Pitch angle spectra at various energies, and **(g)** the O^+ energy density. Enhancements are associated with increases in the electric field **(h)** and magnetic field **(i)** energy densities. **(j)** indicates intervals of kinetic Alfvén waves, and **(k)** shows the magnetic field inclination angle showing dipolarizations. For identified KAW intervals during the main and recovery phase of the storm, panels **(l–m)** compare KAW electric field energy densities with downgoing field-aligned electron characteristic energies, energy fluxes, and KAW parallel Poynting fluxes with downgoing KAW accelerated electron energy fluxes, respectively. Panels **(o–q)** compare O^+ outflow energy with downgoing field-aligned electron characteristic energies, energy fluxes, and KAW parallel Poynting fluxes, respectively. The red lines, dots and bars show linear fits, averages and standard deviations. Correlation coefficients and 99% confidence low and high limits are listed above each panel demonstrating statistically significant correlations between the compared quantities

performed at larger geocentric distances indicate that these fluctuations form the inner portion of an Alfvén wave distribution extending outward into the near-Earth plasma sheet and its boundary layers (Chaston et al. 2012; Wygant et al. 2002).

During geomagnetic storms, KAWs in the inner magnetosphere are invariably observed coincident with counterstreaming field-aligned electrons at energies of several keV and below, and O^+ ion outflow at energies up to several tens of keV (Chaston et al. 2015b; Hull et al. 2019, 2020). Additionally, correlations of KAW energy densities and Poynting flux have been made with O^+ outflow (Gkioulidou et al. 2019; Hull et al. 2020), ingoing electron characteristic energies and energy fluxes, and outflowing O^+ energies and energy densities (Hull et al. 2019, 2020). These correlations indicate that dispersive Alfvén waves are playing an essential role in controlling O^+ outflow along magnetic field lines into the equatorial

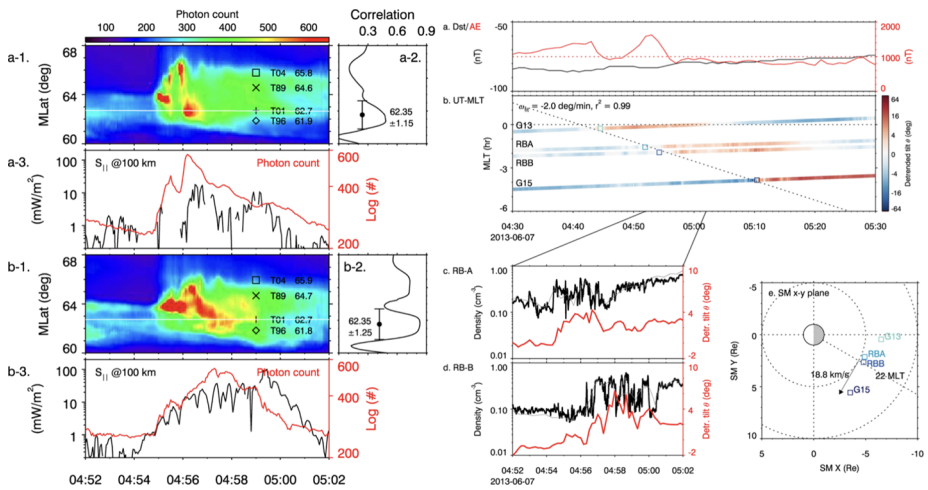


Fig. 9 (Adapted from Tian et al. 2021) (left) – The auroral brightness (red) correlated to Poynting flux (black) at Van Allen Probes A and B (a-3 and b-3) footprints, which were 0.5 h apart in MLT, during the westward and poleward expansion of a discrete arc. (a-1 and b-1) show keograms of the aurora and (a-2 and b-2) show the correlation analysis. Around the time of auroral expansion, a dipolarization was observed to propagate westward at 2 deg/min (second panel on right). This speed is much smaller than the westward expansion of the aurora (13.6 deg/min, not shown)

inner magnetosphere. This may occur by KAWs enhancing “soft” electron precipitation into the topside ionosphere in combination with subsequent transverse O^+ energization along the magnetic field line (e.g., Strangeway et al. 2005; Artemyev et al. 2015; Damiano et al. 2018).

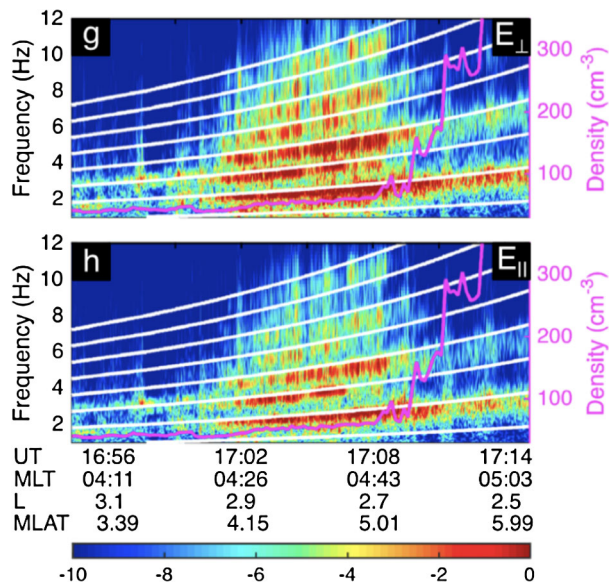
Given the global field-aligned extent of these waves, this energization process can occur all along the magnetic field line, and when combined with the magnetic mirror force, can result in field-aligned ion beams at energies up to 10 keV in the equatorial plane (Chaston et al. 2016). This may ultimately lead to significant, if not dominant, enhancements to ring current pressure (Chaston et al. 2015b; Hull et al. 2019, 2020), as indicated in Fig. 8 panel g.

A recent study by Tian et al. (2021) (Fig. 9), based on THEMIS all-sky imager data conjugate with the Van Allen Probes near the plasmasheet boundary layer, reported strong temporal and spatial associations between Alfvénic Poynting flux and discrete auroral arc brightenings. These observations indicate that structured Alfvén waves play a stronger role than previously thought in driving electron acceleration leading to auroral arc motion, contradicting the idea that auroral motions are associated with the motion of dipolarization, as the two motions were not correlated in this event.

Ion Cyclotron Harmonic Waves Ion cyclotron harmonic waves are an important component of the inner magnetosphere low frequency wave spectrum. These are most commonly observed as left-hand polarized waves with frequencies near the cyclotron harmonics of H^+ and He^+ (typically a few Hz, coined Electromagnetic Ion Cyclotron (EMIC) waves). They are associated with enhanced perpendicular temperature anisotropies from dayside magnetosphere compressions (typically H^+ band) or with afternoon to nightside injections of plasmasheet ions (typically for the He^+ band).

Posch et al. (2015) performed a statistical and event study using EFW and EMFISIS data to show that compressional electromagnetic waves generated at harmonics of the local

Fig. 10 (Adapted from Usanova et al. 2016) An example of the parallel and perpendicular electric field components of an oxygen cyclotron harmonic wave. Density derived from EFW probe potentials is shown as the magenta curve. The color represents the electric field log power spectral density ($\text{mV/m}^2/\text{Hz}$)



proton cyclotron frequency (aka fast magnetosonic waves) were observed both inside and outside of the plasmasphere, with maximal occurrence from noon to dusk and within 3 hours following substorm injections. By using the observed frequency spacing between proton harmonics, they inferred that the origin of these waves was within 2 L-shells *outside* the plasmapause boundary.

Usanova et al. 2016 used 32 Sample/sec EFW waveform data to discover a population of *oxygen cyclotron harmonic* (OCH) waves at frequencies near the oxygen cyclotron frequency and its harmonics, associated with increases in ring current O^+ flux during storm main phase. These waves, shown in Fig. 10, are typically parallel propagating with amplitudes of 0.1–5 mV/m and 0.1–5 nT, and likely provide important scattering loss of resonant O^+ ring current ions. They are also linked to relativistic (MeV) electron loss leading to rapid radiation belt flux dropouts in the inner magnetosphere (Qin et al. 2019), and may indirectly contribute to electron loss and energization via cross-frequency coupling with VLF waves (Usanova et al. 2018; Colpitts et al. 2016).

Chorus Waves Chorus are intense whistler-mode waves commonly observed in the low-density inner magnetosphere outside of the plasmasphere in association with substorm injections of energetic electrons. They drive both significant energetic electron loss and acceleration via Landau or cyclotron resonances, processes typically described in a quasi-linear framework (Horne et al. 2016). Populations of extremely large amplitude chorus waves (tens of mV/m) also exist, as discovered by Cattell et al. (2008) with STEREO satellite burst waveform data, and these waves have a strongly nonlinear interaction with electrons leading to rapid scattering and acceleration. Prior to the Van Allen Probes, statistics of large amplitude waves were severely lacking due to instrumental limitations. EFW was well-suited to make observations of waves over a wide range of amplitudes, and several studies using high time resolution burst and filter bank data have since provided insight into the importance of nonlinear whistler mode waves in radiation belt dynamics.

Tyler et al. (2019a) examined the temporal and spatial occurrence of moderate to large amplitude lower band chorus with EFW filter bank electric field data. This instrument pro-

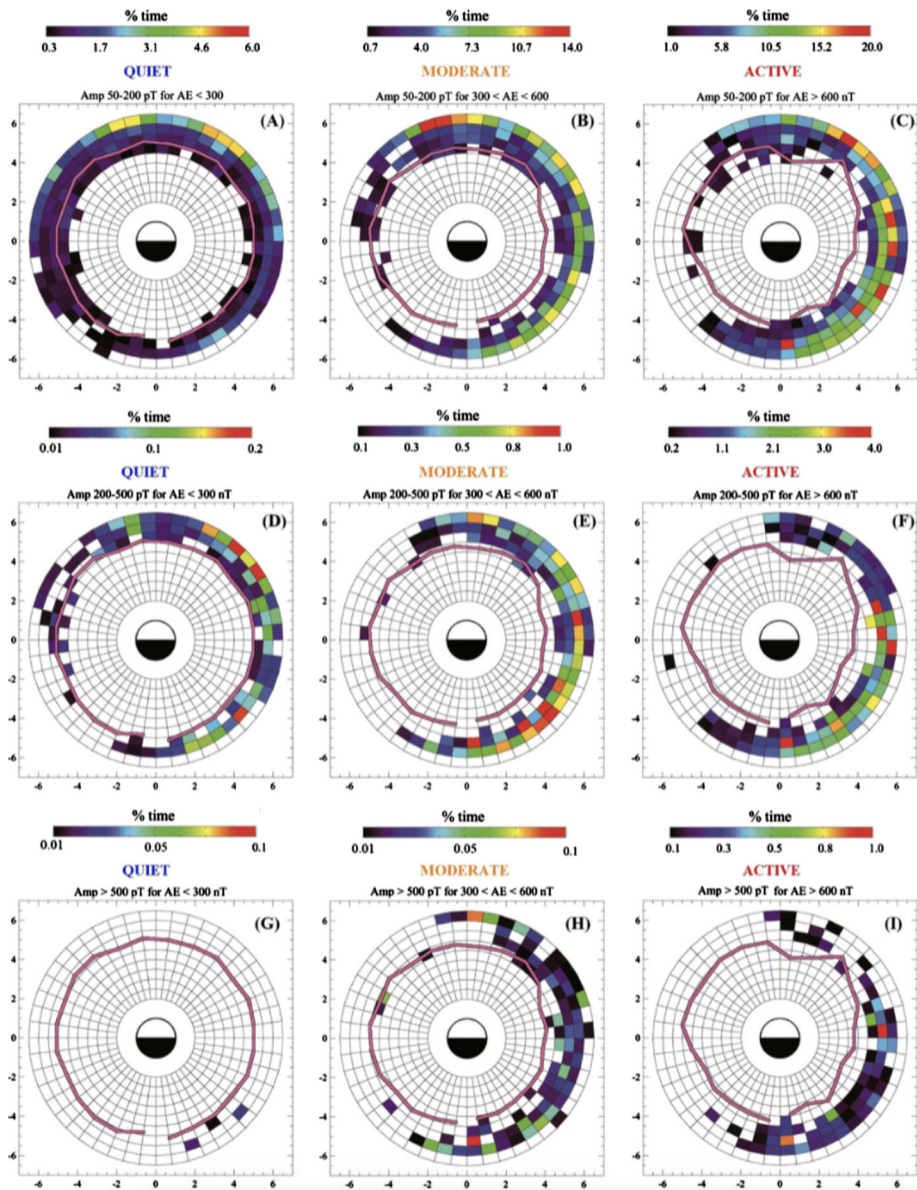


Fig. 11 (Adapted from Tyler et al. 2019a) The percent occurrence of whistler mode waves separated by geomagnetic activity for amplitudes between 5 and 20 mV/m (a–c), amplitudes between 20 and 50 mV/m (d–f), and amplitudes greater than 50 mV/m (g and h). The average plasmapause location for each range of geomagnetic activity is indicated by the pink line

vides a full duty cycle record of peak (and average) wave amplitudes in a variety of frequency bins at 8 S/sec, effectively counting the peak amplitude of individual chorus wave packets. As shown in Fig. 11, large amplitude chorus waves (50–200 pT) can be common during geomagnetically active times, with a 30% occurrence in some regions. Compari-

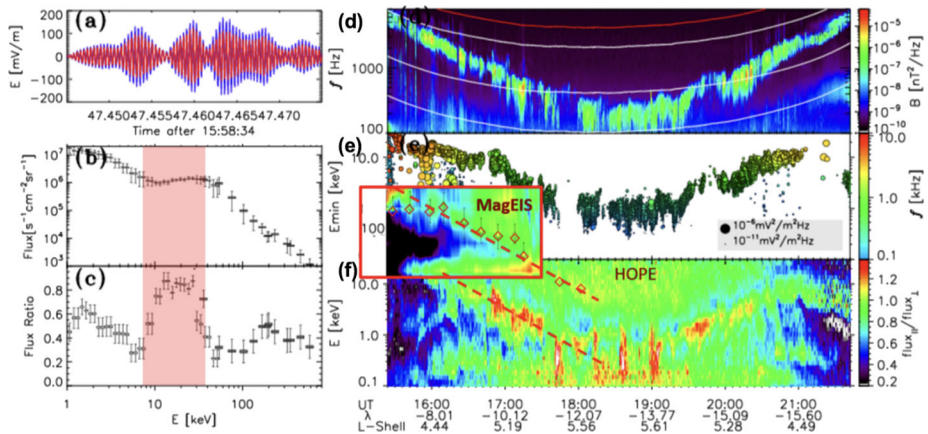


Fig. 12 (Adapted from Agapitov et al. 2015) (a) Very oblique, high-amplitude chorus with a ~ 100 mV/m parallel electric field component. (b, c) HOPE and MagEIS observations showing the flux of the Landau-resonant electrons (red stripe) and the ratio of parallel to perpendicular flux vs energy. (d) Spectrogram of the magnetic field component of observed chorus waves. (e) Resonant energy of the chorus waves, with the color indicating frequency, and (f) HOPE and MagEIS (inset) observations of the flux ratio showing the accelerated electrons, along with confirmation from a test-particle model (diamonds)

son to the occurrence in the magnetic field filter bank data (Tyler et al. 2019b) indicated that large amplitude waves were primarily oblique (and thus more electrostatic) at low L , while dayside and high L populations are primarily field aligned. These studies, although not providing detailed spectral and wave angle information that is important for understanding chorus interaction with electrons, suggest that nonlinear chorus can occur in large enough numbers that they may be of importance to electron acceleration and loss (e.g., Bortnik et al. 2016).

In addition to amplitude, wave obliquity, defined as the angle of the wave vector to the magnetic field, has a strong effect on the interaction with electrons. This was clearly demonstrated by Agapitov et al. (2015) (Fig. 12) who used Van Allen Probes wave and particle measurements, along with a test-particle simulation, to show that oblique, large amplitude chorus waves with a strong parallel electric field component can provide strong acceleration of ~ 1 – 10 keV electrons to ~ 100 – 200 keV via Landau resonance. Panels (b, c) show a resonant ~ 10 keV population (trapped in the wave potential) with a characteristic plateau in parallel energy, and panel (f) shows the subsequent accelerated population, clearly identified by an abnormally large ratio of parallel to transverse flux. This interaction was widespread ($L = 4$ – 6) and long-lasting (6 hrs) and can therefore provide a significant and rapid source of electrons that can act as the seed population for later acceleration to relativistic (MeV) energies. Comprehensive results such as these are also critical input to models of the growth of highly oblique, lower band chorus waves (Mourenas et al. 2015), which had not been previously explained.

At higher latitudes (> 20 deg, and beyond the orbit sampled by the Van Allen Probes) chorus waves can become highly oblique due to refraction and are thought to provide important scattering with relativistic (hundreds keV) electrons (e.g., Horne and Thorne 2003). Agapitov et al. (2018a) combined Cluster spectral data and Van Allen Probes EFW and EM-FISIS spectral observations to obtain a model parameterizing chorus wave power as a function of geomagnetic activity level and spatial location including magnetic latitude. These wave statistics are critical for properly characterizing the interaction of chorus and electrons

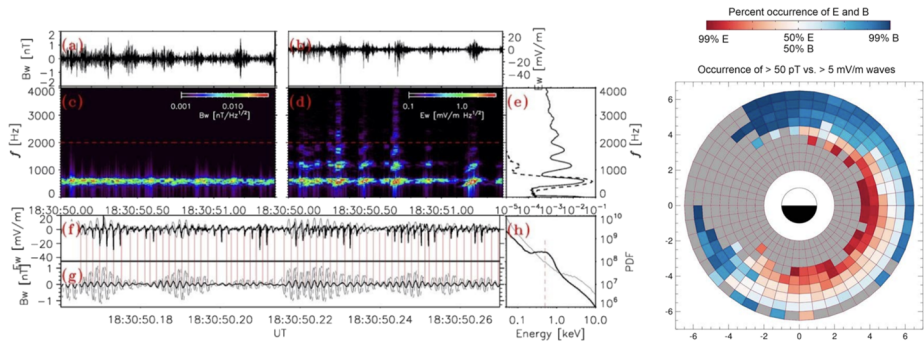


Fig. 13 (Adapted from Agapitov et al. 2018b (left) and Tyler et al. 2019b (right)) Left plot: Van Allen Probe A magnetic and electric field waveforms (a, b), their spectra (c, d), and zoomed in views (f, g) on 2013-04-24. Total power for each frequency is shown in panel (e) for the magnetic field (dashed curve) and electric field (solid curve). Panel h shows the electron energy spectrum along (solid) and perpendicular (thin curve) to the magnetic field. Right plot shows a population of large amplitude, highly oblique lower band whistler mode waves identified with filter bank data outside of the plasmasphere by Tyler et al. (2019b) that may be the result of this interaction

and show that quasi-parallel wave modes significantly underestimate the true levels of electron energization and precipitation into the atmosphere due to the far more oblique waves that are actually present (Artemyev et al. 2016; Agapitov et al. 2019).

In the presence of hot resonant electron beams, even moderate amplitude and moderately oblique whistlers can become highly non-linear. Agapitov et al. (2018b) used EFW observations combined with a particle-in-cell simulation to show how electrons modulated by a whistler wave can produce a hot electron beam-driven electrostatic mode which then interacts with the original whistler mode wave. As shown in Fig. 13, this coupling causes significant distortion and enhancement of the parallel electric field including the introduction of power at higher harmonics (e.g., Kellogg et al. 2010). The resulting beam-driven electrostatic acoustic mode can be an effective accelerator of energetic electrons. This interaction may explain the population of large-amplitude, highly electrostatic and large amplitude whistler mode waves observed by Tyler et al. (2019b) in EFW filter bank data near the nominal plasmopause location (Fig. 13, right panel).

Critical to the importance of nonlinear interactions between chorus and electrons are the spatial scales of the wave amplitude and wave coherence. The dual Van Allen Probes had several close passes (lapping events) during the mission with orbital track separations as low as ~ 100 km, providing a near ideal experiment to study these critical parameters for chorus waves. Agapitov et al. (2017) analyzed five hours of EFW burst waveform data around two consecutive apogees within the chorus generation region when the separation between the two Probes ranged from ~ 100 to 5000 km. Figure 14 shows an example of chorus waves on both spacecraft. The correlation coefficients of wave amplitude between each were analyzed, with the results in the right panel indicating that the maximum source size (at which a single chorus element could be observed on both spacecraft) for lower band chorus was 600–800 km. The scale of phase coherence (not shown), in contrast, was only 150–200 km. The latter is critical for characterizing the nonlinear interaction that produces energetic electron microburst precipitation, shown by Shumko et al. (2018) to have a similar scale size when mapped to the magnetic equator. This study was followed up by Agapitov et al. (2021) who analyzed nearly eight years of lapping events with 8 S/sec EFW filter bank data to find significant transverse correlation in the 400–750 km range, with size increasing with L-shell.

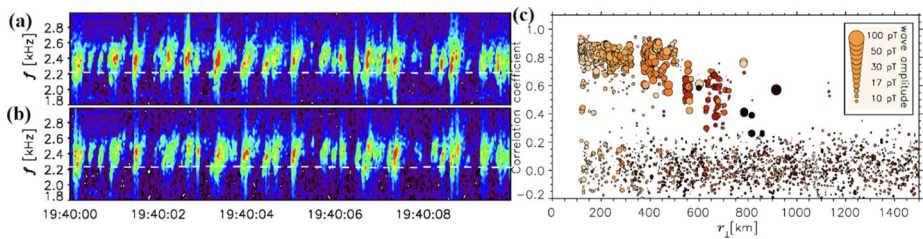


Fig. 14 (Adapted from Agapitov et al. 2017) Left plot shows a selection of chorus waves (Probe A top panel, Probe B bottom panel) observed during 17–22 UT in which continuous EFW high time resolution burst data were available and the inter-spacecraft separation was less than 200 km. The dashed line indicates 0.1 times the electron cyclotron frequency. The right plot shows the distribution of correlation coefficients calculated from 10 sec time intervals during 17–22 UT, with wave amplitude indicated by the circle size

Plasmaspheric Hiss Waves Whistler mode plasmaspheric hiss, an unmodulated and broadband emission on a frequency-time spectrogram, is found within the plasmasphere and plumes. Hiss drives electron scattering loss to the atmosphere following the main phase of a storm, leading to the recovery of the outer belt and the formation of the slot region (e.g., Ripoll et al. 2014). Loss rates depend critically on hiss wave properties, traditionally parameterized with wave magnetic field measurements with respect to activity level (K_p) and spatial location (L , MLT, magnetic latitude). However, this parameterization ignores the fact that hiss is found only within the plasmasphere, which itself varies in size and shape with L and magnetic activity. Malaspina et al. (2016, 2017, 2018a) used Van Allen Probes data to provide a natural sorting of hiss (and other) waves by relative distance to the plasmapause. The plasmapause location was identified using high-spatial-resolution density values determined from EFW spacecraft potential. Comparing the left and right columns in Fig. 15 shows that this sorting gives a much more natural representation of hiss waves. A surprising result is that this simplified parameterization is repeatable in power distributions that are largely independent of activity level (AE) and MLT, but depend mostly on local plasma density. Recent studies including Malaspina et al. (2020) have qualitatively assessed the impact of this parameterization on predictive radiation belt models, showing significant differences in electron lifetimes as compared to the traditional parameterization.

Time Domain Structures One of the more surprising results from the Van Allen Probes mission was the discovery by Mozer et al. (2013) that short-lived, impulsive electric field structures, called Time Domain Structures (TDS), occurred in very large numbers in the inner magnetosphere. This discovery was made possible by EFW's high time resolution, DC-coupled burst waveform data. TDS include electron holes, double layers, and nonlinear whistler mode waves. Although impulsive structures had been previously known to exist in many regions, including along auroral field lines (Temerin et al. 1982; Ergun et al. 1998), at the bow shock (Bale et al. 1998), magnetopause (Cattell et al. 2002; Ergun et al. 2016), in magnetotail reconnection regions (Cattell et al. 2005), and at the plasma sheet boundary layer (Andersson et al. 2009), they had not been observed in the inner magnetosphere prior to the Van Allen Probes. Figure 16 illustrates examples of TDS from EFW burst data. The top panels show closeup views of a few TDS (Mozer et al. 2016) clearly displaying the typical bipolar parallel electric field signatures. The EFW instrument was able to collect waveform data for much longer time periods than any other mission, providing clear evidence for the long duration of intervals filled with these structures and their occurrence rate. An example illustrating large numbers of TDS (electron phase space holes) obtained upstream of a sub-storm dipolarization front is shown on the bottom (Malaspina et al. 2014b). Clear evolution

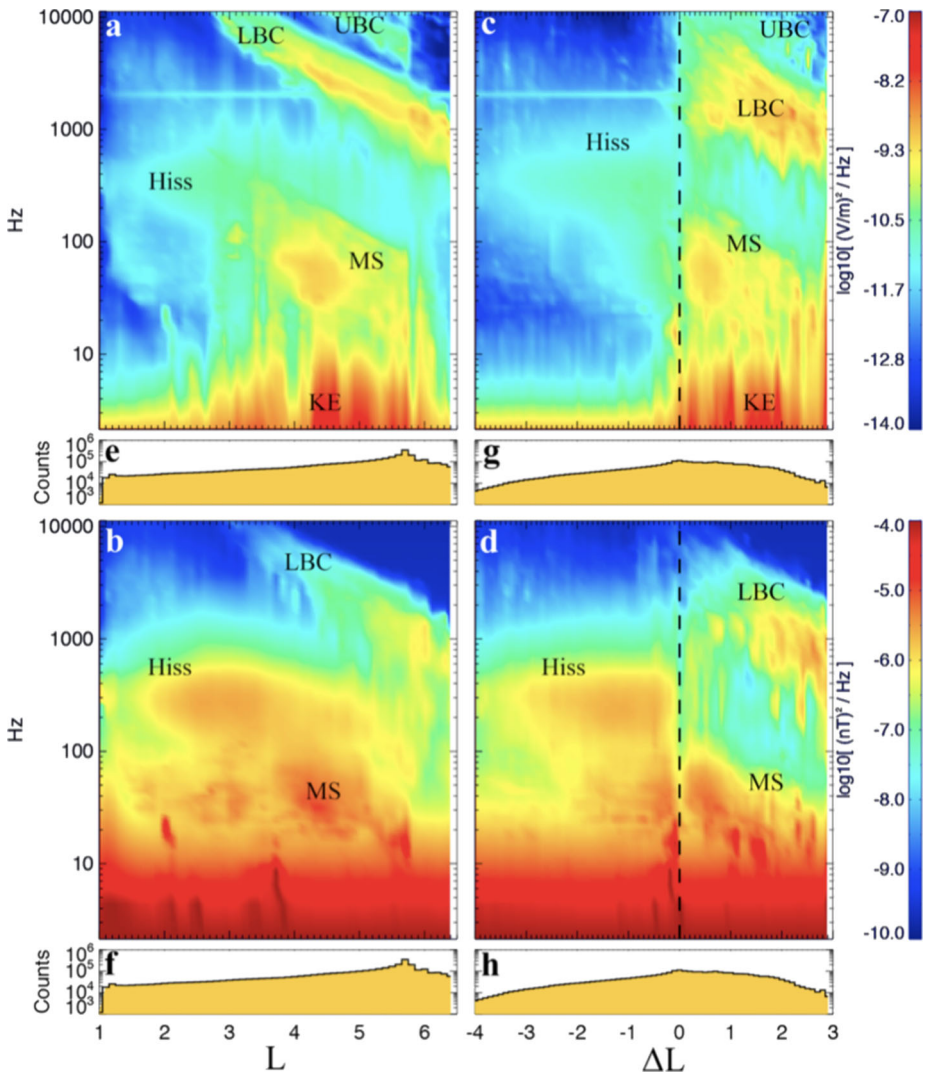
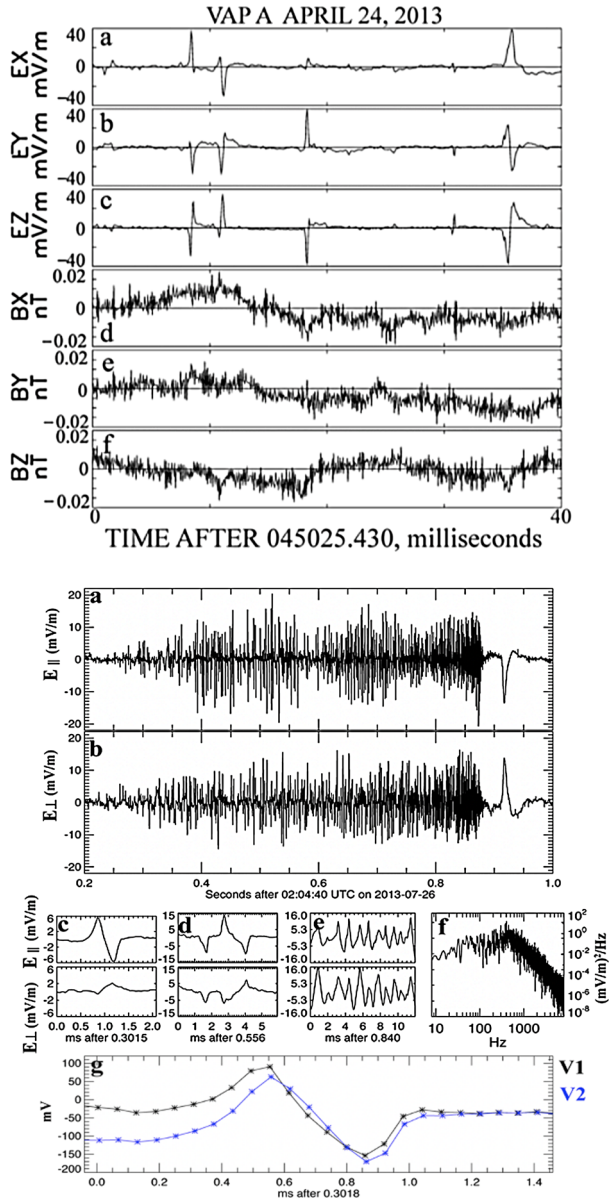


Fig. 15 (Adapted from Malaspina et al. 2016) Comparison of hiss electric (EMFISIS via onboard shared channel with EFW) and magnetic field (row 1) and magnetic field amplitudes (row 2) from ~ 3 years of Van Allen Probes data traditionally sorted (column 1, frequency vs L) vs relative sorting (column 2, frequency vs distance from plasmapause). The plasmapause location on each inbound or outbound orbit was determined as the innermost crossing of 100/cc density values as determined from EFW spacecraft potential. The wave groups indicated are upper and lower band chorus (UBC, LBC), plasmaspheric hiss, magnetosonic (MS), and kinetic-scale electric field structures (KE)

of the structures with respect to upstream distance from their source plasma double layer is seen in panels c–e.

The fast sampling rate of the EFW burst data (16,384 S/sec), combined with the long EFW booms in the spin plane (~ 100 m tip-tip double sensor separation), allowed interferometric timing analysis to determine the TDS propagation velocity (Fig. 16 panel g). This velocity, typically along the magnetic field, allows one to estimate both the energy

Fig. 16 (Adapted from Mozer et al. 2016 (top) and Malaspina et al. 2014b (bottom)) Examples of TDS from the AC-coupled EFW burst 2 data. The top panels show a close-up view of TDS electric (spin plane and spin axis components) and magnetic field signatures, most showing a typical bipolar structure. The bottom panels (a, b) show 160 msec of data showing hundreds of TDS upstream of a substorm dipolarization front. Panels (c–e) show how the character of the TDS changes with distance from the front, and panel f shows their broadband nature in frequency space. Panel (g) shows the single sensor voltages used in an interferometric timing analysis



of Landau-resonant electrons, as well as the net electric potential across the TDS. Rapid parallel acceleration (within a bounce period) occurs as trapped electrons are carried into regions of higher magnetic field (Mozer et al. 2016; Vasko et al. 2017b). Slow-propagating electron acoustic TDS (~ 3000 km/s) can accelerate thermal electrons to several keV energies (Artemyev et al. 2014), and can result in precipitation including pulsating auroras (Mozer et al. 2017; Shen et al. 2020). An example is shown in Fig. 17 (Vasko et al. 2015). The left-hand panels plot spectra of the electric and magnetic fields and the electrons over a ~ 30 min interval. The broadband spikes are caused by intense TDS electric field spikes

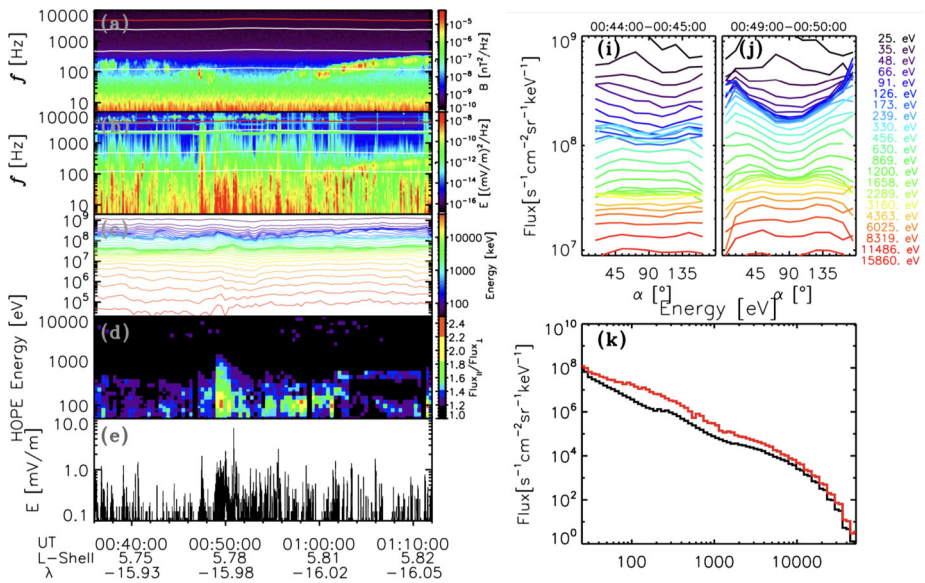


Fig. 17 (Adapted from Vasko et al. 2015) Van Allen Probe B observations on November 13, 2012 showing field-aligned electron pitch angle distributions accelerated by Time Domain Structures. Panels (a, b) show the magnetic and electric field power spectra showing broadband spikes that are the TDS. Panel (d) shows the ratio of parallel to perpendicular sub-keV electron fluxes from the HOPE instrument, with an enhancement corresponding to the increase in TDS activity in panels (b) and (e). Panels (i) and (j) are HOPE pitch angle distributions before and during the increase in TDS activity showing clear increases in field-aligned flux at < 1 keV energies. Panel (k) shows the omnidirectional flux vs energy before (black) and during (red) the TDS

(panel d) associated with an enhancement in the ratio of parallel to perpendicular electron flux at sub keV energies (panel d). The right panels show that the initially almost isotropic distribution (i) becomes more field-aligned and enhanced (panel k) at energies up to about 1 keV coinciding with the onset of the TDS.

Fast-propagating TDS ($\sim 20,000$ km/s), thought to be generated by oblique whistlers or kinetic Alfvén waves (An et al. 2021), can provide significant Landau acceleration of near-relativistic electrons (~ 100 keV) in the field-aligned direction (Kellogg et al. 2011; Mozer et al. 2016). This interaction may be a critical step in dramatic outer belt energizations (e.g., Jaynes et al. 2015) that follow storm time dropouts by providing the seed population that chorus waves then rapidly accelerate to MeV energies (Mozer et al. 2016).

2.6 Summary

The Van Allen Probes EFW instrument has provided significant advances in our understanding of the radiation belts and inner magnetosphere, as demonstrated by the limited selection of results described in this section. Much remains to be uncovered in this rich dataset, and future studies will continue to provide insights into the dynamics of the inner magnetosphere.

3 Science Results from Collaborative Campaigns

Untangling the spatial and temporal variations in loss and acceleration processes is a fundamental requirement for understanding the dynamics of the inner magnetosphere. This

requires near-simultaneous multi-point observations and is the primary motivation behind the current trend of multi-satellite missions including the Van Allen Probes (2 sc), THEMIS (5 sc), Cluster (4 sc), MMS (4 sc) and others. One way to obtain the necessary measurements is to combine data sets from big-budget, fully instrumented satellite missions with data from instruments on low cost ground-based networks, rockets, balloon arrays, and small satellites including CubeSats. Under this paradigm, collaboration between multiple missions is critical for maximizing the scientific data return. Throughout the Van Allen Probes mission, the EFW team collaborated with other mission teams to develop focused data collection campaigns, as described in Manweiler et al. (this journal). Of all these campaigns, this section focuses on the important scientific results from campaigns with the Balloon Array for Radiation-belt Relativistic Electron Losses (BARREL, Millan et al. 2013; Millan et al. this journal) mission, the FIREBIRD II (henceforth FIREBIRD; Klumpp et al. 2015; Crew et al. 2016) and AeroCube-6 (AC-6; e.g., Blake and O'Brien 2016; O'Brien et al. 2016; Shumko et al. 2020) CubeSats, the World Wide Lightning Location Network (WWLLN; Dowden et al. 2002), and the Arase spacecraft (Miyoshi et al. 2018).

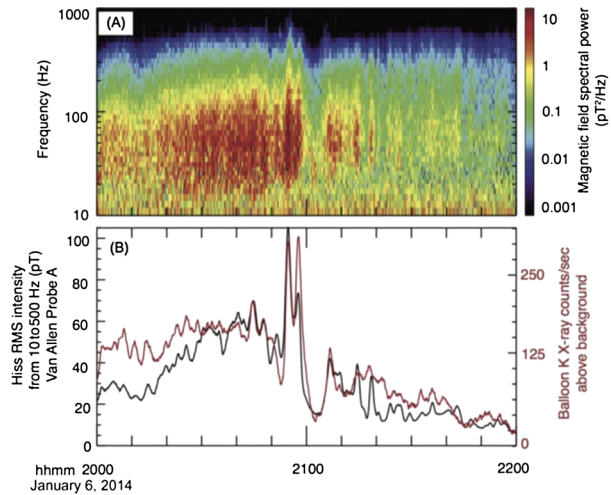
3.1 Science Results from EFW and BARREL

The BARREL mission was a mission of opportunity with the Van Allen Probes (Millan et al. 2013). Over the course of six campaigns, balloons were launched from locations in Antarctica and Kiruna, Sweden to measure X-rays caused primarily by precipitating electrons of tens to hundreds of keV in energy. Typically aloft for multiple days, they drifted across a range of magnetic field lines threading the magnetosphere, leading to frequent magnetic conjunctions with the Van Allen Probes. Breneman et al. (2015) analyzed data from a near perfect magnetic conjunction between a single balloon and Van Allen Probe A to identify distinctive modulations occurring in both plasmaspheric hiss amplitude and X-ray flux for two hours, as shown in Fig. 18. By inverting the X-ray spectrum into a precipitating flux spectrum, they were able to definitively show that observed hiss directly caused tens of keV electron loss in a manner consistent with quasi-linear scattering theory, the first such direct comparison. In addition, similar fluctuations of hiss and X-rays were observed on multiple other satellites and balloons spanning a large extent of MLT and L-shell, indicating that this loss process was coherent on a near global scale (see also Li et al. 2017). The cause of this modulation was not determined but was likely related to ULF waves generated either internally to the magnetosphere or externally from the magnetosheath, foreshock, or solar wind. Breneman et al. (2020) subsequently showed that global-scale coherence of waves and precipitation is a common feature of the dayside outer belt and can be driven by common dynamic solar wind pressure fluctuations (e.g., Kepko et al. 2002).

Prompt dayside compressions caused by shock impacts can also lead to enhanced electron loss. Halford et al. (2016) showed that sudden BARREL X-ray increases following a Jan 9, 2014 shock impact could be explained by a combination of enhanced scattering loss from chorus waves and adiabatic motion whereby previous trapped electrons near the loss cone find themselves within an expanded loss cone as they are transported earthwards by the shock-enhanced dusk-dawn electric field (e.g., Rae et al. 2018).

Chaston et al. (2018) combined BARREL and EFW observations during a nightside magnetic conjunction to show that kinetic Alfvén waves, previously identified to cause loss of ring current ions and drive radial electron transport, can provide rapid scattering loss of relativistic electrons throughout the outer radiation belt during geomagnetic storms. Modeling of pitch angle scattering based on the observations suggests that a drift-bounce resonance with the electron gyroradius scale waves caused the enhanced losses. Though this study only

Fig. 18 (Adapted from Breneman et al. 2015) Comparison of plasmaspheric hiss amplitudes and X-rays from precipitating electrons during an extremely close magnetic conjunction between Van Allen Probe A and BARREL balloon 2I. **(a)** Plasmaspheric hiss amplitudes observed on EFW spectral data. Panel **b** shows that the hiss RMS intensity has a very close correspondence with X-ray counts on 2I



focused on a single conjunction, the large populations of KAWs, particularly on the night-side during the storm main phase, suggest that this may be an important loss mechanism for energetic electrons. A study by Blum et al. (2015) supports this hypothesis, showing that the nightside MLT and L-shell distribution of KAWs bears a close resemblance to relativistic electron loss signatures derived from low altitude spacecraft.

3.2 Science Results Involving EFW and the CubeSat Missions FIREBIRD II and AC-6

EFW worked closely with both the low Earth orbiting FIREBIRD and AC-6 CubeSat teams over 18 focused (roughly month long) collaborative campaigns from early 2016 until the end of the Van Allen Probes mission in late 2019. The primary goal of these campaigns was to coordinate equatorial observations of waves with non-relativistic (> 30 keV dosimeter, AC-6) and relativistic (200 keV to $> \text{MeV}$, FIREBIRD) electron precipitation events. This precipitation commonly takes the form of impulsive (subsecond) events termed microbursts, and one of the important goals of the Van Allen Probes mission was to understand their cause and relevance to outer radiation belt dynamics (Mauk et al. 2013). EFW's collaborative effort with FIREBIRD and AC-6 resulted in a novel dataset of hundreds of hours of high time resolution waveform and particle measurements near magnetic conjunctions. For a detailed description of these campaigns see Johnson et al. (2020), Sample et al. (2020), and Spence et al. (this journal).

Using data during a particularly close conjunction, Breneman et al. (2017) established, for the first time, a direct connection between chorus and microbursts. Results are presented in Fig. 19, which shows similar cadences in chorus observed on Van Allen Probe A and microbursts on FIREBIRD (Flight Unit 4) occurring over 80 seconds during an outer belt conjunction near $\text{MLT} = 10.5$. Probe A observations for roughly 1 hour centered on this conjunction indicate that no other wave populations were observed during this time, so that the microbursts could only have been caused by the chorus waves.

Waveform and spectral observations from EFW and EMFISIS (via shared data channel) showed that the chorus waves consisted of parallel-propagating rising tones near the magnetic equator. This indicated that production of the observed > 200 keV to ~ 1 MeV microbursts likely occurred at higher magnetic latitudes ($> |20|$ deg) where the stronger

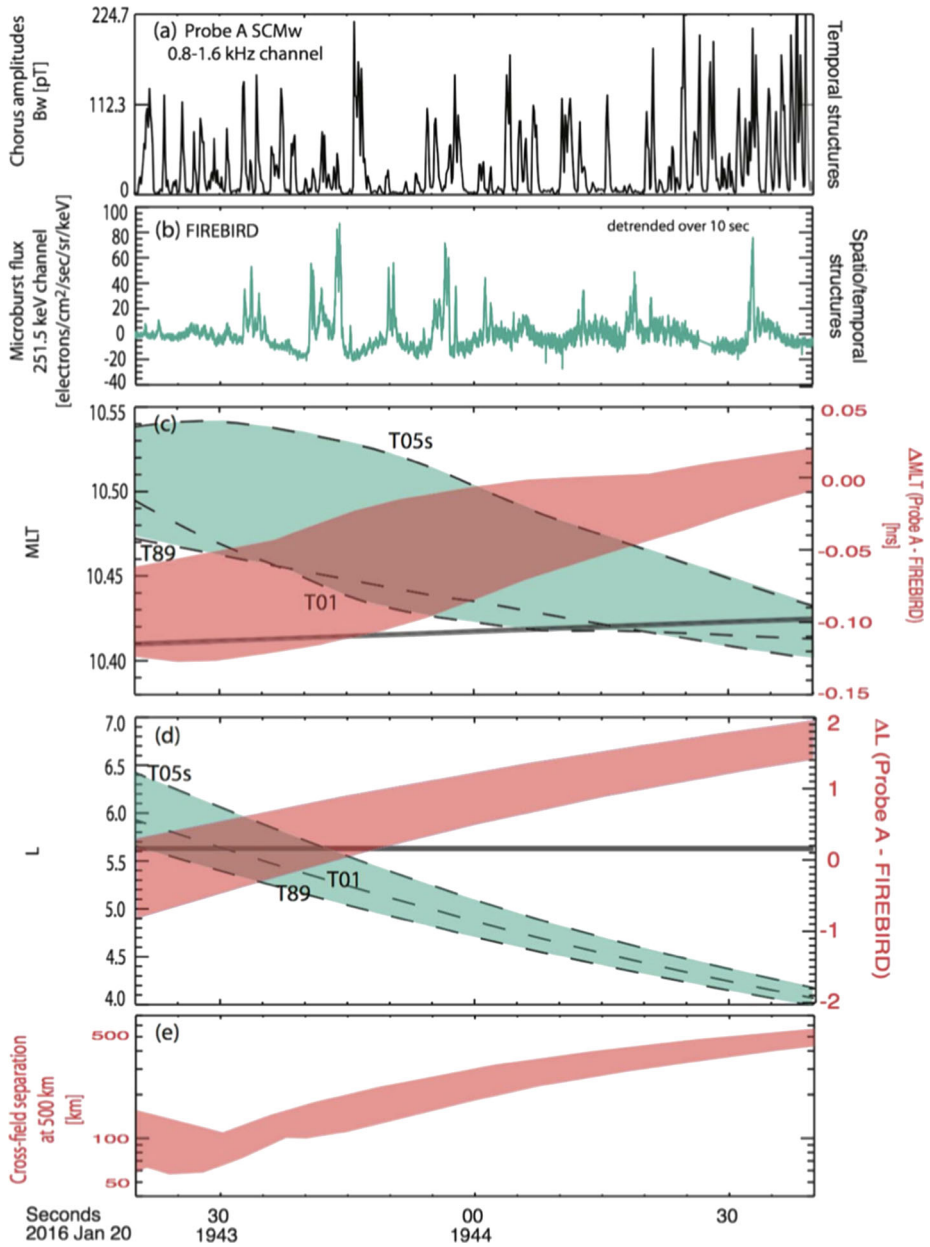


Fig. 19 (Adapted from Breneman et al. 2017) Close conjunction observations of chorus and microbursts on Van Allen Probe A and FIREBIRD Flight Unit 4, respectively. (a) Amplitudes from the EFW filter bank 0.8–1.6 kHz channel showing temporal variation of chorus waves. (b) FIREBIRD 251.5 keV channel flux, detrended over 10 sec, showing spatio/temporal variation of microbursts. (c) Magnetic local times mapped to the magnetic equator of Probe A (black line) and FIREBIRD. The range of FIREBIRD values represents uncertainty estimated from the use of different magnetic field models, including T89, T01, and T05s (e.g., Tsyganenko and Sitnov 2005). (d) Same as panel (c) but with L values instead of MLT. (e) Range of cross-field separations of Probe A and FIREBIRD Flight Unit 4 mapped to 500 km altitude based on panels (c, d)

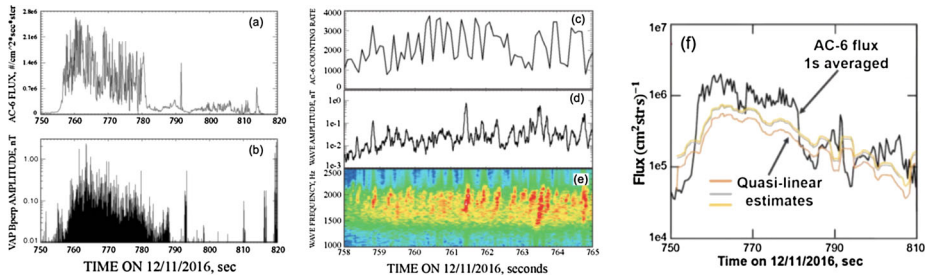


Fig. 20 (Adapted from Mozer et al. 2018) Comparison of AC-6 > 30 keV dosimeter counts showing (a) microbursts and (b) EFW observations on Van Allen Probe B of chorus intensity during a close magnetic conjunction. Panels (c–d) show a close-up comparison. Panel (f) shows a comparison of 1-sec averaged flux on AC-6 to quasi-linear estimates of the flux based on Van Allen Probes B observations

magnetic field and increased obliquity of the chorus waves increased the first order cyclotron resonance energy to these energies (as suggested by Horne and Thorne 2003). The importance of microburst loss to outer belt recovery depends critically on the spatial extent (L, MLT) and duration of the observed microburst flux, neither of which is well constrained by observations. Future observations involving constellations of observations will likely be necessary to quantify this loss process.

Another important result from the EFW and FIREBIRD/AC-6 collaboration was published by Mozer et al. 2018, who compared AC-6 > 30 keV dosimeter microburst flux with lower band chorus observed during a magnetic conjunction near $L = 6$. The intensity plots in Fig. 20 (panels a, b) clearly show a close correspondence between the microburst flux and the rising tone (panel e) chorus waves. Comparisons with quasi-linear scattering theory (panel f) indicated that, though the 1 sec averaged microburst flux is roughly similar to quasi-linear estimates, the spikier elements (< 0.5 sec) require a nonlinear explanation. This result thus emphasizes the fundamental nonlinear nature of the wave-particle interaction producing microbursts.

3.3 WWLLN Campaigns with EFW

For a few months in 2013 (Jul–Sep) and 2014 (Mar–Apr), EFW collaborated with a team from the World Wide Lightning Location Network (WWLLN, Dowden et al. 2002) in an effort to better understand the coupling of lightning sferics into lightning whistler mode waves in the magnetosphere, where they are known to drive electron loss from tens of keV to several MeV at $L < 2.5$ (Green et al. 2020). To guide the EFW burst data collection, the WWLLN team would first predict the most likely ten-minute timespan that each Van Allen Probe would be conjugate to thunderstorm activity based on the previous three years of optical WWLLN lightning stroke data. This resulted in a large amount of burst data collection, which at a sample rate of 16,384 S/sec could not all be telemetered. Efforts thus focused on small (typically 1–2 min) chunks of time when lightning was present within a 500–1000 km footprint separation of one of the Van Allen Probes. This scheme proved highly successful and culminated in the statistical study of Zheng et al. (2016). Their timing analysis was used to directly associate 22.9% of the whistlers observed in EFW burst data with a lightning stroke, most at $L = 1–3$. The analysis included modeling the whistler pulse dispersion associated with propagation along the magnetic field line to the Van Allen Probes, and then removing observed dispersion to obtain the original signal at the source (called ‘de-chirping’). Figure 21 shows an example of this analysis, demonstrating the close association

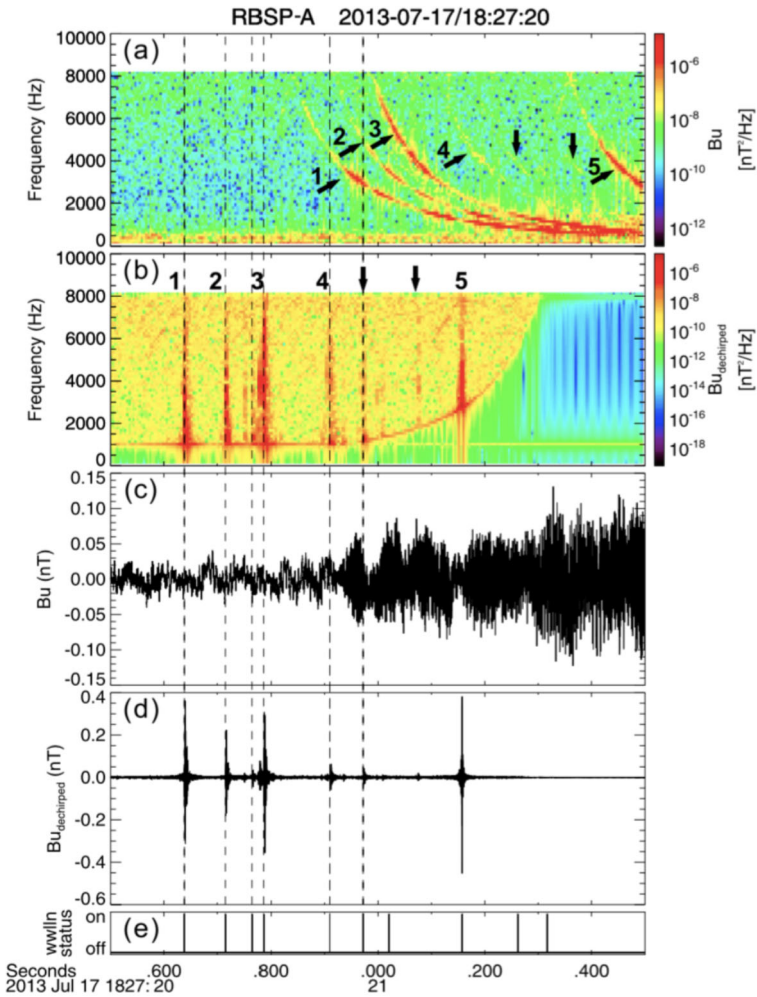


Fig. 21 (Adapted from Zheng et al. 2016) Comparison of lightning whistlers on Van Allen Probe A to WWLLN lightning strike flags. (a) Van Allen Probe A spectral data from EFW burst waveform data showing the magnetic signatures of multiple dispersive lightning whistlers. (b) De-chirped whistlers from (a). (c) Burst waveform data and (d) de-chirped burst waveform data corresponding to the spectrograms in panels (a, b). (e) WWLLN flags indicating times of lightning flashes

on a stroke-by-stroke basis between the de-chirped whistlers observed on EFW and the lightning pulse timing from WWLLN. This result is an important step towards classifying the coupling of lightning strokes to VLF wave power (e.g., Ripoll et al. 2019), and paves the way for independent use of WWLLN data for prediction of power input into VLF waves.

WWLLN and other ground station observations were combined with Van Allen Probes EFW and EMFISIS burst waveform data in a study of lightning whistlers driven by rare but extremely powerful superbolt lightning flashes (Ripoll et al. 2021). Though less common than typical lightning flashes, superbolts were shown to transmit 10–1000 times more VLF wave energy into the inner magnetosphere than typical lightning strokes, suggesting that

they may provide an important contribution to precipitation loss of electrons in the inner belt ($L \sim 1.1\text{--}2.5$).

3.4 Collaborations with Arase

The EFW team collaborated with the Arase satellite team (Miyoshi et al. 2018) to take joint observations of the inner magnetosphere, identifying and collecting burst data from over 500 conjunctions from 2017–2019. The higher orbital inclination angle of Arase, relative to the more equatorial orbit of Van Allen Probes, allowed observations at different latitudes but the same L-shell and MLT. This collaboration has significantly enhanced our understanding of the spatial and temporal structures of dynamic phenomena occurring in the inner magnetosphere, including wave propagation (see Miyoshi et al. 2022 for a review). Matsuda et al. (2021) used observations of the same EMIC waves observed at Arase, the Van Allen Probes, and several ground stations to verify their theoretical growth, waveguiding by density irregularities in the magnetosphere, and their effect on subsequent ion heating. Miyoshi et al. (2019) combined both missions to discover a new source of plasmaspheric EMIC waves that result from the mode conversion of equatorial noise emissions at $L < 2$ at the cyclotron frequency of deuteron and alpha particles.

Colpitts et al. (2020) combined both missions to show the first direct observations of how rising tone chorus elements propagate from their equatorial source region to higher latitudes. The rising tone elements, observed first on Van Allen Probe A at 11 deg magnetic latitude, as shown in Fig. 22, became more oblique and were significantly attenuated as they propagated to the location of Arase at 21 deg magnetic latitude. A comparison with a ray-tracing analysis indicated that the rising tone elements were generated nearly parallel to the ambient magnetic field at or near the magnetic equator, and then propagated unducted first to the Van Allen Probes and then on to Arase with the observed time delay, wave normal angle and attenuation.

3.5 Summary

EFW collaborations with BARREL, FIREBIRD, Aerocube6, WWLLN, Arase, and others have resulted in numerous publications significantly advancing our understanding of the spatial and temporal variability of important magnetospheric processes. The resulting datasets of spatially separated, high time resolution data during dynamic times that will remain useful long into the future. These can be found at the following locations: FIREBIRD: http://solar.physics.montana.edu/FIREBIRD_II/, BARREL: http://barreldata.ucsc.edu/data_products/ (also at <http://cdaweb.gsfc.nasa.gov/>), Aerocube6: <https://rbspgway.jhuapl.edu/ac6> (registration required), WWLLN: <http://wwlln.net> (contact information only), Arase: <https://ergsc.isee.nagoya-u.ac.jp/index.shtml.en> (also at <http://cdaweb.gsfc.nasa.gov/>).

4 EFW Measurements, Data Quantities, Error Sources and Software

This section introduces the measurement of electric fields using the double probe technique, specific measurements and data products provided by EFW, and possible sources of error. Some data products include magnetic field data quantities obtained via shared channels with EMFISIS (Kletzing et al. 2013; Kletzing et al. this journal). Detailed discussions of the design and operation of the EFW instrument, as well as current biasing, effective boom length and spacecraft charging, are presented in Wygant et al. (2013).

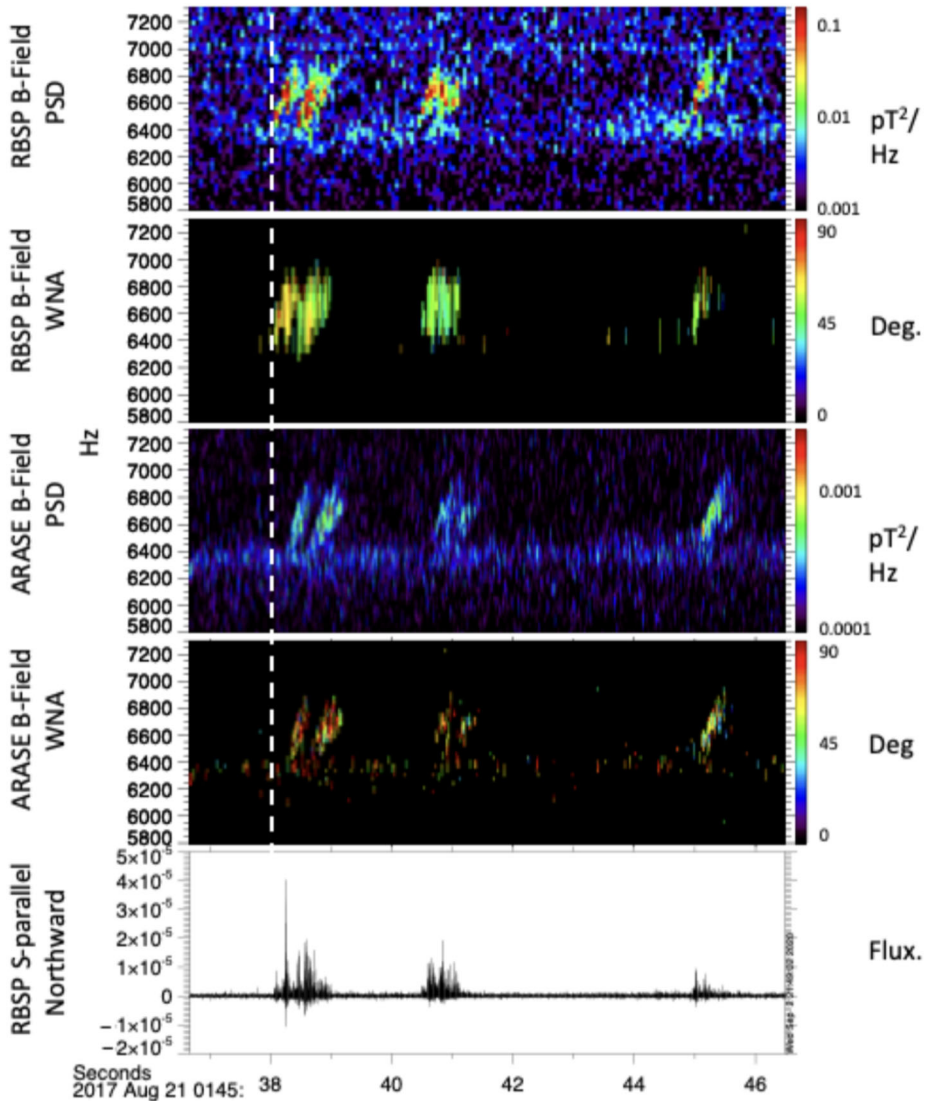


Fig. 22 (Adapted from Colpitts et al. 2020) Burst magnetic field spectrogram (a) and wave normal angle (b) from EFW (via shared analog channel with EMFISIS) on Van Allen Probe A at 11 deg magnetic latitude. (c) and (d) show the same on Arase at 21 deg magnetic latitude. (e) shows the parallel Poynting flux (positive is northward propagating) of the waves on Van Allen Probes A

4.1 Measurement of Electric Fields and Spacecraft Potential Using Double Probes

The double probe (sensor) technique for measurement of electric fields has been utilized on spacecraft for more than 50 years, and the basics are described in pedagogical articles by Fahleson (1967) and Mozer et al. (1973). The component of the electric field in the spacecraft frame along the direction connecting the two sensors is their potential difference divided by their separation. The double probe technique and mitigation of possible error

sources depends on understanding the current balance to a sensor immersed in a plasma. The basics of current balance are introduced in Fahleson (1967) and Mozer et al. (1973), and comprehensive discussions of sensor current biasing are described in Mozer (2016), Lindqvist et al. (2016), and references therein. Thorough descriptions of the double probe instruments on specific satellites are provided by Mozer et al. (1978a, 1979), Pedersen et al. (1984), Wygant et al. (1992), Marklund et al. (1994), Harvey et al. (1995), Gustafsson et al. (1997), Ergun et al. (2001), Marklund et al. (2004), Bonnell et al. (2008), Wygant et al. (2013), Torbert et al. (2016), and Lindqvist et al. (2016).

4.1.1 EFW Electric Field Measurements

EFW makes a measurement of the full three-dimensional electric field with two orthogonal sensor pairs in the spin plane, and one pair along the spin axis. In the spacecraft frame, the electric field along each sensor pair is given by their potential difference divided by physical separation, L_{sep} . Each sensor potential (V_i , $i = 1, 2, \dots, 6$) is measured as $V_i = V_{\text{pi}} - V_{\text{sc}}$, where V_{pi} and V_{sc} are the floating potentials of the sensor and spacecraft, respectively. Note that these floating potentials, defined relative to the local plasma, are not measured. Electric fields determined in this manner are typically smaller than the actual electric field because of distortion of the potential contours that occurs in the presence of the charged spacecraft surfaces including the spacecraft body, wire booms, etc. This is often accounted for by using an effective sensor separation that is different from the physical sensor separation. Measured electric fields consist of physical electric fields in an inertial frame, and electric fields due to the velocity of the spacecraft relative to that frame ($\mathbf{E}_{\text{mot}} = -\mathbf{v}_{\text{sc}} \times \mathbf{B}$, where \mathbf{B} is the magnetic field). \mathbf{E}_{mot} is typically subtracted off to obtain the physical electric field.

Possible sources of error in measurements of the electric field and approaches to mitigating their effects have been discussed in Bonnell et al. (2008), Wygant et al. (2013), and Mozer (2016). The orientation of the spin axis on both Van Allen Probes (within 15 deg of sun pointing) allows all four spin-plane sensors to be uniformly illuminated over a full spin period. This removes errors associated with differences in photoemission between the different sensors. Errors associated with photoemission asymmetries produced by the spacecraft body, primarily in the spacecraft/sun direction, can still remain. These are, however, reduced because the sensors sample electric fields in the plane orthogonal to the spacecraft/sun direction. Design features such as current biasing of sensors and voltage biasing of elements near the sensors further reduced measurement errors. Current biasing of the sensors in a low-density plasma provides a stable reference for the electric field measurement, improving accuracy by several orders of magnitude. The bias current and photoemission current are independent of the electron density and temperature of the ambient plasma. The implementation of these features in EFW is described in detail in Wygant et al. (2013).

On a spinning spacecraft like the Van Allen Probes, quasi-static electric field measurements in the spin plane are of higher quality than along the spin axis for several reasons. First, the larger sensor separation (100 m vs 15 m tip-to-tip for EFW) yields a larger potential difference between sensors for a given electric field. Second, the spin plane sensors are much farther from the charged spacecraft body and are thus more electrically isolated. Third, by fitting the data over three successive spin periods and computing a running average, the DC offsets produced by common mode error fields can be determined and removed. Fourth, for certain orientations the anti-sunward spin axis sensor potential (V_5) contains spikes due to the shadowing of the spin plane sensors and the magnetometer booms.

Effective Boom Length As discussed above, the magnitude of each electric field component depends on the separation of the two opposing sensors. Because of strong coupling with the plasma, the *effective boom length* (L_{eff}) is typically less than the physical length (L_{sep}) due to shorting associated with deformation of equipotential contours of the ambient electric field from the conducting spacecraft, conducting boom surfaces, and other effects (Mozer et al. 1978a). This length reduction was successfully modeled prior to the launch of the first current biased double probe instruments (Mozer et al. 1973; Pedersen et al. 1998; Ergun et al. 2016). These analyses show that the effective boom length is controlled by the ratio of the Debye length to the physical boom length. Followup estimates and comparisons to data have been made for a number of spacecraft including ISEE-1 (Mozer et al. 1978a, 1978b), THEMIS (Califf et al. 2016b), Cluster (Eriksson et al. 2006), and Van Allen Probes (Hartley et al. 2016, 2017; Lejosne and Mozer 2019). Within the plasmasphere, where the Debye length is small, L_{eff} is very close to L_{sep} . In the near-Earth plasma sheet and other regions, where the Debye length is large compared to the boom length, L_{sep} is larger than L_{eff} , typically by ~ 1.2 times. The physical boom length is used for the calculated EFW electric fields as presented in the Level 2 and Level 3 data. For precise estimates of the electric fields in low-density plasmas, such as the plasma sheet, users should scale the spin plane electric field values up by a factor of 1.2.

Frequency Response of the Electric Field Measurement In addition to the changes in the effective boom length discussed above, the frequency response of the instrument must be included for an accurate determination of the electric field waveform. The two primary effects are 1) the frequency response, including phase shifts, of the sheath-sensor voltage divider network (associated with the plasma sheath impedance and the input impedance of the input stages of the sensor preamplifier) and 2) any downstream anti-aliasing filters which are present in the digital filter boards of the EFW instrument (cf. Wygant et al. 2013 for details). Note that at the highest frequencies of 400 kHz, the booms (50 m spin plane and 7 m spin axis) have a distributed impedance that dominates and attenuates the frequency response. This is far above the EFW measurement range (16,384 S/sec) but does affect high frequency EMFISIS wave measurements.

The transition from resistive coupling (which occurs at the lowest frequencies) to capacitive coupling in the sheath-sensor voltage divider occurs at about 100 Hz and results in an associated phase shift and attenuation of the sensor signal by a factor of ~ 5 . Subsequent digital signal processing uses Bessel filters, which have a characteristic constant phase shift versus frequency which results in a frequency-independent time lag in the waveform. Values are presented in Table 3 of Wygant et al. (2013) for each sampling rate. These time delays were compensated for in all processing at L1 and higher. Following these time and frequency/phase response corrections, time tags for each data point in all variables in L2 and L3 files were centered on the sampling interval. A detailed discussion of the frequency response of the Van Allen Probe EFW instrument along with laboratory-calibrated frequency response curves and phase shifts due to the above effects may be found in Wygant et al. (2013).

Hartley et al. (2016, 2017, 2022) compared in situ measurements of the E/B ratio for whistler mode waves using EMFISIS data to that expected from the theoretical cold plasma dispersion relation using measured magnetic field and plasma densities and was able to provide one of the most rigorous experimental calibrations thus far of the high frequency attenuation of the wave electric field due to the sheath-sensor voltage response. Their analysis also provides a useful correction to the spin axis sensor measurements.

4.1.2 Spacecraft Potential

The spacecraft potential (V_{sc}), which is the potential of the spacecraft relative to the local plasma, can be approximated utilizing the measurements of the individual sensor potentials, $V_i = V_{pi} - V_{sc}$. Due to current biasing, the floating potential V_{pi} contributes only a constant offset on the order of 1 volt. Therefore, the spacecraft potential, as expressed, for example, using V_1 and V_2 is $V_{sc} = -(V_1 + V_2)/2 + (V_{p1} + V_{p2})/2$, but can be approximated as $-(V_1 + V_2)/2$. This sum also removes the contribution of any differential signal due to electric fields. As discussed in many previous references (e.g., Pedersen et al. 1995, 2008), the spacecraft potential can often provide an estimate of the plasma density. In the case of the Van Allen Probes, reliable values were obtained over a range of $\sim 10 \text{ cm}^{-3}$ to $\sim 3000 \text{ cm}^{-3}$ for low temperature plasmas characteristic of the plasmasphere after calibration against the more precise measurement based on visual identification of the upper hybrid line from the EMFISIS instrument (Kurth et al. 2015). This calibration was typically based on ~ 8 orbits of data and updated monthly over the course of the mission. For comparison, the upper hybrid line determination is accurate to ~ 10 percent but has a typical 6.5 sec resolution (0.5 sec resolution for selected time intervals) and is available only when a clear upper hybrid line is observed, while the spacecraft potential estimate of density is accurate to about 30% but has a time resolution of 32 S/sec, and is appropriate for high time resolution wave studies. See Jahn et al. (2020) for a detailed comparison of these two density measurements on the Van Allen Probes. Note that care should be taken when using spacecraft potential for density estimates in the presence of extremely large amplitude plasma waves (e.g., tens of mV/m), which can themselves modify spacecraft potential as shown by Malaspina et al. (2014a) and Wang et al. (2014).

4.2 EFW Data Products

EFW provides a variety of publicly available data products including electric fields, individual sensor potentials, spacecraft potential, and density estimated from spacecraft potential. The data products are provided in Common Data Format (CDF) files and include waveforms, spectra, and filter bank products with cadences ranging from spin period (~ 11 sec) to burst rates up to 16,384 S/sec. In this section we discuss each data product, error codes and briefly describe error sources.

4.2.1 MGSE Coordinate System

As discussed previously, the spin plane measurement of the quasi-static electric field is significantly more accurate than the spin axis measurement. It is therefore important to separate the spin plane and spin axis components when rotating electric field vector data from spinning (antenna) coordinates to a despin coordinate system. For this reason, many of the EFW science quantities are provided in the modified GSE (mGSE) coordinate system, which is defined in terms of GSE as follows:

- 1) $\mathbf{X}_{mgse} = \mathbf{S}_{gse}$, where \mathbf{S}_{gse} is the unit vector along the spin axis in the direction of the sun in GSE coordinates (provided in the EFW L2 and L3 data, cf. Table 1)
- 2) $\mathbf{Y}_{mgse} = -(\mathbf{S}_{gse} \times \mathbf{Z}_{gse})$
- 3) $\mathbf{Z}_{mgse} = (\mathbf{S}_{gse} \times \mathbf{Y}_{mgse})$

The mGSE system is identical to GSE for a spin axis that points directly at the sun. For both Van Allen Probes the spin axis was maintained between 15–27 deg of sun-pointing (Kirby

Table 1 EFW Boom locations and telemetry channels and their relation to two spacecraft coordinate systems

EMFISIS science coordinates (SCM& FGM)	S/C coordinates	EFW TM channel
+V	+X + Y	4
+U	+X - Y	2
-U	-X + Y	1
-V	-X - Y	3
+W	+Z	6
-W	-Z	5

et al. 2013), and so mGSE and GSE were often qualitatively similar. The \mathbf{Y}_{mgse} coordinate is in the ecliptic plane and also in the spin plane of the long rotating booms. Thus, the \mathbf{Y}_{mgse} and \mathbf{Z}_{mgse} components of the electric field are measured relatively accurately by the long spin axis boom system while the \mathbf{X}_{mgse} component is measured less accurately by the shorter spin axis booms. An important feature of the mGSE system is that the \mathbf{Y}_{mgse} component of the electric field lies within 15 deg of the dawn-dusk electric field (\mathbf{Y}_{gse}) and is well-determined by the long spin axis booms. Generally, only the spin plane measurements are accurate enough at low frequencies to measure the large scale quasi-static electric field, while the spin axis measurement is useful for wave electric fields (> 10 Hz). This means that, to rotate DC electric field vectors to a more standard coordinate system such as GSE, an estimate of E_x must be made. In the quasi-static regime this can be done using the ideal MHD assumption that there is no electric field along the background magnetic field, or $\mathbf{E} * \mathbf{B} = 0$, which yields $E_x = -(E_y B_y / B_x + E_z B_z / B_x)$. However, any errors in E_y and E_z may be significantly amplified if B_x is small relative to B_y or B_z , and the method is generally only reliable when the angle between the spin plane and magnetic field is > 15 deg.

It is also useful to understand the relationship between the spacecraft coordinate system, and the instrument coordinate systems for electric field measurements, and for fluxgate and search coil magnetometer measurements. To facilitate identification of waves, the three search coil sensors and the three pairs of electric field sensors are aligned. Figure 23 and Table 1 show the relationship between electric field sensor locations, labeled in the fourth column by sensor number ($V_1, V_2, V_3, V_4, V_5, V_6$), the spacecraft coordinate system which can be used to determine the field-of-view of the particle instruments on the spacecraft, and magnetic field coordinate system (u, v, w) used by EMFISIS for the fluxgate and search coil magnetometer sensors.

4.2.2 Spin-Fit Electric Field

The primary EFW data product is the spin plane electric field at spin period cadence (~ 11 sec) in the mGSE coordinate system. This is recommended for users who do not require the full cadence (16 or 32 S/sec) data, which are described in Sect. 4.2.3. The spin fitting procedure is a least-squares fit for each spin period of one component of the onboard-determined 32 S/sec spin plane electric field (E_{12} or E_{34}) to determine the part of the signal that varies as a sine wave with the spin period. Iterative outlier subtraction was used for points more than 1.4 standard deviations from the mean. Any DC offsets, which represent variations in sensor potentials that can be caused by different sensor work functions, spurious currents, etc. (see Wygant et al. 2013; Mozer 2016), were then removed. Failed spin fits occurred when fewer than five data points remained following the iterative outlier subtraction, and these times were not included in the final spin fit data products (Table 4). Extensive

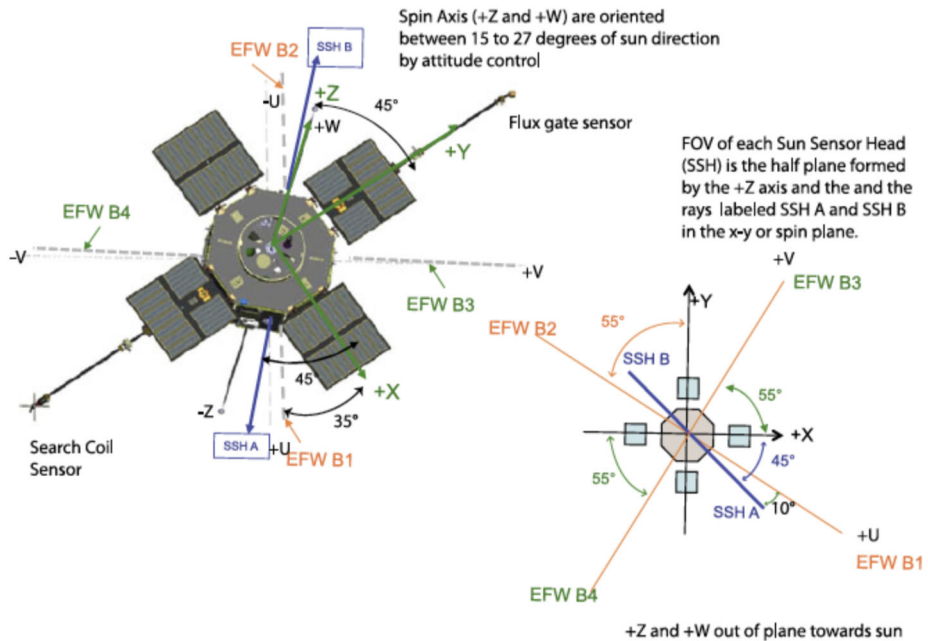


Fig. 23 (Adapted from Wygant et al. 2013) The orientation of the EFW spin plane boom sensors (u, v, w coordinates) on the Van Allen Probes spacecraft

testing indicated that spin fits derived from E_{12} and E_{34} on both Van Allen Probe A and B were very similar during times when all four spin plane probes were healthy. For the public EFW data products, spin-fit electric fields from Van Allen Probe B were derived from the onboard-determined 32 S/sec electric field values E_{12} for the full mission. For Van Allen Probe A, E_{12} was used until 2014-12-31. After this date, however, V_1 sensor photoemission decreased significantly, leading to a decrease in performance. The team were able to use linear combinations of the working sensor potentials to provide a measurement of the two-dimensional electric field in the spin plane at 16 S/sec. The best results were obtained using a V_{24} potential difference starting January 1, 2015. These are available in the L3 spin fit files for Probe A.

4.2.3 Survey DC Electric Fields, Sensor Potentials, and Densities

For users requiring data with higher time resolution than the spin period, EFW provides survey cadence waveform products. These include the aforementioned low frequency (32 S/sec, DC-coupled) *spin plane* electric fields from the on-board differenced spin plane electric fields E_{12} and E_{34} , and 16 S/sec potentials from the spin plane sensors (V_{1-4}). Note that the spin plane electric field on Van Allen Probe A starting from January 1, 2015 should be used with caution, due to the V_1 degradation as mentioned in Sect. 4.2.2.

Electric fields and potentials from the short spin axis sensors (V_5 , V_6) are primarily used for AC analysis because of the lower accuracy at DC. Note that for some orientations the anti-sunward spin axis probe (V_5) was shadowed by the spin plane booms and/or the magnetometer booms, producing spikes in the sensor potential.

EFW also provides a high cadence (16 S/s) plasma density calculated from the same spin plane probe pair used in production of the spin-fit electric fields. Monthly calibration

Table 2 Frequency range (Hz) for each filter bank channel for 7-channel mode (blue) and 13-channel mode (all). The numbers in the rightmost column are the frequencies of the peak of the channel response curves

Van Allen Probes EFW Filter Bank Channels		
ID	Freq range & peak (Hz)	
1	0.8–1.5	1.36
2	1.5–3	2.62
3	3–6	5.14
4	6–12	10
5	12–25	20.8
6	25–50	40.6
7	50–100	83.8
8	100–200	172
9	200–400	334
10	400–800	1360
11	800–1600	1360
12	1600–3200	2800
13	3200–6500	–6500

against the upper hybrid line identified from EMFISIS High Frequency Receiver (HFR) spectral data (Kurth et al. 2015) was performed, so this data product provides accurate density measurements in the range from $\sim 10 \text{ cm}^{-3}$ to $\sim 3000 \text{ cm}^{-3}$. Comparison between the EMFISIS and EFW densities is described in detail in Jahn et al. (2020).

4.2.4 Spectral Data

EFW telemetered AC-coupled survey spectral (complex Fast Fourier Transform) data at a 4 sec cadence in 64 pseudo-log frequency bins from 1 Hz to 6.5 kHz. For each 4 sec bin only the first one second was used in the FFT. Spectral products were produced throughout the mission from potentials V_1 , V_2 , potential differences V_{12} , V_{56} , and search coil magnetic channels (from EMFISIS) $SCM_{u,v,w}$, where u , v , w are the search coil directions in the spinning spacecraft frame (see Fig. 24).

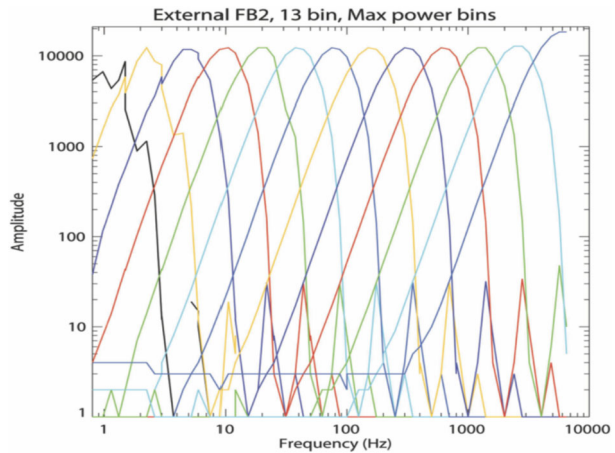
4.2.5 Peak Detector (Bandpass Filter Bank) Data

The EFW bandpass filter peak detector continuously recorded the peak and average DC-coupled electric and/or magnetic wave amplitude of 16,384 S/sec data at eight times per second, providing data at a higher time resolution but lower frequency resolution than the spectral data. This cadence is typically sufficient to allow accurate count of waveform modulation peaks in VLF waves such as chorus (Tyler et al. 2019a,b). The peak detector mode of operation was changed multiple times over the mission lifetime to provide data necessary for specific science topics. These modes are presented in Table 2 and include either 7 or 13 frequency bins from ~ 0.8 –6500 Hz, and either electric field only, or simultaneous electric and magnetic fields. Due to design limitations, every other frequency bin was skipped in the 7-channel mode. We note that, under the assumption of narrowband waves, the overlapping gain curves (Fig. 24) can be used to significantly improve the frequency and amplitude resolution of the filter bank data, as described in detail by Tyler et al. (2019b).

4.2.6 Burst Data Products

One of the important features of EFW was its burst waveform collection capabilities. This included a large (32 GB) onboard DC-coupled flash memory (*burst 1*) for ground-selected

Fig. 24 Response curves (amplitude vs frequency) for the 13 filter bank bins. These were used by Tyler et al. (2019b) to enhance the frequency and amplitude resolution of filter bank data under the assumption of narrowband waves



collection and playback of waveforms at rates from 128 to 16,384 S/sec, and a more traditional style AC-coupled interferometric mode (*burst 2*) consisting of onboard-triggered five second samples of 16,384 S/sec waveforms into a 256 MB memory. The burst 1 memory represented an orders-of-magnitude increase in highly flexible collection capability compared to previous satellite burst memories. Continuous 3d electric and magnetic field waveforms could be obtained for hours or even days depending on the collection rate, fundamentally changing the way in which burst collection could be obtained to address science goals. This capability was vital for the collaborative campaigns with other missions as described in Sect. 3.

Both burst 1 and burst 2 memories telemetered single-ended potentials $V_{[1,2,3,4,5,6]}$ and search coil magnetic fields in UVW coordinates. Onboard-produced electric fields $E_{[12,34,56]}$ were telemetered early in the mission, but because these could be reproduced on the ground from the single-ended potentials with nearly the same accuracy, EFW stopped transmitting them in late 2013 to reallocate telemetry (see Table 4).

Unlike the filter bank data, the source channels for EFW burst data remained the same throughout the entire mission. Data collection rate for burst 1 was, however, often changed to suit the desired collection scheme. Table 3 shows the various rates used, the number of hours (memory capacity) at each rate, and the amount of playback that was possible per day (green). The values in blue indicate the final totals (hrs and samples) of playback for the entire mission. Of note, over 2500 hrs of burst 1 playback were obtained by mission end on each spacecraft. This vastly exceeds the totals for any previous magnetospheric mission.

Because the burst data products are, by definition, not a full duty cycle, their distribution with L and MLT is not the same as the spacecraft orbital sampling. The L vs MLT dial plots in Fig. 25 show the physical distribution of burst 1 data for the different sample rates. Overall, the collection is focused near apogee ($L > \sim 4$), and with a sample rate that largely depended on local time of apogee, which drifted over the course of the mission. For example, higher sample rates were typically selected for apogee collection on the dayside for capture of chorus waves, while lower sample rates could be used in the afternoon/night sector for capture of EMIC and other low frequency waves.

4.3 EFW Data Product Variables, Files, and Software

This section contains a detailed description of the names of the primary EFW measurement variables and the EFW data file in which they reside (in the form of ISTP-compliant CDF

Table 3 EFW burst 1 capabilities. The green values show all the possible collection rates that were used during the mission, each corresponding to a maximum number of hours of continuous data collection, and a set number of hours of playback per day. For each Probe and mode, the blue values show the total telemetered data volume (hrs) over the entire mission, and the total number of burst data samples ($\times 10^9$). The mission totals are shown in red

(A) Collection rate (S/sec)	(B) Temporal memory size	(C) Playback rate (hrs/day)	Total telemetered burst data over entire mission			
			Probes A & B (hrs)		Probes A & B (Samples 10^9)	
512	24d 8hr	8	1415	1025	2.61	1.89
1,024	12d 4hr	4	180	507	0.67	1.87
2,048	145.6hr	2	48	44	0.36	0.33
4,096	72.8hr	1	326	568	4.82	8.38
8,192	36.4hr	0.5	34	20	1.02	0.62
16,384	18.2hr	0.25	621	509	36.67	30.06
Total			2627	2675	46.13	43.14

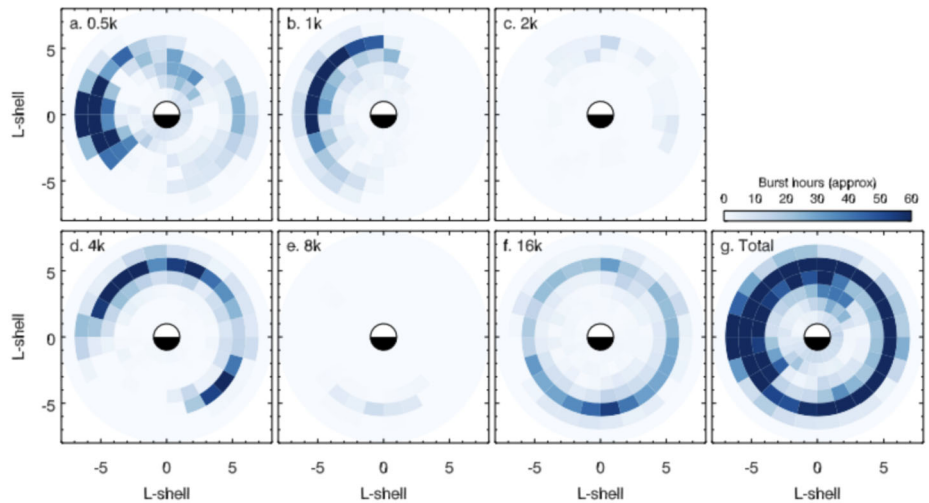


Fig. 25 Distributions of EFW burst 1 data (hours) over the entire in L and MLT for the different collection rates used. The rightmost panel shows the totals over all collection rates. Higher/lower rate collection was focused on the morning/afternoon sectors in order to capture chorus/EMIC waves

files). The variables include data derived from the EFW instrument, from the channels shared with EMFISIS, and ephemeris variables. The content of EFW data files is summarized in Table 4. Data are archived at CDAWeb (<https://cdaweb.gsfc.nasa.gov/pub/data/rbsp/>). In addition, daily summary “quick look” plots are available at <http://rbsp.space.umn.edu/survey>, while the EFW website is available at <http://rbsp.space.umn.edu>. Please note that this website contains a “required reading” section that describes in more detail the basics of using EFW data. Some users may require data beyond what is offered in the archived EFW CDF files, such as additional housekeeping variables, spin-fit electric fields with different probe pairs, etc. These users are encouraged to contact the EFW team.

4.3.1 EFW L2 and L3 Variables

As discussed previously, the measured electric field $\mathbf{E}_{\text{measured}}$ consists of geophysically interesting fields as well as the *motional* electric field \mathbf{E}_{mot} caused by the relative motion of the sensors with respect to the Earth's magnetic field. The geophysically uninteresting motional electric field ($\mathbf{E}_{\text{mot}} = -\mathbf{v}_{\text{sc}} \times \mathbf{B}_0 > 200$ mV/m) dominates near perigee due to the large spacecraft velocity ($|\mathbf{v}_{\text{sc}}| \sim 8$ km/s in the Earth-centered inertial frame) and strong magnetic field \mathbf{B}_0 . Removal of this field gives the electric field in an inertial frame of reference. Note that complete removal of this field near perigee is very difficult, particularly at $L < 3$ (see Lejosne and Mozer 2016a, 2016b, 2018, 2019, 2020; Lejosne et al. 2021).

Electric field variables in the inertial frame include:

efield_in_inertial_frame_spin-fit_mgse (size of $[n, 3]$; located in L3 files) – The spin-fit electric field at spin period cadence (~ 11 sec) with the spin axis component set to 0. The probe pair used for the spin-fit can be found in the *used_boom_pair* variable.

efield_in_inertial_frame_spin-fit_edotb_mgse (size of $[n, 3]$; located in L3 files) – The spin-fit electric field similar to *efield_in_inertial_frame_spin-fit_mgse* but with the addition of the spin axis E field calculated from the $\mathbf{E} * \mathbf{B} = 0$ assumption.

The motional electric field in the spacecraft frame (\mathbf{E}_{mot}) is included as:

VxB_mgse (size of $[n, 3]$; located in L2 spin-fit files) – The motional electric field (\mathbf{E}_{mot}) in mGSE coordinates.

Near perigee, the inertial frame electric field is dominated by the electric field that drives the co-rotation of the plasma about the Earth ($\mathbf{E}_{\text{corot}} = (\boldsymbol{\omega} \times \mathbf{R}) \times \mathbf{B}_0$, where the co-rotational velocity $\mathbf{v}_{\text{corot}} = \boldsymbol{\omega} \times \mathbf{R}$ is on the order of 0.6 km/s).

In order to better observe plasma frame electric fields at low L, including those associated with deviations from corotation, the following equivalent (to the inertial frame) products are available with $\mathbf{E}_{\text{corot}}$ subtracted off.

The electric field variables in the corotation frame include:

efield_in_corotation_frame_spin-fit_mgse (size of $[n, 3]$; located in L3 files) – The spin-fit electric field similar to *efield_in_inertial_frame_spin-fit_mgse* but with $\mathbf{E}_{\text{corot}}$ subtracted off. The spin axis E field is 0. The optimum probe pair used for spin-fit can be found in the *used_boom_pair* variable.

efield_in_corotation_frame_spin-fit_edotb_mgse (size of $[n, 3]$; located in L3 files) – The spin-fit electric field similar to *efield_in_corotation_frame_spin-fit_mgse* but with the addition of the spin axis electric field calculated from the $\mathbf{E} * \mathbf{B} = 0$ assumption.

efield_spin-fit_mgse (size of $[n, 3]$; located in L2 spin-fit files) – The same spin-fit electric field as *efield_in_corotation_frame_spin-fit_mgse*.

VxB_efield_of_earth_mgse (size of $[n, 3]$; located in L3 files) – The corotation electric field ($\mathbf{E}_{\text{corot}}$) in mGSE coordinates.

efield_coro_mgse (size of $[n, 3]$; located in L2 spin-fit files) – The corotation electric field ($\mathbf{E}_{\text{corot}}$) in mGSE coordinates. This is the same as *VxB_efield_of_earth_mgse*.

In addition to electric fields, EFW also provides measurements of single-ended probe potentials. These are generally provided at a survey cadence of 32 or 16 S/sec and include:

vsvy (size of $[n, 6]$; located in L1 and L2 *vsvy* files) – The single-ended probe potentials from the 4 spin plane probes (V_{1-4}) and two spin axis probes (V_5 and V_6). The *vsvy* data in the L1 files are in ADC units whereas *vsvy* data in the L2 files are in volts and have been processed to remove any time tag irregularities that occasionally exist in the L1 data.

vsvy_vavg (size of $[n, 3]$; located in L2 vsvy files) – The spacecraft potential in volts, defined as the average of opposing probe potentials. The 3 components are the average values from V_{12} , V_{34} , and V_{56} .

spacecraft_potential (size of $[n]$; located in L3 files) – The spacecraft potential in volts. The optimum sensor pair used for this calculation can be found in the *used_boom_pair* variable.

EFW-derived plasma density is provided in:

density (size of $[n]$; located in L3 files) – The density estimation derived from the spacecraft potential. See Sect. 4.2.3 for details.

EFW CDF files contain several data flags in order to indicate times where caution is advised, or when data are deemed unusable. These include:

efw_qual (size of $[n, 20]$; located in L2 files) – This variable contains 20 commonly used EFW flag values. Definitions of the 20 flags are described in Table 5 and archived at <https://spdf.gsfc.nasa.gov/pub/data/rbsp/documents/efw/>.

flags_all (size of $[n, 25]$; located in L2 and L3 files) – This variable contains 25 commonly used EFW flag values. For backward compatibility, although more flags are included in the L3 files, we kept *efw_qual* in the L2 files. The added flags do not affect the global flag, i.e., the L2 and L3 global flags are the same. Definitions of the 25 flags are described in Table 5 and archived at <https://spdf.gsfc.nasa.gov/pub/data/rbsp/documents/efw/>.

Ephemeris variables are included in most EFW CDF files. These are derived by the EFW team from SPICE kernels and include:

velocity_gse (size of $[n, 3]$; located in L3 files) – The spacecraft velocity (km/s) in GSE coordinates.

position_gse (size of $[n, 3]$; located in L3 files) – The spacecraft position (km) in GSE coordinates.

vel_gse (size of $[n, 3]$; located in L2 files) – Same data as *velocity_gse* but kept for backward compatibility.

pos_gse (size of $[n, 3]$; located in L2 files) – Same data as *position_gse* but kept for backward compatibility.

spinaxis_gse (size of $[n, 3]$; located in L2 and L3 files) – The unit vector of the spacecraft spin axis in GSE coordinates.

mlt (size of $[n]$; located in L2 and L3 files) – The magnetic local time (MLT) in hours.

lshell (size of $[n]$; located in L2 and L3 files) – The dipole Lshell.

mlat (size of $[n]$; located in L2 and L3 files) – The magnetic latitude in degrees.

orbit_num (size of $[n]$; located in L2 and L3 files) – The orbit number defined using the spacecraft position. The orbit number increases when the spacecraft passes the perigee.

bias_current (size of $[n, 6]$; located in L2 and L3 files) – The bias current applied to each probe.

Now that we have discussed the general variable types, Sect. 4.3.2 lists the exact variables found in each EFW CDF file, and Sect. 4.3.3 is a detailed discussion of available flag variables.

4.3.2 EFW CDF Files

The EFW data production chain that produced the final publicly available data files consisted of four steps of calibration, or “Levels”, from internal Level 0 and Level 1 files to

publicly available Level 2 and Level 3. Level 0 data contain raw (uncalibrated, binary) data. These were time-tagged to produce uncalibrated waveform and spectral Level 1 data in the spinning spacecraft frame. In general, Level 1 data are not suitable for scientific analysis or publication and require further processing. Level 1 data products were then calibrated to physical units and rotated into despun spacecraft (DSC) or modified GSE (mGSE) coordinates to produce Level 2 data, which include both full time resolution and spin period products. The exception is the burst waveform data which are provided to the public at Level 1. Level 2 data can be used for scientific analysis including the investigation of asymmetric phenomena around the spacecraft such as photoelectron clouds and wakes, but the flagging of poor-quality data is less stringent than that used for Level 3 data. Level 3 files contain EFW's best calibrated products but are available at spin period resolution only (due to the requirement of the spin fitting procedure). The team strongly encourages the use of Level 3 products when data at higher time resolution are not required.

Table 4 provides a summary of all variables included in each CDF file, as well as the start and stop dates when each was produced.

4.3.3 Error Sources and Data Quality Flags

As discussed previously, EFW actively biased its sensors to significantly reduce the sheath impedance, allowing a more stable sensor operation and the measurement of high-quality electric fields. However, there remain times when the measurement accuracy of the quasi-static electric field decreases, most often in the resistively coupled regime of $\sim < 100$ Hz. For example, excessive spacecraft charging caused by enhanced fluxes of energetic electrons may make quasi-static data unreliable. Therefore, EFW provides flags allowing the user to ascertain data quality. To specify the quality of the DC electric field data and associated error sources, EFW defines 25 flag quantities in the L3 CDF files. The key information about the flags is summarized in Table 5. End users should refer to the meaning of these flags when there is a need for analyzing the flagged DC-coupled electric field data. A detailed description of each flag is documented at <https://spdf.gsfc.nasa.gov/pub/data/rbsp/documents/efw/>. As a cautionary note, not all types of data quality issues are easily captured in the 25 flags, and users are encouraged to exercise care when analyzing EFW data. A non-comprehensive list of time periods with possible data quality issues can be found at the same link.

Global Flag The global flag (*global_flag*) is a general data quality indicator for DC electric field data. It is an amalgamation of flags that strongly suggests data of bad or significantly reduced quality that should NOT be used. Specifically, the global flag is triggered by any of the following conditions: excessive sensor charging (*v[1-6]_saturation*, *charging*, *charging_extreme*, *eclipse*, and *boomflag[1-4]*), sensor diagnostic tests (*efw_sweep*), attitude changes (*maneuver*), and antenna deployments (*efw_deploy*). The relevant flags, as noted in the parenthesis, are discussed in detail below. Globally flagged data are removed in EFW L3 files but remain in the L2 files. Note that it is often the case that AC-coupled EFW data beyond a few hundred Hz, which reside in the L2 filter bank and spectral files, are usable when the global flag is triggered.

Flag Related to Sensor Diagnostic Tests As discussed previously, accurate measurements of electric fields in low-density plasmas require active biasing in order to control probe photoemission and limit excessive probe charging relative to the plasma. On EFW, photoemission is controlled by current biasing the sensors and voltage biasing the usher and guard surfaces (Wygant et al. 2013). The ideal bias currents and voltages changed over the course of the

Table 4 The EFW CDF data products (L1, L2, and L3). Primary variables are highlighted as red

File type	File naming convention	Cadence	Dates produced
L3	rbstp[a,b]_efw-l3_YYYYMMDD_v04.cdf Description: These files represent the best EFW data at spin period cadence, and are the ones that most users will want. The used probe pair is labeled in the variable used_boom_pair Variables: <code>efield_in_corotation_frame_spin_fit_mgse</code> , <code>efield_in_inertial_frame_spin_fit_mgse</code> , <code>efield_in_corotation_frame_spin_fit_edotb_mgse</code> , <code>efield_in_inertial_frame_spin_fit_edotb_mgse</code> , <code>VxB_efield_of_earth_mgse</code> , <code>spacecraft_potential</code> , <code>density</code> , <code>flags_all</code> , <code>velocity_gse</code> , <code>position_gse</code> , <code>mlt</code> , <code>lshell</code> , <code>spinaxis_gse</code> , <code>used_boom_pair</code> , <code>bias_current</code>	~ 11 sec	A: 2012-09-23 to 2019-02-23 B: 2012-09-23 to 2019-07-16
L2 spin-fit	rbstp[a,b]_efw-l2_e-spin-fit-mgse_YYYYMMDD_v04.cdf Description: Similar to L3 but with less strict calibrations and flagging. Variables: <code>efield_spin_fit_mgse</code> , <code>VxB_mgse</code> , <code>efield_coro_mgse</code> , <code>orbit_num</code> , <code>vel_gse</code> , <code>pos_gse</code> , <code>mlt</code> , <code>lshell</code> , <code>spinaxis_gse</code> , <code>flags_all</code> , <code>bias_current</code>	~ 11 sec	A: 2012-09-23 to 2019-02-23 B: 2012-09-23 to 2019-07-16
L2 electric fields in mGSE	rbstp[a,b]_efw-l2_esvy_despun_YYYYMMDD_v03.cdf Description: Electric field data in the mGSE coordinate Variables: <code>efield_mgse</code> , <code>orbit_num</code> , <code>vel_gse</code> , <code>pos_gse</code> , <code>mlt</code> , <code>lshell</code> , <code>spinaxis_gse</code> , <code>bias_current</code> , <code>efw_qual</code>	32 S/sec	A: 2012-09-23 to 2019-02-23 B: 2012-09-23 to 2019-07-16
L2 electric fields in UVW	rbstp[a,b]_efw-l2_e-hires-uvw_YYYYMMDD_v02.cdf Description: Electric field data in the UVW coordinate. Includes spin axis component Variables: <code>e_hires_uvw_raw</code> , <code>e_hires_uvw</code> , <code>L_vector</code> , <code>e_hires_uvw_efw_qual</code>	32 S/sec	A: 2012-09-23 to 2019-10-14 B: 2012-09-23 to 2019-07-16
L2 single ended potentials	rbstp[a,b]_efw-l2_vsyy-hires_YYYYMMDD_v02.cdf Description: Single-ended probe potential data Variables: <code>vsyy</code> , <code>vsyy_vavg</code> , <code>orbit_num</code> , <code>vel_gse</code> , <code>pos_gse</code> , <code>mlt</code> , <code>lshell</code>	16 S/sec	A: 2012-09-05 to 2019-10-14 B: 2012-09-13 to 2019-07-16
L2 spec	rbstp[a,b]_efw-l2_spec_YYYYMMDD_v02.cdf Description: Spectral product at 64 frequency bins, averaged over each 4 sec time period, with selectable quantities of E and B fields and potentials Variables: <code>spec64_e_l2ac</code> , <code>spec64_e56ac</code> , <code>spec64_v1ac</code> , <code>spec64_v2ac</code> , <code>spec64_scmu</code> , <code>spec64_scmw</code> , <code>spec64_fcenter</code> , <code>efw_qual</code>	4 sec	A: 2012-09-05 to 2019-10-12 B: 2012-09-05 to 2019-07-14

Table 4 (continued)

File type	File naming convention	Cadence	Dates produced
L2 filter bank	<p>rbstp[a,b]_efw-12_fbk_yyyyymmdd_v02.cdf</p> <p>Description: Fast filter bank data. There are several mode changes, including changes between 13 or 7 frequency bins [fbk13.fbk7; see Table 2], [e12.e34], and [scmu.scmw]. “pk” and “av” represent the peak and average value each eighth of a second.</p> <p>Variables: fbk13_e12dc_pk, fbk13_e12dc_av, fbk13_scmu_pk, fbk13_scmu_av</p>	8 S/sec	<p>A: 2012-09-05 to 2019-10-12</p> <p>B: 2012-09-05 to 2019-07-14</p>
L1 esvy	<p>rbstp[a,b]_ll_esvy_yyyyymmdd_v03.cdf</p> <p>Description: Level 1 data of the electric field</p> <p>Variables: esvy</p>	32 S/sec	<p>A: 2012-09-05 to 2019-10-14</p> <p>B: 2012-09-05 to 2019-07-16</p>
L1 vsvy	<p>rbstp[a,b]_ll_vsvy_yyyyymmdd_v03.cdf</p> <p>Description: Level 1 data of the single ended potential</p> <p>Variables: vsvy</p>	16 S/sec	<p>A: 2012-09-05 to 2019-10-14</p> <p>B: 2012-09-05 to 2019-07-16</p>
L1 EB1	<p>rbstp[a,b]_ll_eb1_yyyyymmdd_v02.cdf</p> <p>Description: Ground selectable burst data of the electric field</p> <p>Variables: E12, E34, E56</p>	512–16,384 S/sec	<p>A: 2012-09-05 to 2013-10-09</p> <p>B: 2012-09-06 to 2013-12-20</p>
L1 VB1	<p>rbstp[a,b]_ll_vb1_yyyyymmdd_v02.cdf</p> <p>Description: Ground selectable burst data of the single ended potential</p> <p>Variables: V1, V2, V3, V4, V5, V6</p>	512–16,384 S/sec	<p>A: 2012-09-05 to 2019-10-10</p> <p>B: 2012-09-06 to 2019-07-16</p>
L1 MSCB1	<p>rbstp[a,b]_ll_mscb1_yyyyymmdd_v02.cdf</p> <p>Description: Ground selectable burst data of the search coil magnetic field</p> <p>Variables: MSCx, MSCy, MSCz</p>	512–16,384 S/sec	<p>A: 2012-09-05 to 2019-10-10</p> <p>B: 2012-09-06 to 2019-07-16</p>

Table 4 (continued)

File type	File naming convention	Cadence	Dates produced
L1 VB1 split	rbsp[a,b]_efw_l1_vb1-split_YYYYMMDDThhmmss_v03.cdf Description: Single day of VB1 data split into smaller (15-min) files, because the VB1 files can be very large (> 5 GB). Variables: V ₁ , V ₂ , V ₃ , V ₄ , V ₅ , V ₆	512–16,384 S/sec	A: 2012-09-05 to 2019-10-10 B: 2012-09-06 to 2019-07-16
L1 MSCB1 split	rbsp[a,b]_efw_l1_mscb1-split_YYYYMMDD_hhmmss_v03.cdf Description: Single day of MSCB1 data split into smaller (15-min) files. Variables: MSC _X , MSC _Y , MSC _Z	512–16,384 S/sec	A: 2012-09-05 to 2019-10-10 B: 2012-09-06 to 2019-07-16
L1 EB2	rbsp[a,b]_l1_eb2_YYYYMMDD_v01.cdf Description: Onboard auto-triggered burst data of the electric field Variables: E ₁₂ , E ₃₄ , E ₅₆	16,384 S/sec	A: 2013-04-25 to 2019-10-14 B: 2013-04-25 to 2019-07-16
L1 VB2	rbsp[a,b]_l1_vb2_YYYYMMDD_v01.cdf Description: Onboard auto-triggered burst data of the single ended potential Variables: V ₁ , V ₂ , V ₃ , V ₄ , V ₅ , V ₆	16,384 S/sec	A: 2012-09-05 to 2019-10-14 B: 2012-09-05 to 2019-07-16
L1 MSCB2	rbsp[a,b]_l1_mscb2_YYYYMMDD_v01.cdf Description: Onboard auto-triggered burst data of the search coil magnetic field Variables: MSC _X , MSC _Y , MSC _Z	16,384 S/sec	A: 2012-09-05 to 2019-10-14 B: 2012-09-05 to 2019-07-16

Table 5 The 25 EFW flag values in the variable “flags_all” in the L3 data files

No	Flag name	Conditions for flag = 1, which marks questionable data
1	global_flag	When any of the following flags are thrown: v[1-4]_saturation, eclipse, maneuver, charging, charging_extreme, efw_deploy, efw_sweep, boomflag[1-4]
2	eclipse	When the spacecraft is in the shadow of the earth, including umbra and penumbra (padded by ± 10 min)
3	maneuver	Maneuvering and thrusting
4	efw_sweep	EFW sensor diagnostic tests (SDT), also known as the bias sweeps
5	efw_deploy	Boom deploy times early in the mission (2012)
6–11	v[1-6]_saturation	v1_saturation is 1 when the single-ended probe potential V1 > 195 volts (sensor relative to sc potential). v[2-6]_saturation are similarly defined for V2, V3, . . . , V6
12	Espb_magnitude	Not used
13	Eparallel_magnitude	Not used
14	sine_wave_fit_quality	The quality of the spin fit sine wave. Generally used to identify times when wake effects are occurring.
15	autobias	When the autobias algorithm is operating
16	charging	When $[L > 4 \text{ and } V_{sc} > 0 \text{ V}]$ or $[V_{sc} < -20 \text{ V for any L}]$, where V_{sc} is the spacecraft potential
17	charging_extreme	$[L > 4 \text{ and } V_{sc} > 20 \text{ V}]$ or $[V_{sc} < -20 \text{ V for any L}]$, where V_{sc} is the spacecraft potential
18	density	When global_flag = 1 and when density is < 10 or $> 3,000 \text{ cm}^{-3}$
19–24	boomflag[1-6]	boomflag1 is 1 when V1 deviates from the median of $[V1, V2, V3, V4]$ by $> 5 \text{ V}$. boomflag[2-4] are similarly defined for V2, V3, V4. boomflag[5-6] are not used
25	undefined	Not used

mission as the sensors aged and as the orbit precessed. Determining these ideal values therefore required EFW to perform occasional sensor diagnostic tests (SDTs, or “bias sweeps”) throughout the mission. During SDTs, which lasted a few to tens of minutes, the EFW instrument was stepped through a variety of preprogrammed current and voltage values. All SDT times are flagged with the *efw_sweep* flag and trigger the global flag.

Flags Related to Excessive Sensor Charging During the vast majority of the Van Allen Probes mission, the low-density and sunlit conditions encountered meant that the spacecraft floating potential was positive such that the sensor potential $V_i = V_{pi} - V_{sc}$ ($i = 1-6$) was negative. Occasionally, during particularly active times, excessive spacecraft charging occurred. A clear example was during the 2012-11-14 geomagnetic storm, shown in Fig. 26, where an influx of energetic (tens of keV) electrons during the first apogee caused the Van Allen Probe B spacecraft body to float negatively relative to the spheres. This is shown as positive excursions in panel (c) which plots the negative of the spacecraft potential $-V_{sc} = (V_1 + V_2)/2$. This excessive charging reduced the dynamic range of the sensor preamps, and when this potential exceeded (negative sense) the power supply *rail voltage* of -225 volts the preamp could no longer drive the signal and dropouts occurred (shown most prominently from $\sim 03:00-03:30$ UT). These times of extreme charging led to unrealistically large electric fields.

This type of charging can be separated from the more typical potential fluctuations that occur along the Van Allen Probe orbit (e.g., the second apogee pass on this day) by compar-

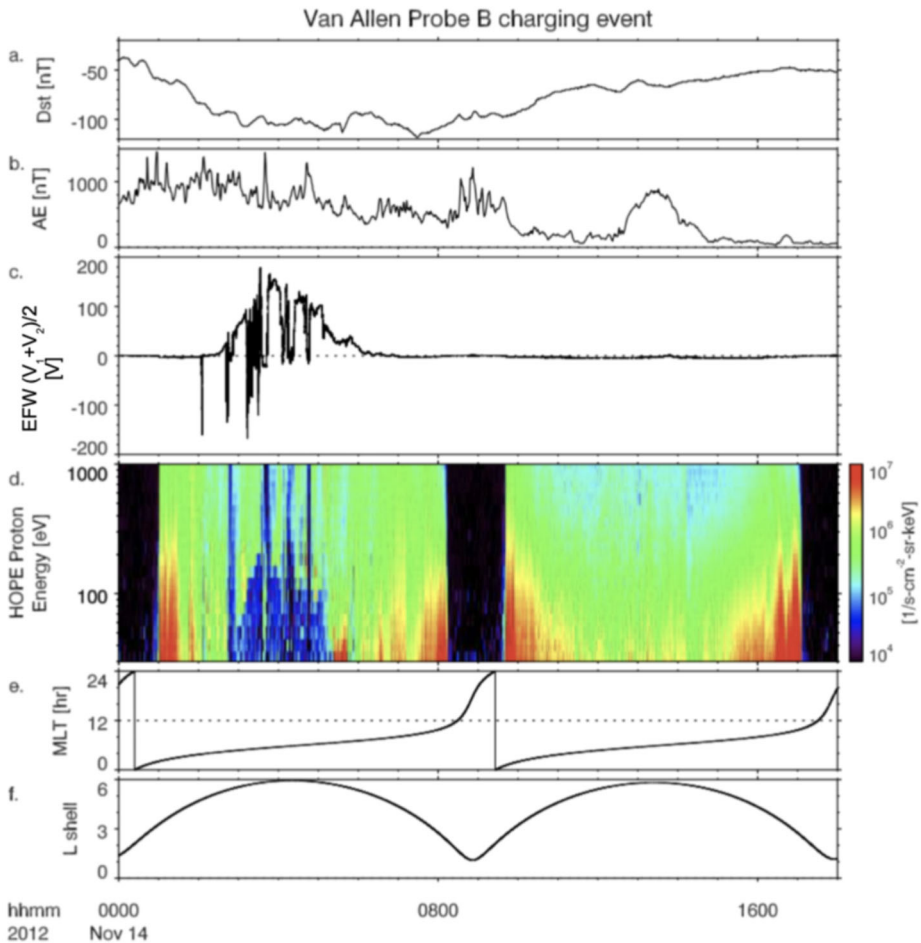


Fig. 26 Van Allen Probe B charging during the 2012-11-14 geomagnetic storm. Panels (a, b) show DST and AE indices. Panel (c) plots the negative spacecraft potential $-V_{sc} = (V_1 + V_2)/2$. Panel (e) shows the HOPE proton energy spectrum modified by the excessive spacecraft charging. Panels (f, g) show the magnetic local time and L-shell of Van Allen Probe B

ison with HOPE low energy ion fluxes (panel d), which are modified by spacecraft charging (e.g., Sarno-Smith et al. 2016). The clear dropout during the charging event occurred because protons at those energies were accelerated by the negatively charged spacecraft to energies greater than the spacecraft potential.

To track times of excessive charging, each probe has its own flag ($V[1-6]_{saturation}$). The flag is 1 when the sensor potential (measured relative to the spacecraft (sc) body as $V_i = V_{pi} - V_{sc}$, where V_{pi} and V_{sc} are the floating potentials of the sensor and spacecraft, respectively) is $V_i > 195$ volts. If any of these flags correspond to a sensor used to produce spin-fit data then the global flag is triggered. For example, if the spin-fit data is derived from the V_1 and V_2 probes, then the global flag will only be triggered if excessive charging occurs in V_1 and/or V_2 .

To identify all times when excessive charging occurred, two additional, more restrictive, charging flags are used, and both trigger the global flag. A general *charging* flag is used to

indicate times when the average of opposing antenna sensor pairs (e.g., $(V_i + V_j)/2$) satisfies the following condition: $(V_i + V_j)/2 > 0$ volts at $L > 4$. This flag was designed to identify less extreme charging events where data quality may still be compromised. For example, the sensors are particularly susceptible to potential fluctuations during magnetosheath encounters during extremely low-density conditions. An additional *extreme charging* flag is triggered when $(V_i + V_j)/2 > 20$ volts at $L > 4$, or where $(V_i + V_j)/2 < -20$ volts. $L < 4$ data are only flagged by the *V[1-6]_saturation* flag. Extreme charging was more common in the early mission when the sensors were more heavily biased and there were several significant geomagnetic storms. The negative value trigger is in place to catch times of saturation when sensor potentials can drop to the rail values (see negative spikes in Fig. 26). As the names suggest, caution or extreme caution should be used when examining data during these times. All charging events are flagged within ± 10 min of charging onset/offset.

Eclipse Flag The *eclipse* flag is also related to spacecraft charging. During eclipse (both umbra and penumbra) the spacecraft tends to charge to large negative potentials due to the lack of photoemission. Due to the difficulty of controlling these potentials, EFW did not attempt to maintain sensor potentials near the plasma potential with biasing, but allowed them to *float* relative to the plasma. Note that the eclipse flag is padded by ± 10 min relative to the entry/exit of eclipse.

Boom Flags In addition to monitoring the charging status of each boom using the charging and extreme charging flags, EFW also considered whether all the single-ended potentials are consistent with each other. Consistency was quantified using V_{median} , defined as the median value of V_1 , V_2 , V_3 , and V_4 . The *boomflags* are 1 when $|V_i - V_{\text{median}}| > 5$ volts, a threshold chosen empirically based on a comprehensive analysis of the entire spin-fit dataset. The flags *boomflag5* and *boomflag6* were not used. This metric not only effectively flagged problematic spin-fit electric fields, but also was used in selecting the best probe pair for calculating the spin-fit electric field.

Flags Related to Maneuvers, Deployments

Maneuver Flag There are a number of data quality issues associated with spacecraft acceleration events, including maneuvers and attitude adjustments. Maneuvers, related to orbit change or collision avoidance, occurred only a handful of times. Attitude adjustments were more frequent, occurring roughly once per month in order to keep the spacecraft spin axis in its near sun-pointing direction. Electric field data can be significantly compromised during and for some time after these events and are flagged with the *maneuvers* flag. Decreased quality occurs during the maneuver and for a short time after due to any plasma plume created by thruster firings, and due to uncertainties in the attitude solution. Note that the attitude adjustment maneuvers induced long period (> 5 min) wobbles in the booms that manifested as oscillations in the potentials and electric fields lasting for up to one day at > 3 RE and up to five days at < 3 RE. These are not flagged and are discussed at the end of this chapter.

EFW_deploy Flag Early in the mission, antenna deployments occurred frequently as the sensors, with their large moment of inertia, were carefully deployed in stages. These times are flagged with the *EFW_deploy* flag. All spin plane booms reached full deployment on both spacecraft on Sept 22, 2012, and all axial booms reached full deployment on Jan 7th, 2012. All L2 and L3 EFW data products make use of the proper antenna physical length after each deployment. A list of all boom deployments can be found at <https://spdf.gsfc.nasa.gov/pub/data/rbsp/documents/efw/>.

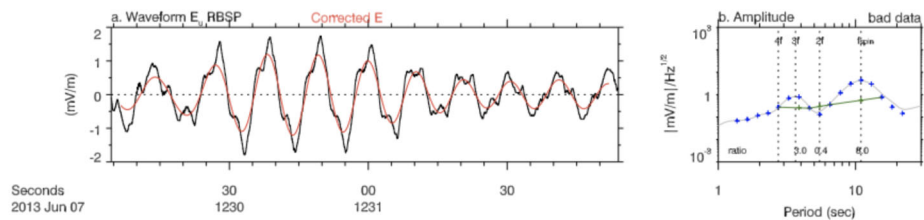


Fig. 27 The black sine wave in the left panel is the measured electric field on Van Allen Probe B showing a clear twice per spin period distortion caused by a wake effect. The red curve is the same signal with the wake effect removed. The right panel shows the wavelet analysis used to detect (over 10 spin periods) enhancements in power at spin period harmonics of 2, 3, and 4, which suggest the presence of a wake effect

Flags Related to Other Data Quality Issues We now discuss flags that do NOT trigger the global flag but are important in evaluating the data quality of the EFW data products.

Autobias Flag Following a flight software update on March 19, 2014, an auto biasing scheme was introduced that allowed automated onboard control of bias currents based on the measured spacecraft potential (V_{12}). This dynamic approach was designed to maximize sensor sensitivity over the wide range of densities and temperatures encountered over an orbit. This scheme, with times indicated by the *autobias* flag, was used on Van Allen Probe B for the remainder of the mission, and on Van Allen Probe A until shortly after Oct 2015 when V_1 performance degraded. Note that the *autobias* flag does not trigger the global flag because the autobiasing routine typically improved data quality. The flag was saved to evaluate the performance of the autobias algorithm.

Flag Related to Spin Fit Quality and the Possible Presence of Wake Effects Wake effects are a common error source present in double probe measurements (Engwall et al. 2006). These are observed, typically in low densities, when fast (supersonic) plasma flowing to downstream sensors is shielded by the large Debye sheath surrounding the spacecraft body (Bauer et al. 1983; Pedersen et al. 1984; Eriksson et al. 2006). Wake effects are observed as spin period distortions of the sensor potential (V_i). They are often parallel to the ambient magnetic field, and such *magnetic wakes* manifest as apparent field-aligned electric fields. Wake effects in EFW data, as shown in Fig. 27, are typically small ($< 1\text{--}2$ mV/m) in the spin plane due to the long boom lengths and antenna orientation. This error field can, however, be a significant fraction of the total electric field at times when the real electric fields are small (e.g., < 5 mV/m). As an example, the red curve shows a ~ 1 mV/m zero-peak real (wake-corrected) electric field that appears as a ~ 1.5 mV/m electric field with the wake effect.

Wake effects are identified with the *sine_wave_fit_quality* flag using a wavelet analysis to detect elevated power at harmonics of the spacecraft spin period (Fig. 27b). Specifically, peaks are detected over 120 sec (~ 10 spin periods) as power enhancements in both E_u and E_v (spin plane components) at spin period harmonics of 2, 3, and 4. Triggering of the wake flag requires simultaneous wake identification on both E_u and E_v . Note that, because the boom response to wakes of various strengths is complex, the flag for wake effect does not trigger the global flag. However, users are strongly encouraged to be cautious using wake-flagged data.

Density Flag A final flag related to sensor charging is the *density* flag. A very useful feature of EFW is the determination of plasma density from sensor potentials at a high cadence

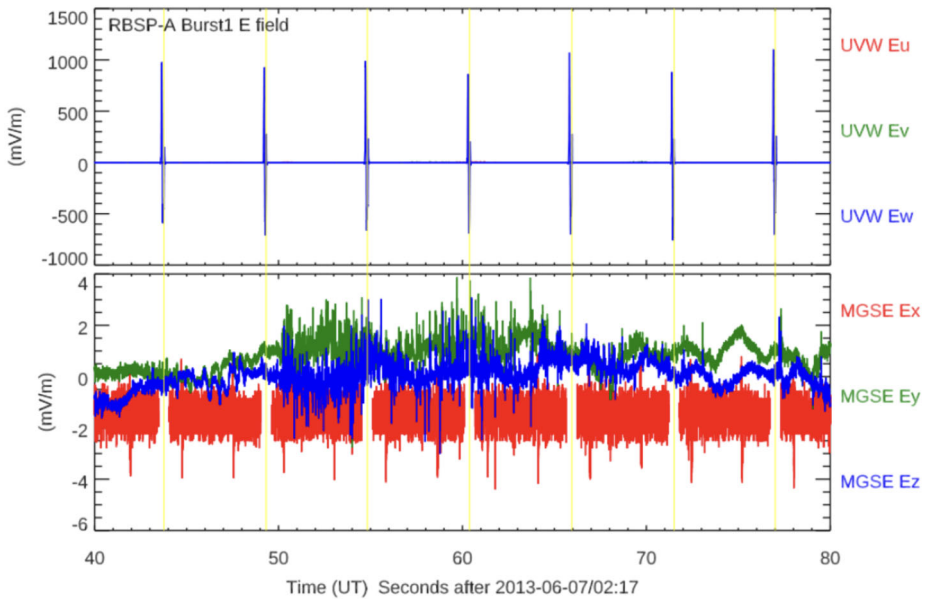


Fig. 28 Forty seconds of burst 1 electric field data showing the effects of spikes caused by shadowing of the V_5 boom by the spin plane wires. The shadowing, with times indicated by the yellow lines, is observed in (a) the E_w UVW component, which is derived from the potential difference $V_5 - V_6$. (b) The electric field rotated to MGSE coordinates after removal of the spikes. E_x MGSE is equivalent to E_w UVW

(16 S/sec). However, the calibration procedure that converts sensor potentials to density relies on the assumption that the spacecraft potential is driven by a cold plasma population. This can be violated at times when the `global_flag` is triggered. In addition, the sensor potential is only weakly dependent on density in tenuous plasmas. EFW thus flags density values when the density is determined to be $< 10 \text{ cm}^{-3}$. Values $> 3000 \text{ cm}^{-3}$ are also considered suspect and are removed. Note that it is often the case that density $< 10 \text{ cm}^{-3}$ values can be accurate, but careful analysis is required to determine when this is the case. Users should additionally take care when using EFW-determined density values during times of large electric field amplitudes which can modulate spacecraft surface potential in a way that can erroneously be interpreted as caused by density fluctuations (Malaspina et al. 2014a).

$\mathbf{E} * \mathbf{B} = 0$ Assumption (`spinaxis_Bo_angle`) Data quality are dependent on the magnetic field direction relative to the spin plane for data products that use the $\mathbf{E} * \mathbf{B} = 0$ assumption. When the angle between any of the spin plane directions and the magnetic field is less than ~ 15 deg, there is significant uncertainty in this calculation. These times are flagged with the variable `spinaxis_Bo_angle` and the spin axis derived data are removed.

Data Quality Issues That Are not Flagged We conclude this section by discussing two data quality issues that are not flagged: spikes in products derived from shadowing of the V_5 boom and oscillations in the booms following maneuvers.

Shadow Spikes in V_5 Spikes in data products derived from the anti-sunward boom potential V_5 are common and are caused by shadowing from the spin plane wires. An example of the effect this has on burst 1 electric field measurements is shown in Fig. 28. The shadow spikes (yellow lines) are identified using flags at

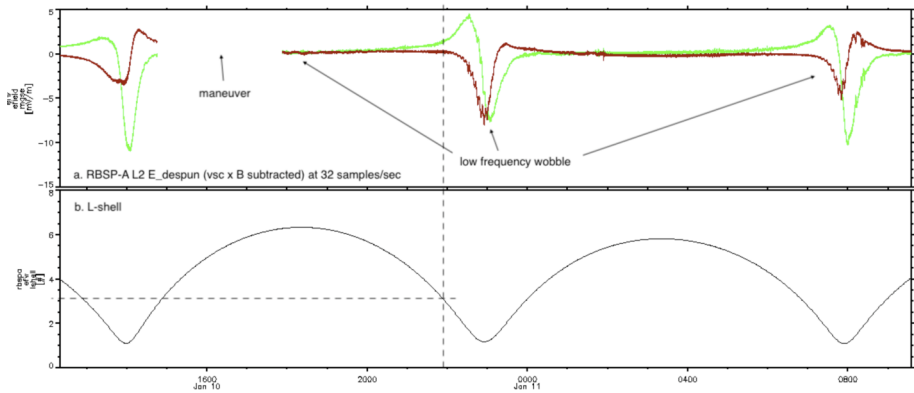


Fig. 29 An example of oscillations in the 32 Samples/sec spin plane electric field following an attitude adjustment maneuver on RBSPa near 15 UT on Jan 10th, 2013. E_y MGSE is green and E_z MGSE is red

RBSPa: <https://cdaweb.gsfc.nasa.gov/pub/data/rbsp/documents/emfisis/emfisis.physics.uiowa.edu/Events/rbsp-a/SP5antinsadow/>

RBSPb: <https://cdaweb.gsfc.nasa.gov/pub/data/rbsp/documents/emfisis/emfisis.physics.uiowa.edu/Events/rbsp-b/SP5antinsadow/>

Oscillations in Probe Potentials Following Maneuvers The Van Allen Probes underwent near-monthly attitude adjustment maneuvers in order to keep the spin axis pointed in the (roughly) sunward direction. These maneuvers induced small amplitude oscillations of the booms that were often detectable for days and which can present an issue for data analysis requiring very high accuracy quasi-static electric fields (e.g., Ali et al. 2016). An example of these low frequency (period larger than 5 min) oscillations can be seen in the electric field data shown in Fig. 29. The oscillation is largest around perigee (< 3 RE) due to the combination of large corotation and residual (imperfect subtraction of motional electric field) electric fields. The duration of these oscillations varied depending on the maneuver but typically decayed to the background level within 5 days post maneuver at < 3 RE and within 1 day at > 3 RE.

4.3.4 Software for EFW

The standard software package for access and analysis of the EFW dataset is through the SPEDAS package for IDL. The software is available as part of the IDL SPEDAS bleeding-edge software package (Angelopoulos et al. 2019). Installation instructions for this software can be found at http://spedas.org/wiki/index.php?title=Main_Page. Specific code for loading the electric field and related data at the cadence of spin period (~ 11 sec), survey mode (16 or 32 S/sec), and burst mode (512–16,384 S/sec) are documented at <https://pdf.gsfc.nasa.gov/pub/data/rbsp/documents/efw/>. Routines for loading supporting data related to EFW are also listed. Other software for loading the EFW CDF data products include pypedas <https://github.com/spedas/pyypedas> and autoplot <https://autoplot.org/>.

5 Summary

The Electric Field and Waves instruments on the twin Van Allen Probes have provided an unprecedented dataset of high-quality DC and AC electric field measurements throughout

the inner magnetosphere. This dataset has been used in combination with data from the other Van Allen Probes instruments and in collaboration with other missions in hundreds of publications addressing fundamental physics of the magnetosphere and ionosphere (as laid out by the primary mission science goals) and providing exciting new discoveries. The final calibrated dataset, described in detail in this chapter, will remain highly relevant for decades to come.

Acknowledgements The EFW team offers sincere thanks to the many Van Allen Probes scientists, engineers, management, and staff who contributed to the success of this project. We particularly thank D. Sibeck (LWS Mission Scientist) at NASA, and B. Mauk, N. Fox, A. Y. Ukhorskiy (Project Management), R. Harvey, and T. Sotirelis (Spacecraft Operations) at the Applied Physics Laboratory (APL).

We are also grateful for support from our Van Allen Probes colleagues at EMFISIS (C. Kletzing), the ECT suite of instruments (H. Spence) including HOPE (G. Reeves), REPT (D. Baker), and MagEIS (J.B. Blake), BARREL (R. Millan, A. Halford, L. Woodger), as well as support involving collaborative campaigns including FIREBIRD (D. Klumpar, J. Sample, A. Johnson, M. Shumko), Aerocube 6 (J.B. Blake), WWLLN (R.H. Holzworth), and Arase (Y. Miyoshi).

We additionally thank the many engineers, technicians, managers, and support staff at the University of California, Berkeley, the University of Colorado, Laboratory for Atmospheric and Space Physics, and the University of Minnesota including: D. Pankow, D.W. Curtis, H. Richard, K. Harps, J. McCauley, P. Schroeder, J. McTiernan, J.B. Tao, M. Ludlam, P. Turin, M.K. Bolton, D.A. Gordon, B. Donakowski, J. Fischer, S. Heavner, P.C. Berg, C. Shultz, M. Diaz-Aguado, S. Boardsen, W. Rachelson, C. Ingraham, J. Hoberman, R.A. Hochman, M. Born, J. Vernetti, W. Teitler, G. Johnson, R. Jackson, M. Willer, M. Mendoza, H. Yuan, Y. Irwin, B. Dalen, T. McDonald, S. Marker, W. Cole, M. Karlsson, K. Stevens, D. Summers, S. Westfall, J. Lynch, S. Monson.

Finally, thanks to those who supported EFW software development for the SPEDAS library including J. Lewis and V. Angelopoulos, and for data archiving including R.E. McGuire and R.M. Candey.

Funding The Van Allen Probes EFW project was supported by JHU/APL Contract No. 922613 under NASA's Prime Contract No. NNN06AA01C.

Declarations

Competing Interests The authors declare no competing interests.

Open Access This article is licensed under a Creative Commons Attribution 4.0 International License, which permits use, sharing, adaptation, distribution and reproduction in any medium or format, as long as you give appropriate credit to the original author(s) and the source, provide a link to the Creative Commons licence, and indicate if changes were made. The images or other third party material in this article are included in the article's Creative Commons licence, unless indicated otherwise in a credit line to the material. If material is not included in the article's Creative Commons licence and your intended use is not permitted by statutory regulation or exceeds the permitted use, you will need to obtain permission directly from the copyright holder. To view a copy of this licence, visit <http://creativecommons.org/licenses/by/4.0/>.

References

- Agapitov OV et al (2015) Nonlinear local parallel acceleration of electrons through Landau trapping by oblique whistler mode waves in the outer radiation belt. *Geophys Res Lett* 42(23):2015GL066887. <https://doi.org/10.1002/2015GL066887>
- Agapitov OV et al (2017) Chorus whistler wave source scales as determined from multipoint Van Allen Probe measurements. *Geophys Res Lett* 44:2634–2642. <https://doi.org/10.1002/2017GL072701>
- Agapitov OV et al (2018a) Synthetic empirical chorus wave model from combined Van Allen Probes and Cluster statistics. *J Geophys Res Space Phys* 123:297–314. <https://doi.org/10.1002/2017JA024843>
- Agapitov OV et al (2018b) Nonlinear electrostatic steepening of whistler waves: the guiding factors and dynamics in inhomogeneous systems. *Geophys Res Lett* 45:2168–2176. <https://doi.org/10.1002/2017GL076957>

- Agapitov OV et al (2019) Time scales for electron quasi-linear diffusion by lower-band chorus waves: the effects of ω_{pe}/Ω_{ce} dependence on geomagnetic activity. *Geophys Res Lett* 46:6178–6187. <https://doi.org/10.1029/2019GL083446>
- Agapitov OV et al (2021) Chorus and hiss scales in the inner magnetosphere: statistics from high-resolution filter bank (FBK) Van Allen Probes multi-point measurements. *J Geophys Res Space Phys* 126:e2020JA028998. <https://doi.org/10.1029/2020JA028998>
- Ali AF et al (2016) Electric and magnetic radial diffusion coefficients using the Van Allen probes data. *J Geophys Res Space Phys* 121:9586–9607. <https://doi.org/10.1002/2016JA023002>
- An X et al (2021) Nonlinear Landau resonant interaction between kinetic Alfvén waves and thermal electrons: excitation of time domain structures. *J Geophys Res Space Phys* 126:e2020JA028643. <https://doi.org/10.1029/2020JA028643>
- Andersson L et al (2009) New features of electron phase space holes observed by the THEMIS Mission. *Phys Rev Lett* 102(22):225004. <https://doi.org/10.1103/PhysRevLett.102.225004>
- Angelopoulos V et al (2019) The Space Physics Environment Data Analysis System (SPEDAS). *Space Sci Rev* 215:9. <https://doi.org/10.1007/s11214-018-0576-4>
- Artemyev AV et al (2014) Fast transport of resonant electrons in phase space due to nonlinear trapping by whistler waves. *Geophys Res Lett* 41:5727–5733. <https://doi.org/10.1002/2014GL061380>
- Artemyev AV et al (2015) Electron trapping and acceleration by kinetic Alfvén waves in the inner magnetosphere. *J Geophys Res Space Phys* 120:10,305–10,316. <https://doi.org/10.1002/2015JA021781>
- Artemyev AV et al (2016) Oblique whistler-mode waves in the Earth's inner magnetosphere: energy distribution, origins, and role in radiation belt dynamics. *Space Sci Rev* 200:261–355. <https://doi.org/10.1007/s11214-016-0252-5>
- Baker DN et al (2013) A long-lived relativistic electron storage ring embedded in Earth's outer Van Allen belt. *Science* 340(6129):186–190. <https://doi.org/10.1126/science.1233518>
- Baker DN et al (2016) Highly relativistic radiation belt electron acceleration, transport, and loss: large solar storm events of March and June 2015. *J Geophys Res Space Phys* 121:6647–6660. <https://doi.org/10.1002/2016JA022502>
- Bale SD et al (1998) Bipolar electrostatic structures in the shock transition region: evidence of electron phase space holes. *Geophys Res Lett* 25(15):2929–2932
- Bauer OH et al (1983) Influence of wake and photoemission on electric field measurements with a double probe on GEOS-2. In: *Spacecraft/Plasma Interactions and their Influence on Field and Particle Measurements, Proceedings of the 17th ESLAB Symposium, ESA-SP*, pp 51–56
- Blake JB, O'Brien TP (2016) Observations of small-scale latitudinal structure in energetic electron precipitation. *J Geophys Res Space Phys* 121:3031–3035. <https://doi.org/10.1002/2015JA021815>
- Blum L et al (2015) Rapid MeV electron precipitation as observed by SAMPEX/HILT during high-speed stream-driven storms. *J Geophys Res Space Phys* 120:3783–3794. <https://doi.org/10.1002/2014JA020633>
- Bonnell JW et al (2008) The Electric Field Instrument (EFI) for THEMIS. *Space Sci Rev* 141:303–341. <https://doi.org/10.1007/s11214-008-9469-2>
- Bortnik J et al (2016) Chorus waves in geospace and their influence on radiation belt dynamics, waves, particles, and storms in geospace. In: Balasis G, Daglis IA, Mann IR (eds) *Waves, Particles, and Storms in Geospace: A Complex Interplay*. Oxford University Press, London, pp 192–216. <https://doi.org/10.1093/acprof:oso/9780198705246.003.0009>
- Breneman AW et al (2015) Global-scale coherence modulation of radiation-belt electron loss from plasmaspheric hiss. *Nature* 523:193–195. <https://doi.org/10.1038/nature14515>
- Breneman AW et al (2017) Observations directly linking relativistic electron microbursts to whistler mode chorus: Van Allen Probes and FIREBIRD II. *Geophys Res Lett* 44:11,265–11,272. <https://doi.org/10.1002/2017GL075001>
- Breneman AW et al (2020) Driving of outer belt electron loss by solar wind dynamic pressure structures: evidence of balloon and satellite data. *J Geophys Res Space Phys* 125:e2020JA028097. <https://doi.org/10.1029/2020JA028097>
- Califf S et al (2016a) Large-amplitude electric fields in the inner magnetosphere: Van Allen Probes observations of subauroral polarization streams. *J Geophys Res Space Phys* 121:5294–5306. <https://doi.org/10.1002/2015JA022252>
- Califf S et al (2016b) Empirical estimates and theoretical predictions of the shorting factor for the THEMIS double-probe electric field instrument: THEMIS Shorting Factor. *J Geophys Res Space Phys* 121(7):6223–6233. <https://doi.org/10.1002/2016JA022589>
- Califf S et al (2017) The role of the convection electric field in filling the slot region between the inner and outer radiation belts. *J Geophys Res Space Phys* 122:2051–2068. <https://doi.org/10.1002/2016JA023657>

- Carlson CW et al (1998) The Fast Auroral SnapshoT (FAST) mission. *Geophys Res Lett* 25:2013–2016. <https://doi.org/10.1029/98GL01592>
- Carpenter DL, Lemaire J et al (2004) The plasmasphere boundary layer. *Ann Geophys* 22:4291–4298. <https://doi.org/10.5194/angeo-22-4291-2004>
- Cattell CA et al (2002) Polar observations of solitary waves at the Earth's magnetopause. *Geophys Res Lett* 29:5. <https://doi.org/10.1029/2001GL014046/>
- Cattell CA et al (2005) Cluster observations of electron holes in association with magnetotail reconnection and comparison to simulations. *J Geophys Res.* <https://doi.org/10.1029/2004JA010519>
- Cattell CA et al (2008) Discovery of very large amplitude whistler-mode waves in Earth's radiation belts. *Geophys Res Lett* 35:L01105. <https://doi.org/10.1029/2007GL032009>
- Cattell CA et al (2017) Dayside response of the magnetosphere to a small shock compression: Van Allen Probes, Magnetospheric MultiScale, and GOES-13. *Geophys Res Lett* 44:8712–8720. <https://doi.org/10.1002/2017GL074895>
- Chaston CC et al (2012) Correction to “Energy transport by kinetic-scale electromagnetic waves in fast plasma sheet flows”. *J Geophys Res* 117:A12205. <https://doi.org/10.1029/2012JA018476>
- Chaston CC et al (2014) Observations of kinetic scale field line resonances. *Geophys Res Lett* 41:209–215. <https://doi.org/10.1002/2013GL058507>
- Chaston CC et al (2015a) Broadband low frequency electromagnetic waves in the inner magnetosphere. *J Geophys Res Space Phys.* <https://doi.org/10.1002/2015JA021690>
- Chaston CC et al (2015b) Extreme ionospheric ion energization and electron heating in Alfvén waves in the storm time inner magnetosphere. *Geophys Res Lett* 42:10,531–10,540. <https://doi.org/10.1002/2015GL066674>
- Chaston CC et al (2016) Driving ionospheric outflows and magnetospheric O⁺ energy density with Alfvén waves. *Geophys Res Lett* 43:4825–4833. <https://doi.org/10.1002/2016GL069008>
- Chaston CC et al (2018) Pitch angle scattering and loss of radiation belt electrons in broadband electromagnetic waves. *Geophys Res Lett* 45:9344–9352. <https://doi.org/10.1029/2018GL079527>
- Chu X et al (2019) Identifying STEVE's magnetospheric driver using conjugate observations in the magnetosphere and on the ground. *Geophys Res Lett* 46:12665–12674. <https://doi.org/10.1029/2019GL082789>
- Colpitts CA et al (2016) Van Allen Probes observations of cross-scale coupling between electromagnetic ion cyclotron waves and higher-frequency wave modes. *Geophys Res Lett* 43:11,510–11,518. <https://doi.org/10.1002/2016GL071566>
- Colpitts C et al (2020) First direct observations of propagation of discrete chorus elements from the equatorial source to higher latitudes using the Van Allen Probes and Arase satellites. *J Geophys Res* 125:e2020JA028315. <https://doi.org/10.1029/2020JA028315>
- Crew AB et al (2016) First multipoint in situ observations of electron microbursts: initial results from the NSF FIREBIRD II mission. *J Geophys Res Space Phys* 121:5272–5283. <https://doi.org/10.1002/2016JA022485>
- Dai L et al (2013) Excitation of poloidal standing Alfvén waves through drift resonance wave-particle interaction. *Geophys Res Lett* 16:4127–4132. <https://doi.org/10.1002/grl.50800>
- Damiano PA et al (2018) Electron distributions in kinetic scale field line resonances: a comparison of simulations and observations. *Geophys Res Lett* 45:5826–5835. <https://doi.org/10.1029/2018GL077748>
- Dowden RL et al (2002) VLF lightning location by time of group arrival (TOGA) at multiple sites. *J Atmos Sol-Terr Phys* 64:817–830. [https://doi.org/10.1016/S1364-6826\(02\)00085-8](https://doi.org/10.1016/S1364-6826(02)00085-8)
- Engwall E et al (2006) Low-energy (order 10 eV) ion flow in the magnetotail lobes inferred from spacecraft wake observations. *Geophys Res Lett* 33, L06110. <https://doi.org/10.1029/2005GL025179>
- Ergun RE et al (1998) FAST satellite observations of electric field structures in the auroral zone. *Geophys Res Lett* 25(12):2025–2028. <https://doi.org/10.1029/98GL00635>
- Ergun RE et al (2001) The FAST satellite field instrument. *Space Sci Rev* 98(1/2):67–91. <https://doi.org/10.1023/A:1013131708323>
- Ergun RE et al (2016) Magnetospheric multiscale satellites observations of parallel electric fields associated with magnetic reconnection. *Phys Rev Lett* 116:235102
- Eriksson A et al (2006) Electric field measurements on Cluster: comparing the double-probe and electron drift techniques. *Ann Geophys* 24:275–289. <https://doi.org/10.5194/angeo-24-275-2006>
- Fahleson U (1967) Theory of electric field measurements conducted in the magnetosphere with electric probes. *Space Sci Rev* 7:238–262. <https://doi.org/10.1007/BF00215600>
- Falthammer CG et al (1987) Preliminary results from the dc electric field experiment on the Viking Satellite. *Ann Geophys, Ser A* 5(4):171–175
- Foster JC, Burke WJ (2002) SAPS: a new categorization for sub-auroral electric fields. *Eos Trans AGU* 83(36):393–394. <https://doi.org/10.1029/2002EO000289>
- Foster JC et al (2014) Stormtime observations of plasmasphere erosion flux in the magnetosphere and ionosphere. *Geophys Res Lett* 41:762–768. <https://doi.org/10.1002/2013GL059124>

- Foster JC et al (2015) Shock-induced prompt relativistic electron acceleration in the inner magnetosphere. *J Geophys Res Space Phys* 120:1661–1674. <https://doi.org/10.1002/2014JA020642>
- Foster JC et al (2020) Multi-point observations of the geospace plume. In: Zong Q, Escoubet P, Sibeck D, Le G, Zhang H (eds) *Dayside Magnetosphere Interactions*. Geophys. Monograph Series, vol 248. Wiley, New York, pp 243–264. <https://doi.org/10.1002/9781119509592.ch14>
- Gkioulidou M et al (2019) Low-energy (< keV) O⁺ ion outflow directly into the inner magnetosphere: Van Allen Probes observations. *J Geophys Res Space Phys* 124:405–419. <https://doi.org/10.1029/2018JA025862>
- Green A et al (2020) Properties of lightning generated whistlers based on Van Allen Probes observations and their global effects on radiation belt electron loss. *Geophys Res Lett* 47:e2020GL089584. <https://doi.org/10.1029/2020GL089584>
- Gustafsson GB et al (1997) The electric field and wave experiment for the Cluster mission. *Space Sci Rev* 79:137–156. <https://doi.org/10.1023/A:1004975108657>
- Gustafsson GB et al (2001) First results of electric field and density observations by Cluster EFW based on initial months of operation. *Ann Geophys* 19(6):1219–1240. <https://doi.org/10.5194/angeo-19-1219-2001>
- Halford AJ et al (2016) BARREL observations of a solar energetic electron and solar energetic proton event. *J Geophys Res Space Phys* 121:4205–4216. <https://doi.org/10.1002/2016JA022462>
- Hartley DP et al (2016) Using the cold plasma dispersion relation and whistler mode waves to quantify the antenna sheath impedance of the Van Allen Probes EFW instrument. *J Geophys Res Space Phys* 121:4590–4606. <https://doi.org/10.1002/2016JA022501>
- Hartley DP et al (2017) An improved sheath impedance model for the Van Allen Probes EFW instrument: effects of the spin axis antenna. *J Geophys Res Space Phys* 122:4420–4429. <https://doi.org/10.1002/2016JA023597>
- Hartley DP et al (2022) Quantifying the sheath impedance of the electric double probe instrument on the Van Allen Probes. *J Geophys Res Space Phys* 127:e2022JA030369. <https://doi.org/10.1029/2022JA030369>
- Harvey P et al (1995) The electric field instrument on the polar satellite. *Space Sci Rev* 71:583–596. <https://doi.org/10.1007/BF00751342>
- Hayakawa H et al (1990) Electric field experiment on the Akebono (EXOS-D) Satellite. *J Geomagn Geoelectr* 42(4):371–384
- Horne RB, Thorne RM (2003) Relativistic electron acceleration and precipitation during resonant interactions with whistler-mode chorus. *Geophys Res Lett* 30:1527. <https://doi.org/10.1029/2003GL016973>
- Horne RB et al (2016) Wave-driven diffusion in radiation belt dynamics. In: Balasis G, Daglis IA, Mann IR (eds) *Waves, Particles, and Storms in Geospace: A Complex Interplay*. Oxford University Press, London, pp 217–243. <https://doi.org/10.1093/acprof:oso/9780198705246.003.0010>
- Hudson MK et al (2015) Modeling CME-shock driven storms in 2012–2013: MHD-test particle simulations. *J Geophys Res*. <https://doi.org/10.1002/2014JA020833>
- Hudson M et al (2017) Simulated prompt acceleration of multi-MeV electrons by the 17 March 2015 interplanetary shock. *J Geophys Res Space Phys* 122:10,036–10,046. <https://doi.org/10.1002/2017JA024445>
- Hull AJ et al (2019) Dispersive Alfvén wave control of O⁺ ion outflow and energy densities in the inner magnetosphere. *Geophys Res Lett* 46:8597–8606. <https://doi.org/10.1029/2019GL083808>
- Hull AJ et al (2020) Correlations between dispersive Alfvén wave activity, electron energization, and ion outflow in the inner magnetosphere. *Geophys Res Lett* 47:17. <https://doi.org/10.1029/2020GL088985>
- Jacobs JA et al (1964) Classification of geomagnetic micropulsations. *J Geophys Res* 69(1):180–181. <https://doi.org/10.1029/JZ069i001p00180>
- Jahn JM et al (2020) Determining plasmaspheric density from the upper hybrid resonance and from the spacecraft potential: how do they compare? *J Geophys Res Space Phys* 125:e2019JA026860. <https://doi.org/10.1029/2019JA026860>
- Jaynes AN et al (2015) Source and seed populations for relativistic electrons: their roles in radiation belt changes. *J Geophys Res Space Phys* 120:7240–7254. <https://doi.org/10.1002/2015JA021234>
- Johnson AT et al (2020) The FIREBIRD-II CubeSat mission: focused investigations of relativistic electron burst intensity, range, and dynamics. *Rev Sci Instrum* 91:034503. <https://doi.org/10.1063/1.5137905>
- Kanekal SG et al (2016) Prompt acceleration of magnetospheric electrons to ultrarelativistic energies by the 17 March 2015 interplanetary shock. *J Geophys Res Space Phys* 121:7622–7635. <https://doi.org/10.1002/2016JA022596>
- Keiling A et al (2003) The global morphology of wave Poynting flux: powering the aurora. *Science* 299:383–386
- Kellogg PJ et al (2010) Electron trapping and charge transport by large amplitude whistlers. *Geophys Res Lett* 37:L20106. <https://doi.org/10.1029/2010GL044845>

- Kellogg PJ et al (2011) Large amplitude whistlers in the magnetosphere observed with wind-waves. *J Geophys Res*. <https://doi.org/10.1029/2010JA015919>
- Kepko L et al (2002) ULF waves in the solar wind as direct drivers of magnetospheric pulsations. *Geophys Res Lett* 29(8):39-1–39-4. <https://doi.org/10.1029/2001GL014405>
- Kirby K, Artis D, Bushman S et al (2013) Radiation belt storm probes—observatory and environments. *Space Sci Rev* 179:59–125. <https://doi.org/10.1007/s11214-012-9949-2>
- Kletzing CA et al (2013) The electric and magnetic field instrument suite and integrated science (EMFISIS) on RBSP. *Space Sci Rev* 179:127–181. <https://doi.org/10.1007/s11214-013-9993-6>
- Klumpar D et al (2015) Flight system technologies enabling the twin-CubeSat FIREBIRD-II scientific mission. In: Proceedings of the 29th Annual AIAA/USU Conference on Small Satellites, Technical Section V: Year in Review, SSC15-V-6
- Kurth WS et al (2015) Electron densities inferred from plasma wave spectra obtained by the Waves instrument on Van Allen Probes. *J Geophys Res Space Phys* 120(2):904–914. <https://doi.org/10.1002/2014JA020857>
- Lejosne S, Mozer FS (2016a) Van Allen Probe measurements of the electric drift $\mathbf{E} \times \mathbf{B}/B^2$ at Arecibo's $L = 1.4$ field line coordinate. *Geophys Res Lett* 43:6768–6774. <https://doi.org/10.1002/2016GL069875>
- Lejosne S, Mozer FS (2016b) Typical values of the electric drift $\mathbf{E} \times \mathbf{B}/B^2$ in the inner radiation belt and slot region as determined from Van Allen Probe measurements. *J Geophys Res Space Phys* 121:12,014–12,024. <https://doi.org/10.1002/2016JA023613>
- Lejosne S, Mozer FS (2018) Magnetic activity dependence of the electric drift below $L = 3$. *Geophys Res Lett* 45:3775–3782. <https://doi.org/10.1029/2018GL077873>
- Lejosne S, Mozer FS (2019) Shorting factor in-flight calibration for the Van Allen Probes DC electric field measurements in the Earth's plasmasphere. *Earth Space Sci* 6:646–654. <https://doi.org/10.1029/2018EA000550>
- Lejosne S, Mozer FS (2020) Experimental determination of the conditions associated with “zebra stripe” pattern generation in the Earth's inner radiation belt and slot region. *J Geophys Res Space Phys* 125:e2020JA027889. <https://doi.org/10.1029/2020JA027889>
- Lejosne S et al (2021) Thermospheric neutral winds as the cause of drift shell distortion in Earth's inner radiation belt. *Front Astron Space Sci* 8:725800. <https://doi.org/10.3389/fspas.2021.725800>
- Lejosne S et al (2021) Maximizing the accuracy of double probe electric field measurements near perigee: the case of the Van Allen Probes instruments. *Geophys Res Space Phys* 127, e2021JA030099. <https://doi.org/10.1029/2021JA030099>
- Lena FR et al (2021) Detection of hertz frequency multiharmonic field line resonances at Low-L ($L = 1.1$ – 1.5) during Van Allen Probe perigee passes. *Geophys Res Lett* 48:e2020GL090632. <https://doi.org/10.1029/2020GL090632>
- Li X et al (1993) Simulation of prompt energization and transport of radiation belt particles during the March 24, 1991 SSC. *Geophys Res Lett* 20:2423
- Li J et al (2017) Coherently modulated whistler mode waves simultaneously observed over unexpectedly large spatial scales. *J Geophys Res Space Phys* 122:1871–1882. <https://doi.org/10.1002/2016JA023706>
- Lindqvist PA et al (2016) The spin-plane double probe electric field instrument for MMS. *Space Sci Rev* 199:137–165. <https://doi.org/10.1007/s11214-014-0116-9>
- Lysak RL, Lotko W (1996) On the kinetic dispersion relation for shear Alfvén waves. *J Geophys Res* 101(A3):5085–5094. <https://doi.org/10.1029/95JA03712>
- MacDonald EA et al (2018) New science in plain sight: citizen scientists lead to the discovery of optical structure in the upper atmosphere. *Sci Adv* 4:eaq0030
- Malaspina DM et al (2014a) Chorus waves and spacecraft potential fluctuations: evidence for wave-enhanced photoelectron escape. *Geophys Res Lett* 41:236–243. <https://doi.org/10.1002/2013GL058769>
- Malaspina DM et al (2014b) Nonlinear electric field structures in the inner magnetosphere. *Geophys Res Lett* 41:5693–5701. <https://doi.org/10.1002/2014GL061109>
- Malaspina DM et al (2015) Kinetic Alfvén waves and particle response associated with a shock-induced, global ULF perturbation of the terrestrial magnetosphere. *Geophys Res Lett* 42:9203–9212. <https://doi.org/10.1002/2015GL065935>
- Malaspina DM et al (2016) The distribution of plasmaspheric hiss wave power with respect to plasmopause location. *Geophys Res Lett* 43:7878–7886. <https://doi.org/10.1002/2016GL069982>
- Malaspina DM et al (2017) Statistical properties of low-frequency plasmaspheric hiss. *J Geophys Res Space Phys* 122:8340–8352. <https://doi.org/10.1002/2017JA024328>
- Malaspina DM et al (2018a) Variation in plasmaspheric hiss wave power with plasma density. *Geophys Res Lett* 45:9417–9426. <https://doi.org/10.1029/2018GL078564>
- Malaspina DM et al (2018b) A census of plasma waves and structures associated with an injection front in the inner magnetosphere. *J Geophys Res* 123:2566–2587. <https://doi.org/10.1002/2017JA025005>

- Malaspina DM et al (2020) A wave model and diffusion coefficients for plasmaspheric hiss parameterized by plasmopause location. *J Geophys Res Space Phys* 125:e2019JA027415. <https://doi.org/10.1029/2019JA027415>
- Marklund G, Blomberg LG, Lindqvist P-A, Fälthammar C-G, Haerendel G, Mozer FS, Pedersen A, Tanakanen P (1994) The double probe electric field experiment on Freja: experiment description and first results. *Space Sci Rev* 70:483–508. <https://doi.org/10.1007/BF00756883>
- Marklund G et al (2004) Characteristics of quasi-static potential structures observed in the auroral return current region by Cluster. *Nonlinear Process Geophys* 11:709–720. <https://doi.org/10.5194/npg-11-709-2004>
- Matsuda S et al (2021) Multipoint measurement of fine-structured EMIC waves by Arase, Van Allen Probe A, and ground stations. *Geophys Res Lett* 48:e2021GL096488. <https://doi.org/10.1029/2021GL096488>
- Mauk BH et al (2013) Science objectives and rationale for the radiation belt storm probes mission. *Space Sci Rev* 179:3–27. <https://doi.org/10.1007/s11214-012-9908-y>
- Menz AM et al (2019) Efficacy of electric field models in reproducing observed ring current ion spectra during two geomagnetic storms. *J Geophys Res Space Phys* 124(11):8974–8991. <https://doi.org/10.1029/2019JA026683>
- Millan RM et al (2013) The Balloon Array for RBSP Relativistic Electron Losses (BARREL). *Space Sci Rev* 179:503–530. <https://doi.org/10.1007/s11214-013-9971-z>
- Min K et al (2017) Second harmonic poloidal waves observed by Van Allen Probes in the dusk-midnight sector. *J Geophys Res Space Phys* 122:3013–3039. <https://doi.org/10.1002/2016JA023770>
- Mishin EV et al (2013) Interaction of substorm injections with the subauroral geospace: 1. Multispacecraft observations of SAID. *J Geophys Res Space Phys* 118:5782–5796. <https://doi.org/10.1002/jgra.50548>
- Miyoshi Y et al (2018) Geospace exploration project ERG. *Earth Planets Space* 70(1):101. <https://doi.org/10.1186/s40623-018-0862-0>
- Miyoshi Y et al (2019) EMIC waves converted from equatorial noise due to $M/Q = 2$ ions in the plasmasphere: observations from Van Allen Probes and Arase. *Geophys Res Lett* 46:5662–5669. <https://doi.org/10.1029/2019GL083024>
- Miyoshi Y et al (2022) Collaborative research activities of the Arase and Van Allen Probes. *Space Sci Rev* 218:38. <https://doi.org/10.1007/s11214-022-00885-4>
- Mourenas D et al (2015) Very oblique whistler generation by low-energy electron streams. *J Geophys Res Space Phys* 120(5):2015JA021135. <https://doi.org/10.1002/2015JA021135>
- Moya PS et al (2015) Weak kinetic Alfvén waves turbulence during the 14 November 2012 geomagnetic storm: Van Allen Probes observations. *J Geophys Res Space Phys* 120:5504–5523. <https://doi.org/10.1002/2014JA020281>
- Mozer FS (2016) DC and low-frequency double probe electric field measurements in space. *J Geophys Res Space Phys* 121:10,942–10,953. <https://doi.org/10.1002/2016JA022952>
- Mozer FS et al (1973) Analysis of techniques for measuring DC and AC electric fields in the magnetosphere. *Space Sci Rev* 14:272–313. <https://doi.org/10.1007/BF02432099>
- Mozer FS et al (1978a) Measurements of quasi-static and low-frequency electric fields with spherical double probes on the ISEE-1 spacecraft. *IEEE Trans Geosci Electron* 16(3):258–261. <https://doi.org/10.1109/TGE.1978.294558>
- Mozer FS et al (1978b) Electric field measurements in the solar wind, bow shock, magnetosheath, magnetopause, and magnetosphere. *Space Sci Rev* 22:791–804. <https://doi.org/10.1007/BF00212624>
- Mozer FS et al (1979) The dc and ac electric field, plasma density, plasma temperature and field-aligned current experiments on the S3-3 spacecraft. *J Geophys Res* 84(A10):5875
- Mozer FS et al (2013) Megavolt parallel potentials arising from double-layer streams in the Earth's outer radiation belt. *Phys Rev Lett*. <https://doi.org/10.1103/PhysRevLett.111.235002>
- Mozer FS et al (2016) Near-relativistic electron acceleration by Landau trapping in time domain structures. *Geophys Res Lett* 43:508–514. <https://doi.org/10.1002/2015GL067316>
- Mozer FS et al (2017) Pulsating auroras produced by interactions of electrons and time domain structures. *J Geophys Res Space Phys* 122:8604–8616. <https://doi.org/10.1002/2017JA024223>
- Mozer FS et al (2018) Simultaneous observations of lower band chorus emissions at the equator and microburst precipitating electrons in the ionosphere. *Geophys Res Lett* 45(2):2017GL076120. <https://doi.org/10.1002/2017GL076120>
- O'Brien TP et al (2016) AeroCube-6 Dosimeter Data README (v3.0). Aerospace Report No. TOR-2016-01155
- Paral J et al (2015) Magnetohydrodynamic modeling of three Van Allen Probes storms in 2012 and 2013. *Ann Geophys* 33:1037–1050. <https://doi.org/10.5194/angeo-33-1037-2015>
- Patel M et al (2019) Simulation of prompt acceleration of radiation belt electrons during the 16 July 2017 storm. *Geophys Res Lett* 46:7222–7229. <https://doi.org/10.1029/2019GL083257>

- Pedersen A et al (1984) Quasistatic electric field measurements with spherical double probes on the GEOS and ISEE satellites. *Space Sci Rev* 37:269–312. <https://doi.org/10.1007/BF00226365>
- Pedersen A et al (1995) Solar wind and magnetospheric plasma diagnostics by spacecraft electrostatic potential measurements. *Ann Geophys* 13:118
- Pedersen A et al (1998) Electric field measurements in a tenuous plasma with spherical double probes. In: *Measurement Techniques in Space Plasmas*. RF Pfaf, JE Borovsky, DT Young (eds). <https://doi.org/10.1002/9781118664391.ch1>
- Pedersen A et al (2008) Electron density estimations derived from spacecraft potential measurements on Cluster in tenuous plasma regimes. *J Geophys Res* 113:A07S33. <https://doi.org/10.1029/2007JA012636>
- Posch JL et al (2015) Low-harmonic magnetosonic waves observed by the Van Allen Probes. *J Geophys Res Space Phys* 120:6230–6257. <https://doi.org/10.1002/2015JA021179>
- Qin M et al (2019) Investigating loss of relativistic electrons associated with EMIC waves at low L values on 22 June 2015. *J Geophys Res Space Phys* 124:4022–4036. <https://doi.org/10.1029/2018JA025726>
- Rae IJ et al (2018) The role of localized compressional ultra-low frequency waves in energetic electron precipitation. *J Geophys Res Space Phys* 123:1900–1914. <https://doi.org/10.1002/2017JA024674>
- Ripoll JF et al (2014) Electron lifetimes from narrowband wave-particle interactions within the plasmasphere. *J Geophys Res Space Phys* 119:8858–8880. <https://doi.org/10.1002/2014JA020217>
- Ripoll JF et al (2019) Local and statistical maps of lightning-generated wave power density estimated at the Van Allen Probes footprints from the World-Wide Lightning Location Network database. *Geophys Res Lett* 46:4122–4133. <https://doi.org/10.1029/2018GL081146>
- Ripoll JF et al (2021) Electromagnetic power of lightning superbolts from Earth to space. *Nat Commun* 12:3553. <https://doi.org/10.1038/s41467-021-23740-6>
- Rowland DE, Wygant JR (1998) Dependence of the large-scale, inner magnetospheric electric field on geomagnetic activity. *J Geophys Res* 103(A7):14959–14964. <https://doi.org/10.1029/97JA03524>
- Sample JG et al (2020) Nanosat and balloon-based studies of radiation belt loss: low-cost access to space. In: *The Dynamic Loss of Earth's Radiation Belts*. Elsevier, Amsterdam, pp 121–144. Chap. 5
- Sandhu JK et al (2021) ULF wave driven radial diffusion during geomagnetic storms: a statistical analysis of Van Allen Probes observations. *J Geophys Res Space Phys* 126:e2020JA029024. <https://doi.org/10.1029/2020JA029024>
- Sarno-Smith LK et al (2016) Spacecraft surface charging within geosynchronous orbit observed by the Van Allen Probes. *Space Weather* 14:151–164. <https://doi.org/10.1002/2015SW001345>
- Schiller Q et al (2016) Prompt injections of highly relativistic electrons induced by interplanetary shocks: a statistical study of Van Allen Probes observations. *Geophys Res Lett* 43:12,317–12,324. <https://doi.org/10.1002/2016GL071628>
- Selesnick RS et al (2016) Control of the innermost electron radiation belt by large-scale electric fields. *J Geophys Res Space Phys* 121:8417–8427. <https://doi.org/10.1002/2016JA022973>
- Selesnick RS et al (2019) Energetic electrons below the inner radiation belt. *J Geophys Res Space Phys* 124:5421–5440. <https://doi.org/10.1029/2019JA026718>
- Shen Y et al (2020) Potential evidence of low-energy electron scattering and ionospheric precipitation by time domain structures. *Geophys Res Lett* 47:e2020GL089138. <https://doi.org/10.1029/2020GL089138>
- Shumko M et al (2018) Microburst scale size derived from multiple bounces of a microburst simultaneously observed with the FIREBIRD-II CubeSats. *Geophys Res Lett* 45:8811–8818. <https://doi.org/10.1029/2018GL078925>
- Shumko M et al (2020) Electron microburst size distribution derived with AeroCube-6. *J Geophys Res Space Phys* 125(3):e2019JA027651. <https://doi.org/10.1029/2019ja027651>
- Southwood DJ, Kivelson MG (1981) Charged particle behavior in low-frequency geomagnetic pulsations 1. Transverse waves. *J Geophys Res* 86(A7):5643–5655. <https://doi.org/10.1029/JA086iA07p05643>
- Strangeway R et al (2005) Factors controlling ionospheric outflows as observed at intermediate altitudes. *J Geophys Res* 110:A03221. <https://doi.org/10.1029/2004JA010829>
- Su YJ et al (2016) Formation of the inner electron radiation belt by enhanced large-scale electric fields. *J Geophys Res Space Phys* 121:8508–8522. <https://doi.org/10.1002/2016JA022881>
- Takahashi K et al (2018) Van Allen Probes observations of second-harmonic poloidal standing Alfvén waves. *J Geophys Res Space Phys* 123:611–637. <https://doi.org/10.1002/2017JA024869>
- Takahashi K et al (2020) Multiharmonic toroidal standing Alfvén waves in the midnight sector observed during a geomagnetically quiet period. *J Geophys Res Space Phys* 125:e2019JA027370. <https://doi.org/10.1029/2019ja027370>
- Temerin M et al (1982) Observations of double layers and solitary waves in the auroral plasma. *Phys Rev Lett* 48:1175
- Thaller SA et al (2015) Van Allen Probes investigation of the large-scale duskward electric field and its role in ring current formation and plasmasphere erosion in the 1 June 2013 storm. *J Geophys Res Space Phys* 120(6):4531–4543

- Thaller SA et al (2019) Solar rotation period driven modulations of plasmaspheric density and convective electric field in the inner magnetosphere. *J Geophys Res Space Phys* 124:1726–1737. <https://doi.org/10.1029/2018JA026365>
- Tian S et al (2021) Evidence of Alfvénic Poynting flux as the primary driver of auroral motion during a geomagnetic substorm. *J Geophys Res Space Phys* 126:e2020JA029019. <https://doi.org/10.1029/2020JA029019>
- Torbert RB et al (2016) The FIELDS instrument suite on MMS: scientific objectives, measurements, and data products. *Space Sci Rev* 199:105–135. <https://doi.org/10.1007/s11214-014-0109-8>
- Tsuruda K et al (1994) Electric field measurements from the Geotail Spacecraft. *J Geomagn Geoelectr* 46(8):p693–711
- Tsyganenko NA, Sitnov MI (2005) Modeling the dynamics of the inner magnetosphere during strong geomagnetic storms. *J Geophys Res* 110:A03208. <https://doi.org/10.1029/2004JA010798>
- Tyler E et al (2019a) Statistical occurrence and distribution of high-amplitude whistler mode waves in the outer radiation belt. *Geophys Res Lett* 46:2328–2336. <https://doi.org/10.1029/2019GL082292>
- Tyler E et al (2019b) Statistical distribution of whistler mode waves in the radiation belts with large magnetic field amplitudes and comparison to large electric field amplitudes. *J Geophys Res Space Phys* 124:6541–6552. <https://doi.org/10.1029/2019JA026913>
- Ukhorskiy A et al (2014) Rotationally driven ‘zebra stripes’ in Earth’s inner radiation belt. *Nature* 507:338–340. <https://doi.org/10.1038/nature13046>
- Usanova ME et al (2016) Van Allen Probes observations of oxygen cyclotron harmonic waves in the inner magnetosphere. *Geophys Res Lett* 43:8827–8834. <https://doi.org/10.1002/2016GL070233>
- Usanova ME et al (2018) MMS observations of harmonic electromagnetic ion cyclotron waves. *Geophys Res Lett* 45:8764–8772. <https://doi.org/10.1029/2018GL079006>
- Vasko IY et al (2015) Thermal electron acceleration by electric field spikes in the outer radiation belt: generation of field-aligned pitch angle distributions. *J Geophys Res Space Phys* 120:8616–8632. <https://doi.org/10.1002/2015JA021644>
- Vasko IY et al (2017a) Electron holes in the outer radiation belt: characteristics and their role in electron energization. *J Geophys Res Space Phys* 122:120–135. <https://doi.org/10.1002/2016JA023083>
- Vasko IY et al (2017b) Diffusive scattering of electrons by electron holes around injection fronts. *J Geophys Res Space Phys* 122:3163–3182. <https://doi.org/10.1002/2016JA023337>
- Walsh BM et al (2013) Statistical analysis of the plasmaspheric plume at the magnetopause. *J Geophys Res Space Phys* 118(8):4844–4851. <https://doi.org/10.1002/jgra.50458>
- Wang X et al (2014) Photoelectron-mediated spacecraft potential fluctuations. *J Geophys Res Space Phys* 119:1094–1101. <https://doi.org/10.1002/2013JA019502>
- Wygant JR et al (1992) CRRES electric field/Langmuir probe instrument. *J Spacecr Rockets* 29(4):601–604. <https://doi.org/10.2514/3.25507>
- Wygant JR et al (1994) Large amplitude electric and magnetic field signatures in the inner magnetosphere during injection of 15 MeV drift echoes. *Geophys Res Lett* 21:1730
- Wygant JR et al (1998) Experimental evidence on the role of the large spatial scale electric field in creating the ring current. *J Geophys Res* 103(A12):29527–29544. <https://doi.org/10.1029/98JA01436>
- Wygant JR et al (2002) Evidence for kinetic Alfvén waves and parallel electron energization at 4–6 R_E altitudes in the plasma sheet boundary layer. *J Geophys Res* 107:SMP 24–1–SMP 24–15. <https://doi.org/10.1029/2001JA900113>
- Wygant JR et al (2013) The Electric Field and Waves Instruments on the Radiation Belt Storm Probes Mission. In: Fox N, Burch JL (eds) *The Van Allen Probes Mission*. Springer, Boston, pp 183–220. https://doi.org/10.1007/978-1-4899-7433-4_6
- Zheng H et al (2016) A statistical study of whistler waves observed by Van Allen Probes (RBSP) and lightning detected by WWLLN. *J Geophys Res Space Phys* 121:2067–2079. <https://doi.org/10.1002/2015JA022010>

Publisher’s Note Springer Nature remains neutral with regard to jurisdictional claims in published maps and institutional affiliations.

Authors and Affiliations

A.W. Breneman¹  · J.R. Wygant² · S. Tian² · C.A. Cattell² · S.A. Thaller² · K. Goetz² · E. Tyler² · C. Colpitts² · L. Dai² · K. Kersten² · J.W. Bonnell³ · S.D. Bale³ · F.S. Mozer³ · P.R. Harvey³ · G. Dalton³ · R.E. Ergun^{4,5} · D.M. Malaspina^{4,5} · C.A. Kletzing⁶ · W.S. Kurth⁶ ·

G.B. Hospodarsky⁶ · C. Smith^{3,7} · R.H. Holzworth⁸ · S. Lejosne³ · O. Agapitov³ · A. Artemyev⁹ · M.K. Hudson¹⁰ · R.J. Strangeway⁹ · D.N. Baker^{4,5} · X. Li⁴ · J. Albert¹¹ · J.C. Foster¹² · P.J. Erickson¹² · C.C. Chaston³ · I. Mann¹³ · E. Donovan¹⁴ · C.M. Cully¹⁴ · V. Krasnoselskikh¹⁵ · J.B. Blake¹⁶ · R. Millan¹⁰ · A.J. Halford¹

✉ A.W. Breneman

¹ Goddard Space Flight Center, NASA, Greenbelt, MD, USA

² School of Physics and Astronomy, University of Minnesota, Minneapolis, MN, USA

³ Space Sciences Laboratory, University of California, Berkeley, CA, USA

⁴ Laboratory for Atmospheric and Space Physics, University of Colorado Boulder, Boulder, CO, USA

⁵ Astrophysical and Planetary Sciences Department, University of Colorado, Boulder, CO, USA

⁶ Department of Physics and Astronomy, University of Iowa, Iowa City, IA, USA

⁷ University of New Hampshire Physics Department, Durham, NH, USA

⁸ Earth and Space Sciences, University of Washington, Seattle, WA, USA

⁹ IGPP and Department of Earth and Space Sciences, University of California, Los Angeles, CA, USA

¹⁰ Department of Physics and Astronomy, Dartmouth College, Hanover, NH, USA

¹¹ Air Force Research Laboratory, Kirtland Air Force Base, Albuquerque, NM, USA

¹² Haystack Observatory, MIT, Cambridge, MA, USA

¹³ Department of Physics, University of Alberta, Edmonton, Alberta, Canada

¹⁴ Department of Physics and Astronomy, University of Calgary, Calgary, Alberta, Canada

¹⁵ LPC2E, University of Orleans, Orleans, France

¹⁶ Space Science Applications Laboratory, The Aerospace Corporation, El Segundo, CA, USA